

**COMPUTATIONAL INVESTIGATIONS OF MOLECULAR  
TRANSPORT PROCESSES IN NANOTUBULAR AND  
NANOCOMPOSITE MATERIALS**

A Dissertation  
Presented to  
The Academic Faculty

by

Suchitra Konduri

In Partial Fulfillment  
of the Requirements for the Degree  
Doctor of Philosophy in Chemical Engineering  
in the School of Chemical & Biomolecular Engineering

Georgia Institute of Technology  
May 2009

**COMPUTATIONAL INVESTIGATIONS OF MOLECULAR  
TRANSPORT PROCESSES IN NANOTUBULAR AND  
NANOCOMPOSITE MATERIALS**

Approved by:

Dr. Sankar Nair, Advisor  
School of Chemical & Biomolecular  
Engineering  
*Georgia Institute of Technology*

Dr. William J. Koros  
School of Chemical & Biomolecular  
Engineering  
*Georgia Institute of Technology*

Dr. Peter J. Ludovice  
School of Chemical & Biomolecular  
Engineering  
*Georgia Institute of Technology*

Dr. Carson J. Meredith  
School of School of Chemical &  
Biomolecular Engineering  
*Georgia Institute of Technology*

Dr. Yonathan S. Thio  
School of Polymer, Textile & Fiber  
Engineering  
*Georgia Institute of Technology*

Dr. Min Zhou  
School of Mechanical Engineering  
*Georgia Institute of Technology*

Date Approved: February 05, 2009

## ACKNOWLEDGEMENTS

This thesis is the result of not just my efforts, but is influenced directly or indirectly by a number of people, whom I would like to acknowledge here. Firstly, I express my sincere thanks to my advisor, Prof. Sankar Nair, for providing me an opportunity to work with him, and for extending his unwavering support, guidance and commitment to help me develop my scientific skills and become a better researcher that I believe I am now. His trust and help in times of need are greatly appreciated. I am grateful to my committee members Prof. William J. Koros, Prof. Peter J. Ludovice, Prof. Carson J. Meredith, Prof. Yonathan S. Thio, and Prof. Min Zhou for providing valuable suggestions and for their critical reading of this thesis.

I thank Dr. Shaji Chempath (Los Alamos National Laboratory) for his collaboration in providing adsorption data using Monte Carlo simulations. I also thank Ashish Pande for helping me with Matlab coding, and Ji Zang for assistance with Fortran coding. My thanks are also due to Kevin Guger for periodically lending me IT support. Many thanks to all current and past Nair group members, especially Dr. Yeny Hudiono, Dr. Sanjoy Mukherjee, and Amir Ahmadi for making it a great place to work. Special thanks to my friends outside Georgia Tech – Krishna, Rajesh, Ashwini, Preeti, Tarun, Anand, Shabbir, Niket, Manish, Stephanie; and my friends at Georgia Tech- Mariefel, Krystle; for all the great times we spent together.

My heartfelt thanks go to my parents to whom I dedicate this thesis; my brother and grandmother for constantly inspiring me to work hard with utmost sincerity and achieve all my goals; for their faith in me, and for providing me emotional and moral support over the years. My deepest thanks to my best friend, critic, and my husband, Chakradhar for being there for me and constantly providing me support and encouragement at all times.

I gratefully acknowledge financial support of my thesis research by the ACS Petroleum Research Fund and the National Science Foundation.

## TABLE OF CONTENTS

Acknowledgements.....	iii
List of Tables .....	ix
List of Figures.....	x
Summary.....	xiv
Chapter 1: Introduction and Background.....	1
1.1. Nanotechnology and Nanomaterials.....	1
1.2. Transport Phenomena in Porous Nanomaterials.....	2
1.2.1. Polymer/Inorganic Layered Nanocomposites.....	4
1.2.1.1. Synthesis of Nanocomposite Membrane Materials .....	4
1.2.1.2. Transport in Nanocomposite Membrane Materials .....	6
1.2.2. Single-Walled Metal Oxide Nanotubes .....	9
1.2.2.1. Synthesis of Aluminosilicate Nanotubes .....	11
1.2.2.2. Transport in Nanotubes.....	13
1.3. Molecular Modeling of Nanoscale Structure-Property Relations.....	16
1.4. Overall Objective and Strategy .....	17
Chapter 2: Gas Transport in Polymer/Nanoporous Layered Silicate Nanocomposite Materials .....	20
2.1. Introduction.....	20
2.2. Computational Methodology .....	23
2.2.1. The force field.....	23
2.2.2. Model Construction .....	23
2.2.3. Diffusivity Calculations and Polymer Chain Vibration.....	26
2.2.4. Adsorption Isotherm and Diffusivity Calculations in MFI.....	27
2.3. Results and Discussion .....	28

2.3.1. Model Evaluation.....	28
2.3.2. Diffusion through PDMS/AMH-3 Nanocomposites .....	33
2.3.3. Diffusion Selectivities.....	37
2.3.4. PDMS Segmental Dynamics.....	41
2.4. Conclusions.....	43
Chapter 3: Development of a Force Field for Modeling Nanoporous Layered Aluminophosphates.....	45
3.1. Introduction.....	45
3.2. Methodology .....	47
3.2.1. Computational Details .....	47
3.2.1.1. Force field Parameterization .....	47
3.2.1.2. Molecular Dynamics (MD) simulations .....	50
3.2.2. Experimental Details.....	51
3.2.2.1. Fourier Transform Infrared Spectroscopy (FTIR).....	51
3.3. Results and Discussion .....	52
3.3.1. Structural Property Evaluation.....	52
3.3.2. Vibrational spectra .....	56
3.3.3. X-ray Diffraction .....	63
3.4. Conclusions.....	65
Chapter 4: Gas Transport in Stiff Chain Polymer/Nanoporous Inorganic Layered Nanocomposite Materials .....	67
4.1. Introduction.....	67
4.2. Transition State Approach Methodology.....	68
4.3. Computational Methodology .....	71
4.4. Results and Discussion .....	73
4.4.1. Penetrant Probability Density Distribution.....	73

4.4.2. Resident Sites.....	75
4.4.3. Future Work.....	77
Chapter 5: Dimension Control of Single-Walled Metal Oxide Nanotubes .....	78
5.1. Introduction.....	78
5.2. Computational Methodology .....	79
5.2.1. Force field Parameterization.....	79
5.2.2. Molecular Dynamics (MD) simulations .....	82
5.3. Results and Discussion .....	84
5.3.1. Force field parameterization and validation .....	84
5.3.2. Energy Minima in Single-Walled Metal Oxide Nanotubes.....	88
5.3.3. Harmonic Force Constant Model.....	91
5.3.4. Comparison of experimental and predicted nanotube diameters.....	95
5.4. Conclusions.....	97
Chapter 6: Water Transport and Adsorption in Single-Walled Aluminosilicate Nanotubes .....	99
6.1. Introduction.....	99
6.2. Methodology .....	101
6.2.1. Computational Details .....	101
6.2.1.1. Nanotube-Water Model Construction.....	101
6.2.1.2. Adsorption Isotherms.....	102
6.2.1.3. Diffusivity and Molecular Distribution .....	103
6.2.2. Experimental Details.....	105
6.2.2.1. Nanotube Synthesis and Gravimetric Moisture Sorption Analysis .....	105
6.3. Results and Discussion .....	105
6.3.1. Water Adsorption in Aluminosilicate Nanotubes.....	105
6.3.2. Water Structure in the Nanotube.....	110

6.3.3. Diffusivity and Transport Flux .....	114
6.4. Conclusions.....	122
Chapter 7: Conclusions and Future Research directions .....	124
7.1. Conclusions.....	124
7.2. Future Research Directions.....	128
7.2.1. Nanocomposite Membrane Materials with Layered Aluminophosphate .....	128
7.2.2. Gas Transport in Polymer/Porous Inorganic Layered Nanocomposite Materials .....	129
7.2.3. Molecular Transport in Single-Walled Metal-Oxide Nanotubes.....	130
7.2.3.1. Alcohol and Water/Alcohol Mixture Transport in Aluminosilicate Nanotubes .....	130
7.2.3.2. Transport in Functionalized Nanotubes.....	131
Appendix A: PCFF Force Field Expression and Parameters.....	132
Appendix B: Water Adsorption and Structure in Single-Walled Aluminosilicate Nanotubes .....	136
B.1. Water Adsorption Isotherms in Aluminosilicate Nanotubes .....	136
B.2. Internal energy of adsorption .....	140
B.3. O-O and O-H Pair correlation functions of water molecules in the aluminosilicate nanotube.....	141
References.....	142

## LIST OF TABLES

Table 2.1: Model details for the nanocomposite materials investigated. For each wt % of AMH-3, four different models were constructed, one for each permeant. For example, the first model in the Table had 99 PDMS monomers and 5 He permeant atoms, and had an equilibrated volume of 12.8 nm <sup>3</sup> .....	26
Table 2.2: Simulated and extrapolated experimental diffusivities for He, H <sub>2</sub> , N <sub>2</sub> and O <sub>2</sub> in PDMS, and zero-loading diffusivities in MFI at 300 K. # .....	31
Table 3.1: Force field parameters for layered aluminophosphates with Al/P ratio of 3:4.50	
Table 3.2: Structural property predictions in layered AlPOs.....	54
Table 3.3: Comparison of experimental IR peak positions and normal mode vibrational frequencies for layered AlPO-triethylamine.....	60
Table 3.4: Comparison of experimental IR peak positions and normal mode vibrational frequencies for layered AlPO-isopropanolamine.....	62
Table 5.1: Force field parameters used in MD simulations for calculating the energetics of single-walled AlSiGeOH nanotubes. Parameters for Al, Si, O and H are the same as the original CLAYFF <sup>171</sup> , force field with additional parameters for Ge developed in this work using the same procedures as the CLAYFF. ....	81
Table 5.2: Comparison of simulated (using final force field parameters) structural properties of C-phase of Na{AlGeO <sub>4</sub> }, D-phase of K{AlGeO <sub>4</sub> } and $\alpha$ - GeO <sub>2</sub> with experimental crystal structure data. ....	85
Table 5.3: Comparison between computed (from normal mode analysis) and power law fits of the theoretical expression for the RBM frequency in different AlSiGeOH nanotube compositions. $R$ is the nanotube radius in nm and the RBM frequencies are in cm <sup>-1</sup> . ....	90
Table A.1: PCFF force field parameters.....	132

## LIST OF FIGURES

- Figure 1.1: (a) Building unit of aluminosilicate nanotube showing hexagonal arrangement of aluminum atoms, bridging oxygens, and pendant silanol. (b) Cross-sectional view of the nanotube showing pendant silanol groups with 24 Al atoms in the circumference. (c) Side view of the nanotube represented by the stick model to show the non-uniform pore of the nanotube. Al- Green, Si-Gold, O-Red, H-Gray. .... 12
- Figure 2.1: Schematics of (a) nanostructure of the composite material investigated in the current study, (b) microstructure of ordered/oriented arrangement of the polymer/layer nanostructures, (c) microstructure of randomly dispersed polymer/layer nanostructures, and (d) microstructure of idealized nanocomposite membrane material (due to 3-D periodic boundary conditions) investigated in this study. The inorganic AMH-3 layers have the structure shown in Figure 2.2. .... 21
- Figure 2.2: Snapshot of equilibrated membrane model of PDMS confined between individual AMH-3 layers with H<sub>2</sub> molecules as penetrants. The outline represents the unit cell of the simulation model. H: Grey, C: Red, Si: Orange, O: Green. .... 29
- Figure 2.3: PDMS/AMH-3 nanocomposite membrane density as a function of AMH-3 loading in the membrane. Solid line denotes theoretical prediction and symbols denote simulated values. .... 30
- Figure 2.4: Adsorption isotherms of N<sub>2</sub> (green) and O<sub>2</sub> (red) in MFI at 295.95 K and 305.3 K, respectively. Diamonds indicate simulated values and open circles indicate reported experimental values<sup>131</sup>. .... 33
- Figure 2.5: (a) Overall (isotropic) diffusivities, (b) Lateral (XY-plane) diffusivities, and (c) Z-directional diffusivities of He (▲), H<sub>2</sub> (■), N<sub>2</sub> (●) and O<sub>2</sub> (◆) in PDMS/AMH-3 nanocomposite membrane as a function of AMH-3 loading in the membrane. (×) denote experimental diffusivities of He, H<sub>2</sub>, N<sub>2</sub> and O<sub>2</sub> in pure PDMS at 300 K. .... 35
- Figure 2.6: 8-membered ring (8MR) of AMH-3 showing the largest and the smallest (limiting) pore dimensions. Si: Orange, O: Green. .... 37
- Figure 2.7: (a) Overall (isotropic) diffusion selectivities of H<sub>2</sub>/N<sub>2</sub> (■), H<sub>2</sub>/O<sub>2</sub> (▲) and O<sub>2</sub>/N<sub>2</sub> (●) systems as a function of AMH-3 loading in the membrane. (b) Z-directional diffusion selectivities of the penetrants in the PDMS/AMH-3 nanocomposite membrane. Cussler model predictions are indicated as (—) for H<sub>2</sub>/N<sub>2</sub>, (---) for H<sub>2</sub>/O<sub>2</sub> and (----) for O<sub>2</sub>/N<sub>2</sub>. .... 38
- Figure 2.8: (a) Lateral and (b) Z-directional segmental motion of all polymer atoms in the nanocomposite membrane as a function of increasing confinement between the AMH-3 layers. .... 42

Figure 2.9: (a) Polymer mobility in the nanocomposite with 25wt% of AMH-3. Slice 1 is closest to the AMH-3 layer and slice 5 is the farthest. (b) Polymer mobility in different slices in a pure PDMS model.....	43
Figure 3.1: Comparison of experimental crystal structures (left) with predicted structures from molecular dynamics simulations (right). Snapshots show layered AlPOs with organic amine template molecules in the interlayer spacing. (a) 2D layered AlPO-triethylamine with 4×6×8 pore network, (b) 2D layered AlPO-isopropanolamine with 4×6×12 pore network, and (c) 1D chains of AlPO-trimethylamine with 4×8 pore network. Al-green, P-gold, O-red, N-Blue, C-grey, H-Cyan.....	56
Figure 3.2: Comparison between computed vibrational spectral peak positions (dotted lines) and experimental IR spectral peak (blue solid line) for (a) 2D layered AlPO-triethylamine, and (b) 2D layered AlPO-isopropanolamine. Solid green lines denote Gaussian curves and solid red line denotes the Gaussian fit of the FTIR spectra. ....	59
Figure 3.3: Comparison between computed X-ray diffraction patterns of 2D and 1D layered AlPOs crystal structures (black) and simulated structures (grey).....	64
Figure 4.1: Penetrant probability density distribution map of He in MFI (left) indicating straight (a), and sinusoidal channels of MFI pore structure. Gradient in color from dark blue to dark red indicates transition from low-high probability of finding He atoms in MFI structure. MFI snapshots indicating the pore channels are given on the right. Si-Gold, O-Red.....	74
Figure 4.2: Penetrant probability density distribution map of He in PDMS (left). The location of high penetrant probability density regions closely approximate with the resident sites in the snapshot of the He atoms in PDMS (right). Si-Gold, O-Green, C-Red, H-Grey, He-Cyan.....	75
Figure 4.3: Local maxima of penetrant (He) probability density values in PDMS obtained using steepest-descent method.....	76
Figure 4.4: He resident sites in PDMS matrix. The sites are expressed in different colors for clarity.....	76
Figure 5.1: Comparison between computed vibrational power spectra (orange) and experimental IR spectra (black) for AlSiGeOH nanotubes (a) $x = 1$ , (b) $x = 0.75$ , (c) $x = 0.5$ , (d) $x = 0.25$ , and (e) $x = 0$ . The Gaussian curves indicated in red are Si-O vibrations, blue are Ge-O vibrations and green are Al-O vibrations. ....	88
Figure 5.2: Total energy per atom at 298 K of AlSiGeOH nanotubes as a function of number of aluminum atoms ( $N$ ) in the nanotube circumference, for $x = 1.0$ (black), 0.75 (red), 0.5 (green), 0.25 (blue) and 0 (brown). Open symbols denote MD calculations and solid lines denote harmonic strain energy model fits (see Section 5.3.3).....	89
Figure 5.3: Computed Radial Breathing Mode (RBM) frequencies versus nanotube radius for AlSiGeOH nanotubes at $x = 1$ (black), 0.75 (red), 0.5 (green), 0.25 (blue) and 0	

(brown). Open symbols denote MD simulations and solid lines denote harmonic strain energy model fits..... 90

Figure 5.4: Bond strain energies of Al-O(red), Si-O(green)/Ge-O(blue) as a function of the number of aluminum atoms (N) in the circumference..... 95

Figure 5.5: Comparison of AlSiGeOH nanotube diameters versus nanotube compositional parameter  $x$ : computed (green), theoretical (red), and experimental (black) results. .... 97

Figure 6.1: Side view of an aluminosilicate nanotube shell showing nanotube interior with periodic wide and narrow pore regions. The constrictions of the pore are represented by stick model of silanol groups on the interior nanotube wall, while the rest of the linkages in the nanotube structure are represented by line model. Al (gold), Si (green), Nanotube-O (red), H (purple), Water-O (blue)..... 100

Figure 6.2: (a) Computed adsorption isotherms of water adsorbed in single-walled aluminosilicate nanotube as a function of relative humidity at  $T = 298$  (Blue), 308 (Red), 318 (green), and 325 K (black). (b) Measured adsorption isotherms showing amount of water adsorbed in single-walled aluminosilicate nanotube as a function of relative humidity at the same temperatures. .... 107

Figure 6.3: Deconvolution of computed adsorption isotherms (solid line) of water in Aluminosilicate nanotubes at 298 K into water sorption in the pores of the nanotube (dashed line) and water sorption into the interstitial spaces between the nanotubes (dotted line). .... 109

Figure 6.4: Snapshot of aluminosilicate nanotube membrane with adsorption of water molecules into nanopores as well as the interstitial spaces between the nanotubes at 100% RH and 298 K. Al (gold), Si (green), Nanotube-O (red), H (purple), Water-O (blue)... 109

Figure 6.5: Pair correlation function between hydrogen atoms of silanol groups and oxygen atoms of water molecules at various loadings of water molecules in the nanotube,  $N = 1$  (black dot and small dashed line), 4 (dark green medium dashed line), 8 (dark blue small dashed line), 16 (light blue dotted line) 32 (bright green large dashed line), 46 (red solid line). Values on y-axis are ratios of local density of water molecules to the average density in the nanotube. Correlation profiles have been increased by 25-50% of their original values to vertically shift the curves with respect to each other for better clarity of the figure. .... 112

Figure 6.6: Normalized distribution profiles of water molecules and silanol groups along the nanotube axis at various loadings of water molecules,  $N = 1$  (grey dot and small dashed line), 2 (light blue dot and large dashed line), 4 (dark green medium dashed line), 8 (dark gold small dashed line), 16 (bright green dotted line), 32 (blue large dashed line), 46 (red solid line), silanol groups (brown solid line), bulk water (black solid line). For better representation on a single plot, the profiles are normalized such that the total area under each curve is the same. To obtain the actual concentration profiles, each curve should be scaled by the corresponding number of water molecules (N). .... 113

Figure 6.7: Snapshot of molecular distribution of water in single-walled aluminosilicate nanotube. Picture shows water segregation into the wider regions of the nanotube at near saturation loading of water molecules (46 water molecules/simulation cell). Al (gold), Si (green), Nanotube-O (red), H (purple), Water-O (blue). ..... 114

Figure 6.8: Axial self-diffusivities ( $D_s$ ) of water in single-walled aluminosilicate nanotubes as a function of water content in the nanotube, calculated at water loadings varying from 1 to 46 water molecules/simulation cell (corresponding to a water content of 0.19 to 8.7 gm of H<sub>2</sub>O/100 gm of nanotube). Dashed line indicates diffusivity of bulk water. .... 116

Figure 6.9: (a) Schematic of aligned aluminosilicate nanotube thin film with water transport driven by a vapor pressure differential across the membrane and with vacuum on the permeate side.  $L$  is the membrane thickness. (b) Predicted water flux through 15 nm and 100 nm thin nanotube membranes as a function of vapor pressure differential across the membrane. .... 120

Figure B.1: (a) Measured adsorption isotherms showing amount of water adsorbed in single-walled aluminosilicate nanotube as a function of partial pressure at the same temperatures. (b) Computed adsorption isotherms of water adsorbed in single-walled aluminosilicate nanotube as a function of partial pressure at  $T = 298$  (Blue), 308 (Red), 318 (green), and 325 K (black). .... 137

Figure B.2: Site-specific computed adsorption isotherms of water in single-walled aluminosilicate nanotubes. Solid black lines denote total uptake of water in the nanotubes. Dashed lines denote desorption. Solid red lines denote adsorption into the nanopores and solid green lines denote adsorption in the interstitial spaces. .... 139

Figure B.3: Internal energy of adsorption of water molecules in the aluminosilicate nanotube as a function of pressure. .... 140

Figure B.4: O-O and O-H pair correlation functions of water molecules as a function of increasing water content in the nanotube. With increasing water content in the nanotube, the pair correlation functions for water molecules approximate the structure of bulk water. .... 141

## SUMMARY

The unique physical properties of porous nanomaterials, attributed to the combined effects of their nanoscale dimensions, shape, structure, porosity, and composition, make them attractive candidates for construction of nanostructured assemblies and nanodevices for potential applications such as separation devices, molecule sensors, and encapsulation media for molecule storage and delivery, among many other applications. Two important obstacles in the development of functional nanostructured devices are: (i) the difficulty of experimentally probing the nanoscopic length scales involved in the function of nanomaterials that in turn complicate the derivation of structure-property relationships, and (ii) ability to control the dimensions of nanomaterials to achieve desired properties. This work addresses these two challenges by developing and employing molecular simulation techniques, and experiments, to obtain a detailed understanding of (i) the structure-transport property relations in two classes of novel porous nanomaterials, namely, polymer/porous inorganic layered nanocomposite materials and single-walled metal oxide nanotubes, and (ii) fundamental factors influencing dimension control in single-walled metal oxide nanotubes.

Our detailed investigations on gas transport properties in polymer/porous inorganic layered nanocomposites for application as separation devices were performed using Molecular Dynamics simulations. Realistic atomistic models of polydimethylsiloxane (PDMS)/AMH-3 nanocomposites were constructed to study the diffusion of He, H<sub>2</sub>, N<sub>2</sub> and O<sub>2</sub> molecules as a function of AMH-3 content. The

diffusivities of He and H<sub>2</sub> were found to be a strong function of the AMH-3 loading in the nanocomposite, where as there was no appreciable increase in the diffusivity of O<sub>2</sub> and N<sub>2</sub> due to the molecular sieving effect of AMH-3. Predictions of separation properties of the nanocomposite material suggested that the present nanocomposite provided diffusion selectivity improvement as high as 21 (vs. 4) for H<sub>2</sub>/O<sub>2</sub> and 17 (vs. 3.6) for H<sub>2</sub>/N<sub>2</sub> over pure PDMS, while the selectivity for O<sub>2</sub>/N<sub>2</sub> showed little change. Further, the simulations provide a detailed insight on the increasing effect of polymer-inorganic interfacial interactions on the mobility of polymer chains and its effect on the molecule transport phenomena. In particular, at high AMH-3 loadings in the nanocomposite, the polymer chains became more rigid and inhibited penetrant diffusion.

We also developed an atomistic force field for simulating transport properties of layered aluminophosphate (AIPO) materials, which are emerging as potential layered inorganic materials for construction of polymer/porous inorganic layered nanocomposite materials. The force field, containing 9-6 Lennard Jones potential combined with the coulomb electrostatic potential, augments the existing PCFF force field to facilitate computational studies of layered AIPO-organic molecule hybrid materials. The force field parameters derived based on simultaneous predictions of crystal structures of 2D layered AIPOs (AIPO-triethylamine, AIPO-2-methylpiperazine, and AIPO-triethylenetetramine), and stringent validations of the force field obtained by comparing the predicted structural properties, X-ray diffraction patterns, and infrared vibrational spectra with the experimental values suggest that the force field successfully describes the structures of a broad range of 2D and 1D layered AIPOs. Next, in addition to

establishing molecular dynamics simulations procedure, we present preliminary work on developing Transition State Approach-Monte Carlo simulation technique for improving the computational times on calculating gas transport properties in nanocomposite materials.

In a parallel study, we investigated the phenomenon of diameter control that is unique to single-walled metal oxide aluminosilicogermanate ('AlSiGeOH') nanotubes. An interatomic potential model was parameterized, and was employed to perform Molecular Dynamics simulations to investigate the observed monodispersity in diameter of the nanotube from a thermodynamics perspective. The internal energy of the nanotube exhibited a minimum as a function of the diameter, and the minima occurred at different nanotube diameters with changing nanotube composition. We also developed a quantitative correlation to predict nanotube diameters by relating the nanotube composition and geometry to the strain energy of bending into a nanotube.

Finally, we investigated the diffusion properties of water in single-walled aluminosilicate nanotubes using Molecular Dynamics simulations, and adsorption properties using Monte Carlo simulations and experiments. The nanotubes exhibited a large fraction of water uptake (~10wt%) at <10% relative humidity indicating that the nanotube interiors are quite hydrophilic. The self-diffusivity of water molecules at room temperature was found to be Fickian. The diffusivity was comparable to bulk water diffusivity (at low water loadings of upto 3g/100g) and hence is considerably higher than in other nanoporous aluminosilicates such as zeolites. The structure of nanoconfined

water in the nanotubes displays a loading-dependent transition from isolated to connected clusters of water molecules. The water flux values predicted for an aluminosilicate nanotube film were found to be quite high ( $10^2$ - $10^3$  mol m<sup>-2</sup> s<sup>-1</sup>), even at very low pressure differentials (~24 mm Hg) across the membrane.

The studies presented here are the first computational investigations of transport properties of these novel porous nanomaterials, and represent the initial step towards providing guidelines for assisting the design and analysis of these nanostructures for potential application in separations, fuel cell technology and nanofluidics.

# CHAPTER 1

## INTRODUCTION AND BACKGROUND

### 1.1. Nanotechnology and Nanomaterials

The possibility of manipulating matter on sub-100 nm length scales to engineer high-efficiency nanodevices was first conceptualized by Feynman in 1959<sup>1</sup>. Since then nanotechnology has led to many scientific and technological advances in areas such as biology<sup>2</sup>, electronics<sup>3,4</sup>, catalysis<sup>5-7</sup>, energy<sup>5,6</sup>, food<sup>7,8</sup>, and fabric<sup>9,10</sup>. This tremendous increase in interest in this new technology is due to the fact that materials at nanoscale exhibit unique physical, chemical, and biological properties that are very different from the properties of bulk materials coupled with distinctive ability to systematically design devices with targeted applications. For example, gold at a bulk scale is a good reflector of light, however, when synthesized as nanoparticles it absorbs light and generates sufficient heat to destroy cancer cells<sup>2</sup>. Materials change their electrical conducting properties from conductors to semiconductors or semiconductors to insulators with size reduction to nanoscale regime<sup>11,12</sup>. Enhanced catalytic activity, changes in melting points, optical properties are a few of the many novel properties exhibited by nanoparticles<sup>13-15</sup>. Hence, nanostructured assemblies and devices constructed with nanomaterials as building blocks have been proposed to enable novel technological applications such as high strength nanocomposites, therapeutics, field-emitting surfaces, sensors, nanotransistors, electrode materials, and energy storage devices<sup>3-5,16-22</sup>.

The design of functional nanodevices can follow two approaches: a traditional ‘top-down’ approach, which employs miniaturization of large structures to nanoscale systems as followed in current electronics research; and a more precise, economical ‘bottom-up’ approach, which relies on device construction *via* (self) assembly of desired nanomaterials<sup>23,24</sup>. The latter approach is being increasingly accepted as a promising route for building more complex and miniaturized molecular machines while maintaining a precise control over the molecular structure. However, the immediate challenges in engineering a functional nanodevice using the ‘bottom-up’ approach involve (i) synthesis of nanomaterials with a precise control over the dimensions, structure, and composition to obtain nanomaterials with tailored properties suitable for incorporation in nanostructured assemblies and devices, and (ii) attaining a detailed understanding of the properties of nanoscale materials, which are influenced by the combined effects of their nanoscale dimensions, shape, structure, and composition, towards a rational design of the devices. In this thesis, we focus on investigating the structure-transport property relations in two classes of novel nanomaterials, namely, polymer/porous inorganic layered nanocomposite materials and single-walled metal-oxide nanotubes, and provide ‘semi-quantitative’ predictions on the design of nanodevices employing these materials.

## **1.2. Transport Phenomena in Porous Nanomaterials**

Porous nanomaterials provide large specific surface areas with a vast ability to adsorb and interact with molecules that result in unique and improved properties of these materials including high adsorption capacities, and molecular sieving due to size-

selective and shape-selective effects of the nanoscale pore structure. As a result, these materials are finding widespread applications such as energy storage (e.g. H<sub>2</sub> storage) devices, (bio)molecule sensors, biomolecule sequencers, porous electrode materials, nanotransistors etc., in addition to the traditional applications in adsorption, separation, catalysis, and ion-exchange. In order to realize these applications, it is important to understand and characterize the transport phenomena and molecular distribution of species in these materials, which exhibit a different transport mechanism as compared to bulk porous media (e.g. macroporous materials). As the dimensions of the pores approach the sizes of the species being transported in these materials, many interesting and unusual effects such as phase transitions <sup>25</sup>, anisotropic diffusion <sup>26</sup>, the ‘window’ effect <sup>27</sup>, ballistic diffusion <sup>28</sup>, Knudsen and single-file diffusion <sup>29-31</sup> are observed due to an increase in species-pore wall interactions. Consequently, the effects of surface physical properties such as porosity, internal surface area, surface roughness, pore geometry, pore size distribution, pore network connectivity, and chemical properties such as composition that affect the nature of species-pore interactions have to be evaluated to characterize the transport mechanism in porous nanomaterials and thereby determine their applicability in various technological areas.

In the next two sub-sections, a brief review is presented on mass transport mechanisms in two different porous nanomaterials: polymer/porous inorganic layered nanocomposite materials and single-walled metal-oxide nanotubes.

### 1.2.1. Polymer/Inorganic Layered Nanocomposites

Polymer nanocomposite materials are a class of reinforced polymers containing organic or inorganic particles that are nanoscopic in at least one dimension. Among the different types of nanocomposite materials, polymer/inorganic layered nanocomposites (polymers containing ~1nm thick impermeable nanoplatelet-like particles) have attracted great interest in the recent years. These materials, which combine the mechanical stability and processability of the polymer with the thermal and mechanical stability of the inorganic layer, exhibit novel as well as improved material properties compared to pure polymeric materials. A significant increase in tensile modulus (3 times more than corresponding pure polymeric material) and strength with as low as 4 wt% of impermeable inorganic layer content is a testimony to the tremendous property improvement offered by these materials<sup>32-34</sup>. Other unique properties demonstrated by these light weight materials include outstanding barrier properties, increased thermal stability, and fire retardancy<sup>35-41</sup>. The progress achieved in processing efficiency and property enhancement coupled with commercial success of these materials provides a great impetus for extending the concept of nanocomposites with *impermeable* inorganic layers to the synthesis of nanocomposites with *porous* inorganic layers for application in membrane technology.

#### 1.2.1.1. Synthesis of Nanocomposite Membrane Materials

Currently, gas separations using membranes are dominated by polymeric membrane materials that offer a somewhat limited potential for improving their intrinsic

selectivity and permeability properties. Polymer/porous inorganic layered oxide nanocomposite materials are under development as a new class of separation devices whose thickness can be scaled to the sub-100 nm regime <sup>42</sup>. These heterogeneous structures combine the good properties of each phase to improve the separation performance well beyond the limits of intrinsic properties of the polymeric materials. The nanometer thick porous inorganic layers act as ‘molecular sieves’ allowing fast transport of small gas molecules (with sizes smaller than the pore dimension of the inorganic layer) through the inorganic layers while increasing the tortuosity of transport paths for larger molecules (due to the large aspect ratio of the sieving material), thus enhancing the separation performance of the nanocomposite. The polymeric component, on the other hand, provides the mechanical stability and economic processability of the nanocomposite.

The synthesis of polymer/inorganic layered nanocomposites can be achieved *via* different methods depending on the constituent materials and fabrication techniques. These methods include: (a) Intercalation of polymers in layered inorganic hosts, (b) In situ intercalative polymerization, (c) Melt intercalation, and (d) Templated synthesis <sup>39,41</sup>. A successful approach to synthesize these nanocomposites was shown to be *via* intercalation of polymers in the layered inorganic materials. This procedure involves (i) synthesis of the desired inorganic layered materials, (ii) exfoliation into single layers by swelling the layered material in an aqueous or organic solvent in which even the polymer is soluble, and (iii) fabrication of the nanocomposite material by mixing the polymer and inorganic layered solutions such that the polymer chains intercalate into the interlayer

domains by displacing the solvent <sup>33,42-49</sup>. Depending on the thermodynamics (i.e. interplay of entropic effects due to nanoconfinement of polymeric chains and total enthalpy of mixing) of the interfacial interactions, three types of hybrid material morphologies have been identified: (i) phase separated composite-with immiscible polymer and inorganic layers, (ii) intercalated structure-with polymer chain intercalating within the interlayer spacing of two adjacent inorganic layer resulting in a well ordered multilayer structure, and (iii) exfoliated or delaminated structure- obtained as a result of dispersion of inorganic layers in the continuous polymeric matrix <sup>39,41,43</sup>. The separation performance of a nanocomposite membrane material largely depends on the quality of the ‘interface’ region between the polymeric and sieve phases. Appropriate choice of the polymeric material that maintains flexibility during membrane formation and exhibits synergetic interactions with the sieving material that is capable of screening the gas molecules based on shape- and size-selectivity effects of the pore structure, may not only lead to improved mechanical and thermal stability but also improved membrane permselectivities by forming membranes that are free of any defects or macro voids. Consequently, many efforts in the recent past have focused on surface modification of the molecular sieve with a variety of coupling agents to provide a good polymer-to-sieve contact <sup>50-55</sup>.

#### 1.2.1.2. Transport in Nanocomposite Membrane Materials

Polymer/porous inorganic layered nanocomposite materials present three different physical regions to the permeating molecules: (i) polymer, (ii) porous inorganic layer,

and (iii) polymer-inorganic layer interface region. Within the polymeric region, gas transport occurs by adsorption of molecules into the polymeric matrix followed by diffusion. The diffusion is proposed to occur via random ‘jumps’ of penetrant molecules in transient gaps of polymeric matrix created by thermal motion of the polymer segments<sup>56-58</sup>. The intrinsic selectivity of the polymer depends on the penetrant solubility in the polymer as well as the difference in rates at which the transient gaps that are big enough to accommodate the penetrant molecules are formed<sup>59</sup>. Transport in the porous inorganic layer depends on the structure and pore network of the material. For a porous structure with pore sizes approximating the size of penetrant molecules (as is the case with molecular sieve material in the nanocomposite), diffusion is described as a transition state process where a penetrant jump between two consecutive pore locations proceeds through a transition state (i.e. channel connecting the pores)<sup>60</sup>. Consequently, diffusion selectivity can be high as molecules with smaller sizes (than the pore dimensions) can readily jump over the energy barrier at transition state compared to the less frequent jumps by the larger molecules. Finally, transport within the polymer-inorganic layer interfacial region, a critical factor that governs the performance of these nanocomposite membranes, is not very well understood due to the very small length scales (~1nm) of the interfacial region that make it difficult to obtain a direct experimental characterization owing to the lack of required spatial resolution that can differentiate the interfacial region from the “bulk” regions. Previous studies on gas transport in micro-composites (composites with micrometer thick, porous materials such as zeolites and carbon molecular sieves) suggested ‘rigidification’ of polymer segments closer to the microporous material surface that lead to a decreased permeability of gases in the

composite<sup>54,61-64</sup>. On the other hand, the high aspect ratio porous inorganic layers in the nanocomposite present large interfacial specific surface area to the surrounding polymer matrix that induce novel structural and functional properties that cannot be understood by simple scaling of the individual properties of the polymer and inorganic components.

Till date, there are very few experimental studies that focused on transport properties of polymer/porous inorganic layered oxide nanocomposite materials. Studies on gas transport in glassy polymer polyimide/10 wt% layered aluminophosphate nanocomposite demonstrated selectivity enhancement by a factor of 2.5 for O<sub>2</sub>/N<sub>2</sub> and 3 for CO<sub>2</sub>/CH<sub>4</sub> compared to pure polyimide<sup>42</sup>. Similarly, polybenzimidazole/layered silicate AMH-3 nanocomposite increased H<sub>2</sub>/CO<sub>2</sub> selectivity by a factor of 2 compared to pure polymeric materials even at very low loading of 2wt% of AMH-3 in the nanocomposite<sup>47,49</sup>. However, analogous to micro-composite materials, these nanocomposites exhibited a decrease in permeability compared to pure polymeric case<sup>42,47,49,50,55,65-67</sup>. The permeability reduction was more pronounced with an increase in the size of the penetrating gas molecule as well as the total amount of inorganic content in the nanocomposite, and is related to the large aspect ratio of the nanoplatelets that increase the tortuosity of the transport path of the gas molecules.

Detailed understanding of transport properties of nanocomposite materials based on porous inorganic layer structure, nanocomposite morphology (intercalated, exfoliated or partially exfoliated), composition (amount of polymeric vs. inorganic layer content), and nature of interactions between the polymer and inorganic layers<sup>32-34,38,42,47,49</sup> are

required to establish structure-transport property relations in these materials. This will enable the development of an efficient method to predict the nanocomposite properties based on the properties of individual polymeric or inorganic layer materials towards guiding the synthesis of superior membrane materials.

### **1.2.2. Single-Walled Metal Oxide Nanotubes**

Nanotubes are defined as hollow cylindrical objects with diameters and occasionally lengths in the nanoscale regime. These materials have attracted significant attention over the past couple of decades due to their remarkable physical properties, which allow their application as ‘building blocks’ for a variety of nanostructured assemblies and nanodevices<sup>18,19</sup> including high strength nanocomposites<sup>16</sup>, field-emitting surfaces<sup>4</sup>, (bio)molecule separation devices<sup>68</sup>, sensors<sup>17,69</sup>, nanotransistors<sup>3,70</sup>, electrode materials<sup>20</sup>, and encapsulation media for molecule storage and delivery<sup>5,71,72</sup>, and as channels for rapid fluid flow<sup>73-75</sup>. The exceptional properties of nanotubes are attributed to the combined effects of their nanoscale dimensions, hollow cylindrical shape, composition, structure, and porosity. Although there have been significant advances in characterizing the properties of nanotubes in relation to their structure, synthesis of nanotubes with high yield, well-controlled (nanoscale) dimensions, structure (e.g. chirality), and composition to achieve desired properties remains a challenging issue. This situation can be attributed to several factors, including challenges in understanding the mechanism of nanotube synthesis due to fast formation kinetics that impede mechanistic studies toward rational control of nanotube dimensions, structure and

composition. For example, carbon nanotubes and inorganic ‘carbon-like’ nanotubes (e.g. WS<sub>2</sub>) are synthesized *via* arc vaporization, laser ablation and catalytic chemical vapor deposition where the nanotube formation and growth steps occur over very short time scales of femto seconds to seconds resulting in single-walled nanotubes that are polydisperse in dimensions, structural chirality and multi-walled nanotubes as occasional impurities <sup>76</sup>. Likewise, certain metal oxide nanotubes (e.g. ZnO, TiO<sub>2</sub>) are synthesized in high temperature vapor phase reaction over solid or liquid seed materials with fast reaction kinetics that allow little control over the nanotube dimensions or composition <sup>77,78</sup>.

Concepts relevant to nanotube diameter control using a thermodynamic basis have been first speculated by Pauling in the context of naturally occurring chrysotile nanotubes <sup>79</sup>. It was proposed that differences in interatomic bond energies, based on nanotube composition, on the inner and outer nanotube walls generate a bending strain that favors formation of a cylindrical structure rather than a flat (layered) material. The work demonstrated a possibility of nanotube diameter control through interplay of differences in interatomic bond energies. However, such a concept cannot be extended to carbon nanotube or their inorganic counterparts due to their compositions that are constant through their structure resulting in the internal energy of carbon nanotubes (and other structurally analogous nanotube materials) to decrease monotonically with increasing diameter. In contrast, a newly emerging class of inorganic metal oxide nanotubes such as the natural imogolite materials, which can be synthesized with tunable composition,

present good model systems for testing and developing the proposed thermodynamics concepts for nanotube diameter control.

#### 1.2.2.1. Synthesis of Aluminosilicate Nanotubes

Imogolite is a hydrous aluminosilicate ‘clay’ mineral that occurs naturally in volcanic ash <sup>80</sup>. The material is present as unique fibrous structure consisting bundles of very thin (~2nm diameter) single-walled nanotubes. The structural model of aluminosilicate nanotube, a synthetic analogue of natural imogolite, was first proposed by Cradwick et al <sup>81</sup>. The cylindrical wall of these nanotubes can be visualized as a rolled-up sheet of gibbsite (aluminum hydroxide), with isolated silanol ( $\equiv\text{Si-OH}$ ) groups linked to the inner surface of the nanotube wall. The outer diameter of the nanotube is ~2.2 nm and its inner diameter is ~1 nm. The wall is composed of hexagonally arranged aluminum atoms connected by double oxygen bridges. On the outer surface, each oxygen is coordinated to two aluminum atoms and a hydrogen atom. On the inner surface the hydrogen atoms are replaced by silicon, with every three oxygens coordinated by one silicon. Figure 1.1 (a)-(c) shows the hexagonal building unit, cross-sectional and side views of the nanotube structure showing the pendant silanol groups on the inner surface as suggested based on solid-state NMR, TEM and XRD studies <sup>81-83</sup>. The octahedrally coordinated aluminum atoms are well ordered and the axial unit cell dimension of the nanotube is 0.85 nm <sup>81-84</sup>. The number of aluminum atoms in the circumference (N) is necessarily an even number. No chiral properties have been observed for these nanotubes, and the symmetry of the nanotube is that of the zigzag (n,0) configuration of carbon

nanotubes. The chemical formula of the unit cell is  $(\text{Al}_2\text{SiO}_7\text{H}_4)_N$ . Interestingly, the silanol groups on the inner surface of the nanotube can be partly or completely substituted with germanol ( $\equiv\text{Ge}-\text{OH}$ ) groups to form nanotubes with different diameters and lengths<sup>85-88</sup>.

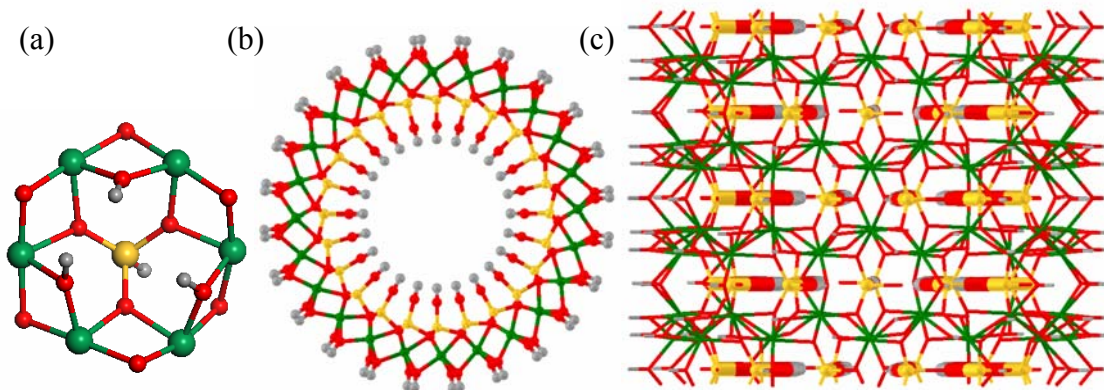


**Figure 1.1:** (a) Building unit of aluminosilicate nanotube showing hexagonal arrangement of aluminum atoms, bridging oxygens, and pendant silanol. (b) Cross-sectional view of the nanotube showing pendant silanol groups with 24 Al atoms in the circumference. (c) Side view of the nanotube represented by the stick model to show the non-uniform pore of the nanotube. Al- Green, Si-Gold, O-Red, H-Gray.

Synthesis of aluminosilicate nanotubes proceeds *via* a low-temperature aqueous phase chemistry to form nanotubes that are exclusively single-walled and more importantly, *monodisperse* in dimensions<sup>86,87</sup>. The synthesis mechanism consists of controlled chemical bonding between the individual metal (Al, Si/Ge) precursors in the solution by employing strict pH control to form mixed aluminosilicate(germanate) precursors. Subsequently, a temperature control (between 65-95°C) is applied to condense the mixed metal precursors into amorphous nanoparticles of sizes ~6 – 12 nm, which ultimately self-assemble to form ordered aluminosilicate (AlSi) or

aluminogermanate (AlGe) nanotubes<sup>86,87</sup>. Based on several type of experimental evidence including nitrogen adsorption, X-ray diffraction, TEM, and dynamic light scattering, it is accepted that synthetic AlSi and AlGe nanotubes are highly monodisperse in diameter and length (AlSi – diameter ~2.2 nm and length ~100nm, AlGe-diameter ~3.3 nm and length ~15nm), irrespective of a substantially diverse range of synthesis conditions reported in the literature. In addition, these nanotube materials present unique properties such as short lengths, well defined structure, non-uniform nanopore structure (unlike carbon nanotubes), ability to disperse in the aqueous phase, and hydrophilicity (unlike hydrophobic carbon nanotubes) due to the presence of hydroxyl groups on the inner and outer walls of the nanotubes, which make them attractive candidates for applications in nanofluidic devices.

#### 1.2.2.2. Transport in Nanotubes

Nanotubes are being increasingly investigated for application in nanofluidic devices<sup>68,69,71,73-75,89,90</sup> among many other potential technological applications due to their hollow cylindrical structure that can be visualized as a conduit for fluid flow. Several experimental and computational studies on gas and liquid adsorption and transport in nanotubes (single- and multi-walled) demonstrated the possibility of attaining high molecular uptake<sup>90-92</sup> as well as fast fluid and selective fluid fluxes<sup>28,73-75,93</sup>, a phenomenon attributed to (i) high specific surface area of the nanotubes that allows preferential adsorption of molecules due to molecule-pore interactions, (ii) the atomic-scale smoothness of the (carbon) nanotube walls that facilitate “frictionless” flow of

fluids, and (ii) molecular ordering phenomena observed inside the nanopores. Depending on the inner diameter of the nanotube, fluid molecules encapsulated in nanotubes have been reported to form a variety of high-density condensed phases<sup>25,91</sup> as well as ordered nanostructures such as one-dimensional water wires<sup>28,94</sup>, and core-shell structures with a cubic ice sheet enveloping a chain-like water configuration<sup>95</sup>.

Transport of molecules in straight, narrow cylindrical pores such as nanotubes is dominated by molecule-molecule and molecule-pore interactions that cannot be predicted by simple Knudsen and Single-file diffusion models. These models assume that the diffusion of an isolated molecule in any nanopore can sufficiently describe the collective diffusion mechanism at any loading. However, recent computational and experimental studies suggested that diffusion of nano-confined molecules was influenced by formation of molecule ‘clusters’ that exhibited concerted motion coupled with weak molecule-pore wall interactions, resulting in diffusivities that are orders of magnitude higher than Knudsen or Single-file diffusion predictions<sup>28,73-75,96,97</sup>. For example, simulation studies on gas transport in narrow (~1.4 nm diameter) carbon nanotubes have shown light gas (H<sub>2</sub>, CH<sub>4</sub>) diffusivities that were within the same order of magnitude as bulk gas diffusion<sup>73,98</sup>. Similar diffusivity enhancements were observed for the case of water transport in short (~1.4 nm), narrow (~0.8 nm) carbon nanotubes. The simulation study demonstrated high water diffusivity due to spontaneous bursts of concerted water molecule transport through the hydrophobic nanotube, a result attributed to the strongly hydrogen-bonded clusters of molecules occasionally entering the nanotubes, and weak interactions between water and the nanotube walls<sup>28</sup>. The predictions of enhanced water fluxes (driven by

pressure gradients) have been realized experimentally via fabrication of membranes from aligned multi-walled (MW), as well as single- or double-walled (DW), carbon nanotubes by Hinds et al.<sup>74</sup> and Holt et al.,<sup>75</sup> respectively. The results showed a 3 to 5 orders-of-magnitude increase in liquid flow rates as a function of nanotube diameters and a 1 to 2 orders-of-magnitude increase in gas transport rates, compared to conventional Poiseuille flow predictions. Further, recent molecular dynamics (MD) simulation studies showed some selectivity in these nanotube membranes due to the preferential adsorption of one species over the other<sup>93</sup>.

Although the computational and experimental studies to date provide substantial evidence that carbon nanotubes can be used in the construction of nanofluidic devices such as high-flux and selectivity membranes, it is difficult to synthesize carbon nanotubes with well-controlled lengths below 100 nm<sup>99,100</sup>. On the other hand, single-walled aluminosilicate and aluminogermanate nanotubes can already be synthesized with tunable dimensions (i.e., ~ 15-100 nm in length and ~2-3.5 nm in outer diameter) and hydrophilic interiors<sup>86,92,101</sup> via aqueous phase chemistry. Till date, there is no information on transport properties of these novel nanotube materials. Hence, in this thesis we examine the phenomenon of dimension control in these nanotubes, and investigate the water adsorption and diffusion properties.

### **1.3. Molecular Modeling of Nanoscale Structure-Property Relations**

Successful application of nanoporous materials requires a detailed understanding of their macroscopic properties in relation to their structure. The macroscopic properties are in turn governed by molecular processes that occur in nanoscopic length scales, which are difficult to probe by experimental techniques that often lack the relevant spatial and temporal resolution. For example, transport process in polymer/inorganic layered nanocomposite materials are influenced by large (due to high aspect ratio inorganic layers) polymer-inorganic layer ‘interfacial’ regions, wherein the inorganic material and the polymer are confined between each other and together influence the transport of molecules through them. However, the very small length scales (~1nm) of the interfacial regions make it difficult to obtain direct experimental characterization (using XRD, TEM, solid-state NMR, SANS, DLS, FTIR) with the required spatial resolution<sup>35,36,41,43</sup>. For the same reason, it is difficult to probe the dynamics of molecules in nanotubes to understand their transport mechanism. On the other hand, molecular simulation methods that employ a detailed atomistic description of the structure of these novel materials can provide a fundamental understanding on the molecular mechanism of observed macroscopic properties.

With recent advances in computing power, molecular modeling techniques have become widely used methods to investigate the molecular structure and properties of a variety of organic as well as inorganic systems. There have been computational investigations of polymer/nonporous layered silicate composites (which are of interest, e.g., as barrier materials and high-mechanical-strength materials) that focused on

understanding the changes in layer cation transport with changes in structural conformation and segmental dynamics of nanoconfined polymer<sup>102,103</sup>. Other researchers have examined the interfacial energetics and dynamics of related systems such as clays and polymer-nanoparticle composites<sup>104-106</sup>, and molecule transport in a composite system containing polydimethylsiloxane and a zeolite phase<sup>107</sup>. In the case of nanotubular materials, computational investigations on gas and water diffusion in carbon nanotubes have provided detailed information on the diffusion mechanism and fluid structure inside the nanotube as a function of its dimensions<sup>28,73,95,108,109</sup>. The knowledge from such studies can be used to determine the structure-property relationships that will be valuable in developing novel nanostructured assemblies and devices. In the course of this thesis, I present the first computational studies on gas transport in polymer/porous inorganic layered oxide nanocomposites as well as water transport and adsorption properties in single-walled metal oxide nanotubes.

#### **1.4. Overall Objective and Strategy**

The focus of this research, detailed in this thesis, is to understand fluid transport phenomena and establish structure-transport property relationships in novel porous nanomaterials including polymer/porous inorganic layered nanocomposite, and single-walled metal oxide nanotubes, using molecular simulation techniques such as Molecular Dynamics and Monte Carlo to provide design guidelines for construction of nanostructured assemblies and devices. This objective was achieved as follows: Chapter 2 of this thesis provides detailed computational study of gas transport in polymer/porous

inorganic layered nanocomposite materials. Molecular dynamics simulations were employed to provide a fundamental understanding on gas diffusion process and polymer dynamics. The effects of confinement on the segmental mobility of the polymer and gas diffusion are presented. In Chapter 3, we present our study on development of a force field for simulating layered aluminophosphates, which are potential candidates for use as molecular sieving layers in nanocomposite membrane materials. The validity and transferability of the force field was established by detailed comparison of structural properties, XRD patterns and vibrational spectra between the simulated and experimental crystal structures. In Chapter 4, we present our preliminary work on developing Transition State Approach Monte Carlo simulation technique to study gas transport in nanocomposite materials containing stiff chain polymers. This computational method was employed to probe simulation time scales (few ns to  $\mu$ s) and length scales (10-100nm) that are inaccessible to Molecular dynamics simulations. Chapters 2-4 together provide a fundamental understanding on gas transport phenomenon in novel polymer/porous inorganic layered nanocomposite membrane materials for application in gas separations, and fuel cell technology.

Chapters 5 and 6 detail our computational studies on structure and water transport properties of single-walled metal oxide nanotubes. In Chapter 5, we present interesting results on a unique correlation between the nanotube diameter, composition and internal energy underlying the synthesis of single-walled metal oxide nanotubes with tunable diameters. In Chapter 6, we present detailed experimental and computational studies on water adsorption and transport properties of single-walled aluminosilicate nanotubes and

provide predictions for diffusive fluxes as a function of nanotube length. Finally, I summarize the present research work in Chapter 7, and discuss the future directions of research in deriving structure-property relations in novel nanomaterials.

## CHAPTER 2

# GAS TRANSPORT IN POLYMER/NANOPOROUS LAYERED SILICATE NANOCOMPOSITE MATERIALS

### 2.1. Introduction

Polymers containing nanoporous, high-aspect-ratio, nanometer thick inorganic layered materials are being investigated as candidates for overcoming the selectivity-versus-permeability trade-offs imposed by conventional polymeric membranes used in gas separations. In the present study, our main objective is to obtain insight into gas diffusion processes in polymer/porous inorganic layer nanocomposite materials wherein the inorganic component is synthesized as a layered material that can subsequently be exfoliated. Towards this goal, we present the first computational investigation of molecular transport and polymer dynamics in such polymer/porous layered material nanocomposites. Figure 2.1(a) shows a schematic of the nanocomposite membrane material of the type being considered in this study. The inorganic components are individual layers of thickness  $\sim 1$  nm dispersed in the polymer, with nanopores ( $\sim 0.5$  nm in size) allowing transport through the layer. Depending on the thickness and structure of the layer, there may be additionally a nanoporous network in the plane of the layer that allows lateral transport through it. This is the case for the layered material considered here. The membrane may either contain the layers dispersed in an ordered/oriented manner such as in Figure 2.1(b), or in random orientations as shown in Figure 2.1(c). In other words, the nanostructure of Figure 2.1(a) can be arranged to yield different membrane microstructures that may show differences in performance. In both cases, it is

desirable that the layers have high aspect ratios as well as high molecular sieving selectivity. This ensures that the preferred species is transported effectively through the layers, whereas the other species must take a much more circuitous path around the layer.

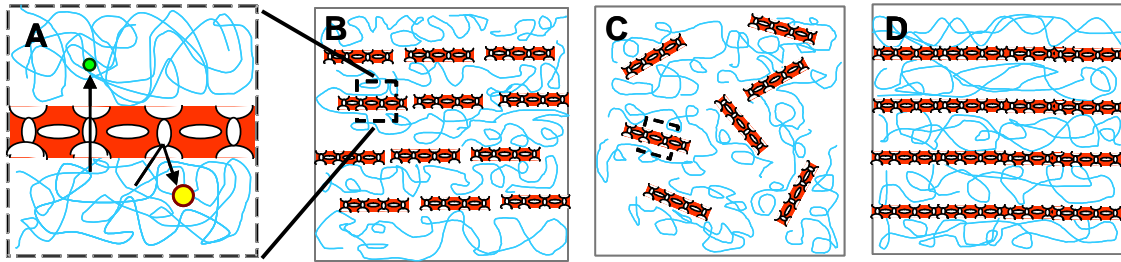


**Figure 2.1:** Schematics of (a) nanostructure of the composite material investigated in the current study, (b) microstructure of ordered/oriented arrangement of the polymer/layer nanostructures, (c) microstructure of randomly dispersed polymer/layer nanostructures, and (d) microstructure of idealized nanocomposite membrane material (due to 3-D periodic boundary conditions) investigated in this study. The inorganic AMH-3 layers have the structure shown in Figure 2.2.

While the issue of modeling the microstructure (in addition to the nanostructure) can only be rigorously tackled within a multiscale modeling framework, the focus of this study is to investigate the fundamental transport processes in the nanostructure of Figure 2.1(a). Since periodic boundary conditions are imposed on the system, the present study corresponds to an idealized microstructure of the type shown in Figure 2.1(d). By analyzing the transport properties in the perpendicular (Z-) direction of this nanostructure, one obtains an approximation of the transport properties of the microstructure in Figure 2.1(b) under the assumption of large aspect ratios. On the other hand, analyzing the isotropic transport properties of the system in Figure 2.1(d), leads to an approximation of the behavior of the system in Figure 2.1(c) which is isotropic from a

macroscopic point of view. Thus, the idealized structure can be used to provide realistic upper bounds on the performance of both types of microstructures, recognizing that a high-quality nanostructure provides the “necessary” (but not always “sufficient”) condition for a high-selectivity membrane.

For our study, we employed polydimethylsiloxane (PDMS) as a model polymer, due to its structural simplicity and availability of transport property measurements<sup>110-112</sup>. A recently synthesized three-dimensionally nanoporous layered silicate, AMH-3<sup>113</sup>, was chosen as the functional material. AMH-3 (see Figure 2.2) is a layered silicate with layers that contain 8-membered silicate rings in all three principal directions. We first describe the construction of realistic atomistic models of a PDMS/AMH-3 nanocomposite material. We then discuss details of molecular dynamics (MD) simulations using the models, to study the diffusion of gas molecules such as He, H<sub>2</sub>, N<sub>2</sub> and O<sub>2</sub> as a function of AMH-3 content. Next, we analyzed our results in terms of the nanocomposite structure and composition, and compared the computational predictions with theoretical predictions for conventional composites to highlight the importance of interfacial effects on the transport properties of the nanocomposites. Finally, we studied the effect of confinement on the mobility of the polymer chains and its effects on permeant diffusion. The investigations described here are intended to form the first step towards a predictive basis for assisting the design and analysis of polymer/nanoporous layered inorganic nanocomposite membranes.

## **2.2. Computational Methodology**

### **2.2.1. The force field**

All the simulations reported here employ the PCFF force field, which is widely used to describe siloxanes and silicates<sup>114-117</sup>. Full details of the force field parameters and interatomic potential energy expressions are provided in Appendix A. To verify that the force field well describes the interaction of the gas molecules with the polymer, we performed calculations of the diffusivity of the four gases in pure PDMS and compared them to prior experimental and computational studies. These results are detailed in Section 2.3.1. To check the quality of the interaction parameters between the gas and AMH-3, we performed diffusion and Grand Canonical Monte Carlo (GCMC) adsorption simulations on another pure-SiO<sub>2</sub> nanoporous material, viz. the zeolite MFI<sup>118</sup> (see Section 2.3.1). Overall, these validation studies generate confidence that the transport predictions using the PCFF are accurate at least qualitatively and most likely in a quantitative sense.

### **2.2.2. Model Construction**

For the polymeric material, the construction and equilibration of our atomistic models follow the procedures outlined by Hofmann<sup>107</sup>. All simulations were performed with the aid of the Materials Studio 3.2 molecular simulation program (Accelrys, Inc). First, bulk polymer (PDMS) unit cells including the penetrant molecules were constructed employing the packing algorithm of Theodorou and Suter<sup>119</sup>. The polymer

chain along with a small number (2-13) of penetrant molecules was packed into a simulation cell under periodic boundary conditions at the experimental density of PDMS (0.95 g/cc)<sup>107</sup>. The penetrant loadings in the polymer were kept low (0.5-3 wt%), thus avoiding effects of interactions between the penetrant molecules. We note that these loadings are nevertheless comparable to the solubilities of these gases in PDMS at typical temperatures and pressures of operation<sup>107,120</sup>. The packing cells were then subjected to structure optimizations *via* the steepest descent method, followed by the conjugate gradient method until the maximum energy gradient at any atom was below 10 kcal/mol/Å. These optimized models were subjected to extensive equilibration procedures using MD simulations in the NVT and NPT ensembles. The structures were equilibrated for up to 25 ps. After an initial NVT-MD run at 300 K, each packing model was subjected to NPT-MD at atmospheric pressure (1 bar) to test whether it relaxes to the experimental PDMS density. If the result deviated by more than 1% from the experimental value, the model was further subjected to NPT-MD compression runs to relieve any unrealistic stresses present in the packing cell. This involved simulations at increased pressures (1-1000 bar), alternating between NVT and NPT-MD steps until the simulated density was well above the target value. The resulting structures were again relaxed via NPT-MD runs at atmospheric pressure. The compression and relaxation cycles were repeated until the final densities were within 1% of PDMS experimental density and the system energy converged to an equilibrium value.

The PDMS/AMH-3 nanocomposite structures were built from the equilibrated structure of the PDMS obtained above<sup>121</sup>. The AMH-3 layer structure was taken from the

published crystal structure<sup>113</sup>. The negative charges on the surface siloxy (-Si-O<sup>-</sup>) groups were passivated by bonding hydrogen atoms to these oxygens. These negative charges are compensated by inter-layer strontium and sodium cations in crystalline AMH-3, but these cations would be removed when the material is exfoliated. The AMH-3 layer was then added to the PDMS model to create an initial composite structure. The PDMS models are constructed with different unit cell sizes, such that the addition of a single AMH-3 layer leads to a predetermined weight fraction (0.25, 0.47, or 0.7) of AMH-3. Note that these loadings cover the composition range of previous work on polymer/clay composite fabrication, as well as current research (in our laboratories and elsewhere) aimed at producing high-inorganic-weight-fraction nanocomposite materials. The composite structure was then subjected to MD structure optimization and equilibration procedures. Since there is no experimental density data available for the composite structures, the equilibration procedures were repeated until the difference in densities obtained from two consecutive compression and relaxation cycles was less than 1%. For all the MD steps, a Berendsen thermostat and barostat with a decay constant of 0.1 ps were employed to control the temperature and pressure during the simulations. The integration time step was 0.9 fs for all the simulations except for membrane models with 25 wt% of AMH-3. The time step for these models was increased to 1.4 fs to reduce the computational time, after performing a trial simulation to ensure that there was no significant difference in the trajectories. The model details for each system are given in Table 2.1. The system sizes are sufficiently large and correctly reproduce the experimentally observed macroscopic behavior, as detailed in the later sections.

**Table 2.1:** Model details for the nanocomposite materials investigated. For each wt % of AMH-3, four different models were constructed, one for each permeant. For example, the first model in the Table had 99 PDMS monomers and 5 He permeant atoms, and had an equilibrated volume of 12.8 nm<sup>3</sup>.

<b>% Wt. AMH-3</b>	<b>No. of monomers</b>	<b>No. of molecules of each penetrant type</b>	<b>Cell volume (nm<sup>3</sup>)</b>
0	(80-99)	5	10.6 ± 0.15 – 13.0 ± 0.14
25	259	13	42.6 ± 1.0
47	99	5	22.5 ± 2.2
70	36	2	11.5 ± 0.08

### 2.2.3. Diffusivity Calculations and Polymer Chain Vibration

The equilibrated model systems were subjected to NVT-MD data production simulations for 500-750 ps at 300 K. Diffusion coefficients were derived from the mean squared displacements of the penetrant molecules. The power-law form of the Einstein equation (Eq. 1) was then used to determine the diffusivity ( $D$ ):

$$\langle |r(t) - r(0)|^2 \rangle = (2dD)t^\alpha \quad (2.1)$$

Here  $r(t)$  and  $r(0)$  are the penetrant displacements at simulation time  $t$  and at time  $t = 0$  respectively,  $d$  ( $= 1, 2$  or  $3$ ) represents the dimensionality of the random walk, and  $\alpha$  is the power law exponent. In applying the Einstein equation to the diffusion trajectory, the effects of anomalous diffusion should be identified to correctly isolate the random walk regime<sup>122</sup>. Anomalous diffusion occurs at short timescales at the beginning of a MD run

and is characterized by fast localized penetrant movement in the ‘holes’ between the polymer chains. Under such conditions the power law exponent is  $\alpha < 1$ . On the other hand, in the normal diffusive regime the penetrant molecules jump between individual holes, and the mean squared displacements increase linearly with time i.e.,  $\alpha \sim 1$ . The diffusion data reported here for each penetrant molecule at different compositions (except 70 wt % AMH-3) is an average of at least 5 individual diffusion trajectories that are verified to be true random walks. For analysis of the polymer chain motions, the NVT-MD simulations were also repeated using a supercell with twice the length in the X and Y directions. By comparing the results obtained from the simulations carried out with a single unit cell, the results were found to be independent of the system size.

#### **2.2.4. Adsorption Isotherm and Diffusivity Calculations in MFI**

MFI crystal structure with lattice parameters of  $x = 20.022 \text{ \AA}$ ,  $y = 19.899 \text{ \AA}$  and  $z = 13.383 \text{ \AA}$  was taken and a supercell consisting of two units cells along z-direction was constructed. For calculating the self-diffusivities of the gas molecules, we performed independent NVT-MD simulations at 300 K with 0.9 fs integration time step for 650 ps with one penetrant molecule per simulation cell. The initial 50 ps of simulation time was utilized for the energy equilibration of the system and the diffusivities were calculated using the latter 600 ps by averaging over six 100ps time blocks of the trajectory data. Self-diffusivities were calculated by fitting Einstein’s equation to the random walk regime of the diffusion trajectory.

Sorption simulations were run by using the Sorption module of Materials Studio 4.0 (Accelrys. Inc.) at experimentally reported temperatures of 295.5 K for N<sub>2</sub> and 305.3 K for O<sub>2</sub>. For the simulations, a 1×1×2 unit cell MFI structure was utilized.

## **2.3. Results and Discussion**

### **2.3.1. Model Evaluation**

Following the construction of equilibrated polymeric and nanocomposite membrane, the models were evaluated for their suitability in MD data production simulations by comparing the simulated and measured densities and diffusivities for the PDMS membrane systems. Visual observation of the equilibrated membrane structures (e.g., Figure 2.2) indicates a uniform segmental distribution through out the packing volume without any unrealistic tensions in the model due to regions of low/high-density packing. The density deviations of the PDMS membrane structures were found to be less than 0.7 % from the experimental value of 0.95 g/cc at a pressure of 1 bar and 300 K, so that the equilibration procedure resulted in physically realistic polymer models. As mentioned in Section 2.2.2, the PDMS/AMH-3 nanocomposite membrane models were subjected to extensive equilibration cycles to attain a stable density value. The resulting material density was found to increase as a function of AMH-3 loading in the material, since AMH-3 is considerably denser than PDMS. At low and moderate loadings of AMH-3, the nanocomposite density (Figure 2.3) follows a mixture rule used to calculate the properties of composite materials<sup>123,124</sup>:  $\rho_c = \rho_p\phi_p + \rho_l\phi_l$ . Here  $\rho_c$ ,  $\rho_p$  and  $\rho_l$  are the densities of the nanocomposite, polymer and inorganic layer respectively, whereas  $\phi_p$  and

$\phi_i$  are the volume fractions of the polymer and layer in the composite material. From Figure 2.3, it is observed that the nanocomposite density shows a deviation of  $\sim 10\%$  from the theoretical prediction at a loading of 70 wt %. This deviation is due to the severe confinement ( $\sim 1$  nm) of the polymer between the layers in this case, as discussed in Section 2.3.4.

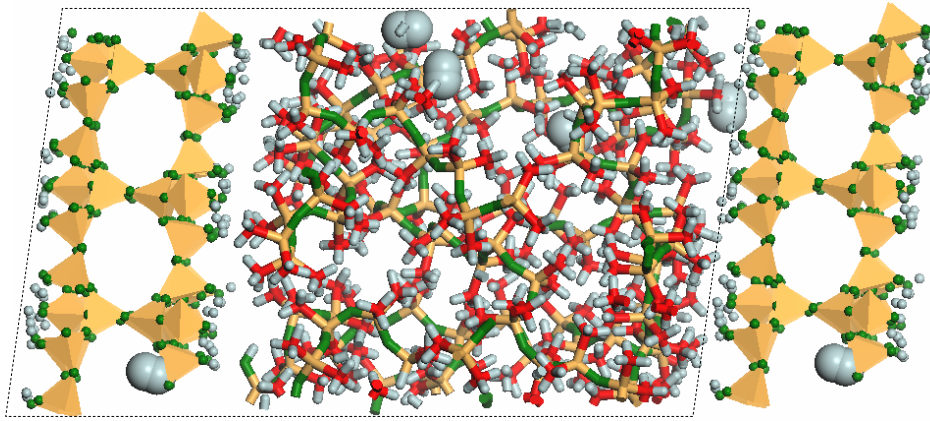


**Figure 2.2:** Snapshot of equilibrated membrane model of PDMS confined between individual AMH-3 layers with H<sub>2</sub> molecules as penetrants. The outline represents the unit cell of the simulation model. H: Grey, C: Red, Si: Orange, O: Green.

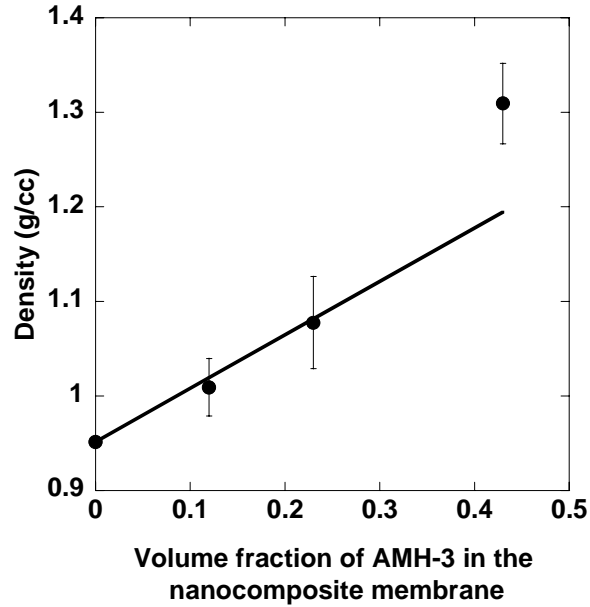


**Figure 2.3:** PDMS/AMH-3 nanocomposite membrane density as a function of AMH-3 loading in the membrane. Solid line denotes theoretical prediction and symbols denote simulated values.

The second step in model evaluation was to compare the simulated diffusivities of the penetrant molecules in PDMS with the available experimental data. Diffusion coefficients of the penetrant molecules were calculated by fitting Eq. 2.1 to the random walk diffusive regimes determined from the mean squared displacements trajectories. Individual penetrant diffusivities obtained by averaging over at least 5 trajectories. The diffusivities calculated in this study were at 300 K, while the experimental diffusivities for PDMS were measured at 308 K. Thus, the experimental data were corrected to 300 K using available activation energy and pre-exponential data<sup>111,112</sup>. Table 2.2 shows the comparison of the simulated diffusivities with those obtained by extrapolating the available experimental data to 300 K. The diffusivities from our study agreed well with the experimental values, and were also found to be in closer agreement with experiment than previously reported simulations<sup>110,125</sup>.

**Table 2.2:** Simulated and extrapolated experimental diffusivities for He, H<sub>2</sub>, N<sub>2</sub> and O<sub>2</sub> in PDMS, and zero-loading diffusivities in MFI at 300 K.<sup>#</sup>

Penetrant	Diffusivities in PDMS				Diffusivities in MFI			
	D <sub>sim</sub> (This work)	D <sub>exp</sub> (308 K) <sup>110</sup>	D <sub>est</sub> (300 K) <sup>111</sup>	D <sub>est</sub> (300 K) <sup>112</sup>	D <sub>Sim</sub> (300 K) <sup>125</sup>	D <sub>sim</sub> (This work)	D <sub>sim</sub> (300 K) <sup>126</sup>	D <sub>sim</sub> (300 K)
He	1.41	----	1.20	0.757	1.19	8.25	7.65	6.58 <sup>97</sup>
H <sub>2</sub>	1.095	1.4	1.097	0.992	----	10.34	----	10.0 <sup>127</sup>
N <sub>2</sub>	0.295	0.34	0.24	0.247	0.12	1.64	1.99	1.35 <sup>‡</sup> /2.05 <sup>†128</sup>
O <sub>2</sub>	0.271	0.34	0.281	0.233	0.18	1.31	1.21	----

<sup>#</sup> Multiply numbers in Table by 10<sup>-8</sup> to obtain diffusivity in m<sup>2</sup>/s.

<sup>126</sup>Self-diffusivities were calculated via MD simulations using the Burchart 1.01-Drieding 2.21 force field.

<sup>97</sup>The interaction between the adsorbed molecules and the adsorbate-zeolite was modeled using a 12-6 Lennard-Jones potential with interaction parameters taken from Chakravarty<sup>129</sup>.

<sup>127</sup>Nonbond interactions (adsorbate-adsorbate and adsorbate-zeolite) were modeled using a pair wise 12-6 Lennard-Jones potential with parameters taken from Buch<sup>130</sup>.

<sup>128</sup>Nonbond interactions were modeled by a 12-6 Lennard-Jones potential in the absence<sup>‡</sup> as well as in the presence of partial charges<sup>†</sup>.

The third step was to assess the performance of the force field for predicting the diffusivities in silicate materials, by simulating the self-diffusivities of He, H<sub>2</sub>, N<sub>2</sub> and O<sub>2</sub> in MFI and comparing them with previously reported MD simulation results that used a variety of force field models<sup>97,126-128</sup>. Table 2.2 shows these comparisons. It appears that the diffusivities of the four gases in MFI are qualitatively insensitive to the differences in the force field models. Further, we performed GCMC simulations to calculate adsorption isotherms of N<sub>2</sub> and O<sub>2</sub> in MFI (Figure 2.4) and compare them to available experimental isotherms<sup>131</sup>. The adsorption isotherm for N<sub>2</sub> is well reproduced, whereas the isotherm for O<sub>2</sub> showed moderate error. Overall, the validation studies strongly suggested that it is productive to use the potential parameters in PCFF (without further tuning) for gas transport studies. However, we caution that these parameters are not validated for calculating other quantities such as the polymer/silicate interfacial energies, which are not the subject of this study.

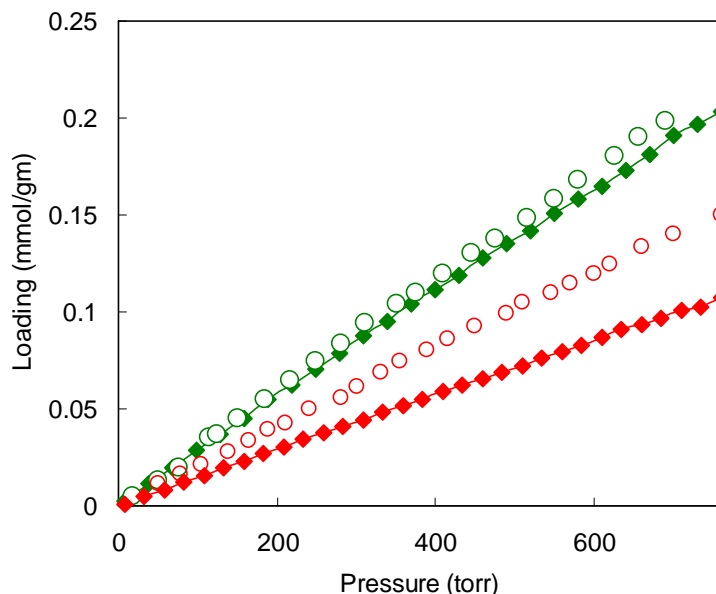


**Figure 2.4:** Adsorption isotherms of N<sub>2</sub> (green) and O<sub>2</sub> (red) in MFI at 295.95 K and 305.3 K, respectively. Diamonds indicate simulated values and open circles indicate reported experimental values<sup>131</sup>.

### 2.3.2. Diffusion through PDMS/AMH-3 Nanocomposites

Analysis of the diffusion trajectories of the four penetrants revealed a random walk diffusion mechanism in both the polymer and the layered silicate structure<sup>121</sup>. Hence, the diffusivities through the nanocomposite material can be calculated using Eq. 2.1 with the overall diffusion trajectories in the material. Diffusion in the nanocomposite material is clearly anisotropic, since the inorganic layers are oriented with their surface normal to Z. Furthermore, the pore structure (and hence the interaction with the penetrants) of layered AMH-3 is different in the Z-direction as compared to the X and Y-directions (in the plane of the layer). Figure 2.5 presents comprehensive data of the overall (isotropic) diffusivities, diffusivities in the XY plane of the layer (i.e., lateral diffusivities), and diffusivities perpendicular to the layer, as a function of AMH-3 weight

fraction. The diffusion of all the penetrant molecules (with the exception of O<sub>2</sub> and N<sub>2</sub> in the models containing 70 wt % AMH-3) reached the random walk regime. Since the diffusion in the Z-direction for O<sub>2</sub> and N<sub>2</sub> in the 70 wt % AMH-3 nanocomposite did not attain the random walk regime within the simulation times, the data for this case is not reported. In the case of pure PDMS, there are slight deviations of the XY- and Z-directional diffusivities from the isotropic diffusivities of the penetrants in the bulk PDMS model. If the constructed PDMS model was perfectly isotropic, these diffusivities would all be equal; however, in practice this cannot be achieved with a finite-size simulation cell in the case of an amorphous system. For this reason, the error bars on the reported data are also higher than those typically reported for crystalline systems. The prediction of the isotropic diffusivity statistically averages out these spatial heterogeneities to a large degree.

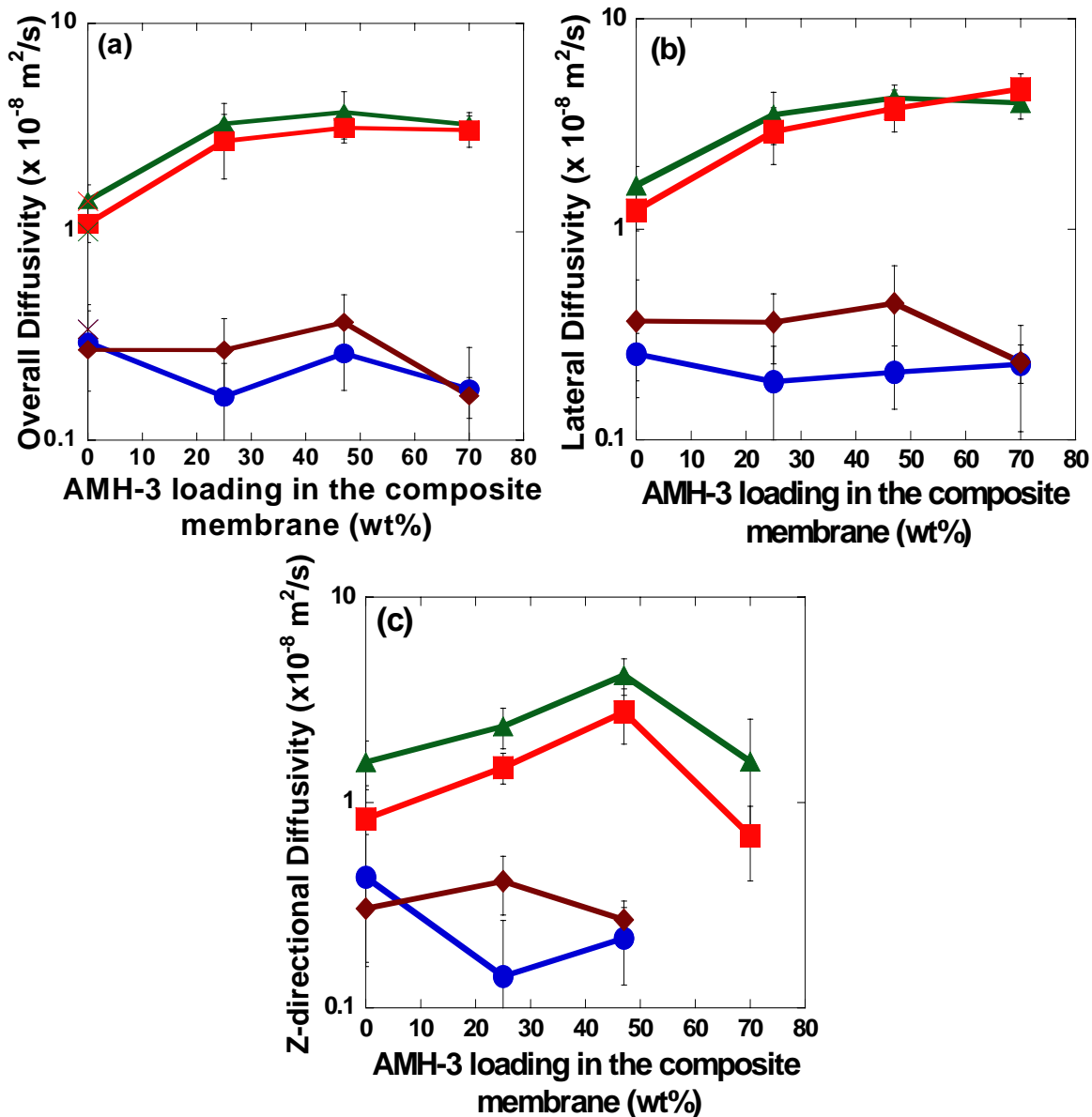


**Figure 2.5:** (a) Overall (isotropic) diffusivities, (b) Lateral (XY-plane) diffusivities, and (c) Z-directional diffusivities of He ( $\blacktriangle$ ), H<sub>2</sub> ( $\blacksquare$ ), N<sub>2</sub> ( $\bullet$ ) and O<sub>2</sub> ( $\blacklozenge$ ) in PDMS/AMH-3 nanocomposite membrane as a function of AMH-3 loading in the membrane. ( $\times$ ) denote experimental diffusivities of He, H<sub>2</sub>, N<sub>2</sub> and O<sub>2</sub> in pure PDMS at 300 K.

The results suggest that the diffusivities of He and H<sub>2</sub> increase significantly upon addition of nanoporous AMH-3. The overall diffusivities (Figure 2.5(a)) of these penetrants exhibit a dependency on the layer loading up to a value of 47 wt %, after

which a further increase in the inorganic content does not affect the diffusivities significantly. A similar trend is observed for the lateral diffusivity of He and H<sub>2</sub> (Figure 2.5(b)). However, the Z-direction diffusivities of He and H<sub>2</sub> pass through a maximum as a function of the inorganic layer loading (Figure 2.5(c)). For O<sub>2</sub> and N<sub>2</sub>, there is a much less appreciable change in diffusivity with AMH-3 loading. The observed changes in the penetrant diffusivities in the PDMS/AMH-3 nanocomposite in comparison to pure PDMS can be attributed to the ‘molecular sieving’ effect of the AMH-3 layer. As can be seen from Figure 2.6, the eight-membered rings (8MRs) of AMH-3 have pore openings with a limiting dimension of 3.4 Å and thus can show selectivity for molecules of small kinetic diameter such as He (2.6 Å) and H<sub>2</sub> (2.9 Å)<sup>42,132</sup>. These penetrants also spend significant time in lateral motion within the 3D porous AMH-3 layer, resulting in an increase in lateral diffusivities of the molecules compared to the Z-directional diffusivities. On the other hand, molecules with kinetic diameters larger than the smallest pore dimension, e.g. O<sub>2</sub> (3.5 Å) and N<sub>2</sub> (3.7 Å), will diffuse more slowly through the AMH-3 layer. These molecules also diffuse more slowly in PDMS than He and H<sub>2</sub>, and hence there is little appreciable change in their diffusivity through the nanocomposite material. Due to the infinite aspect ratio of the layered material (created by periodic boundary conditions), the penetrants must either diffuse through the layer or restrict their motion to the polymer and interfacial regions of the material. For these reasons, the PDMS/AMH-3 nanocomposite membranes do not show an enhancement in the diffusivities of O<sub>2</sub> and N<sub>2</sub> compared to pure PDMS. As a result, there is a substantial enhancement of selectivity between certain pairs of molecules (see next sub-section). Finally, the maxima in the Z-directional diffusivities and the plateau in the overall and lateral diffusivities of He and H<sub>2</sub> can be

explained in terms of the changes in the (vibrational) mobility of the polymer chains as a function of increasing confinement between the inorganic layers. This is explained in further detail in the Section 2.3.4.

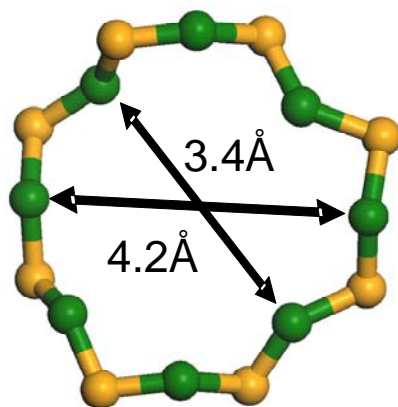


**Figure 2.6:** 8-membered ring (8MR) of AMH-3 showing the largest and the smallest (limiting) pore dimensions. Si: Orange, O: Green.

### 2.3.3. Diffusion Selectivities

Figures 2.7(a)-(b) show the overall (isotropic) and Z-directional diffusion selectivities for three gas molecule pairs ( $\text{H}_2/\text{N}_2$ ,  $\text{H}_2/\text{O}_2$ ,  $\text{O}_2/\text{N}_2$ ) at different compositions of AMH-3 in the material <sup>121</sup>. The  $\text{H}_2/\text{N}_2$  and  $\text{H}_2/\text{O}_2$  selectivities in the nanocomposite are significantly enhanced over pure PDMS, indicating that the presence of the inorganic layer is beneficial for membrane-based separations involving these mixtures. As explained in the Section 2.1, the isotropic and Z-directional selectivities approximate the performance of randomly oriented and perfectly oriented layers, respectively. Since our study investigates the ideal case of infinite aspect ratio of the layers, the results from our

study should be treated as upper bound estimates for diffusion through the two types of nanocomposite membranes shown in Figure 2.1(b) and 2.1(c). The isotropic diffusion selectivities shown in Figure 2.7(a) present upper bound estimates for selectivities that can be attained in a membrane containing randomly oriented AMH-3 layers, since the simulations incorporate the ‘bypassing’ motion of penetrants parallel to the layer. On the other hand, the Z-directional diffusivities (Figure 2.7(b)) provide an upper bound on the performance of a membrane containing AMH-3 layers oriented parallel to the membrane surface. We note that such an analysis is not valid for the limiting case of infinite selectivity of molecules through the inorganic layers (i.e., larger penetrants that exhibit no diffusion through the porous inorganic layers), as the larger penetrants cannot ‘bypass’ the infinitely long inorganic layers in the ideal microstructure investigated here.

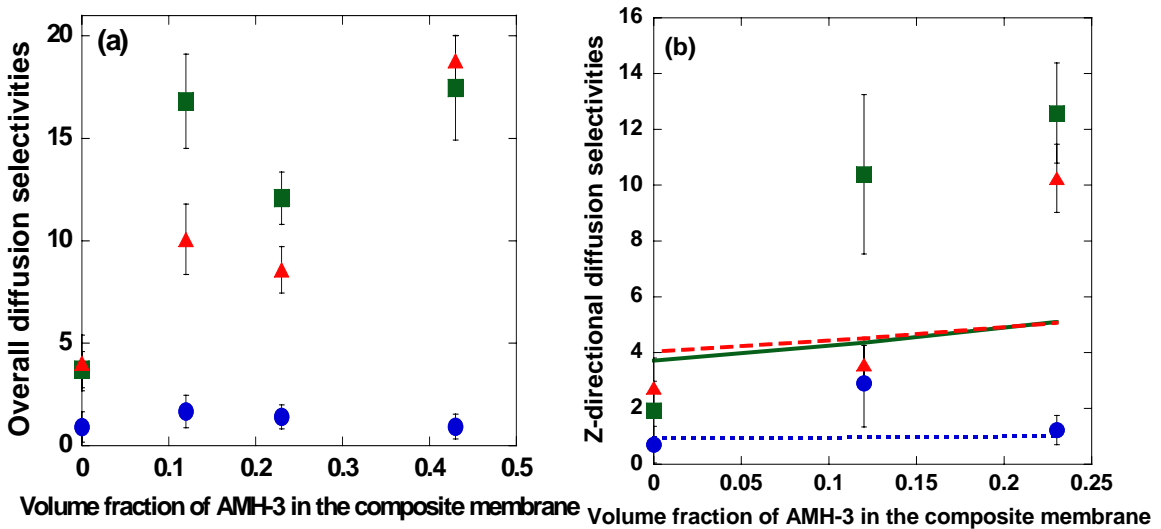


**Figure 2.7:** (a) Overall (isotropic) diffusion selectivities of H<sub>2</sub>/N<sub>2</sub> (■), H<sub>2</sub>/O<sub>2</sub> (▲) and O<sub>2</sub>/N<sub>2</sub> (●) systems as a function of AMH-3 loading in the membrane. (b) Z-directional diffusion selectivities of the penetrants in the PDMS/AMH-3 nanocomposite membrane. Cussler model predictions are indicated as (—) for H<sub>2</sub>/N<sub>2</sub>, (---) for H<sub>2</sub>/O<sub>2</sub> and (---) for O<sub>2</sub>/N<sub>2</sub>.

It is also of interest to compare the selectivity of a true nanocomposite material (as simulated in this study) with models developed for composite membranes containing high-aspect-ratio ‘flakes’ of ‘bulk’ thickness incorporated in a polymer. In particular, we consider the application of the Cussler model<sup>133</sup> to the nanocomposite. The model was developed for the case of oriented flakes with finite aspect ratio, and can be extrapolated to infinite aspect ratios. In the latter case, the Cussler model reduces to a resistances-in-series model with the diffusion selectivity ( $S_{21}$ ) for permeant 2 with respect to permeant 1 predicted as follows:

$$S_{21} = \frac{J_2}{J_1} = \left( \frac{D_2}{D_1} \right) \left( \frac{1 + \phi(\delta_1 - 1)}{1 + \phi(\delta_2 - 1)} \right) \quad (2.2)$$

Here  $J$  is the penetrant flux through the composite membrane,  $D$  is the diffusivity of the penetrant in the polymer,  $\phi$  is the inorganic volume fraction and  $\delta$  is the ratio of penetrant diffusivity in the polymer to the diffusivity in the inorganic flake, i.e.,  $\delta = D_{polymer} / D_{flake}$ . Note that the model assumes the solubilities of both penetrants to be equal. This is also implicitly assumed in the present study, since the nanocomposite unit cells are loaded with the same numbers of each penetrant for each of the MD runs. The diffusivities of the gas molecules through the polymer and AMH-3 layer were obtained by following the penetrant diffusion trajectories in the nanocomposite membrane and isolating the portions of the trajectory spent by the penetrant in the polymer and layered silicate, respectively. Due to the three-dimensionally porous slab-like structure of the layered silicate AMH-3, the penetrants exhibit random walk diffusive motion of the type observed in bulk

nanoporous materials like zeolites<sup>134,135</sup>. In other words, it was found that AMH-3 retains vestiges of ‘bulk’ behavior due to its 3-D porosity, so that it is still possible to obtain random walk isotropic diffusivities within a single layer. Hence, diffusion coefficients can be estimated from the mean squared displacements of the penetrants by applying Eq. 2.1, albeit with significant statistical uncertainty. The isotropic diffusivities in the layer, obtained by analyzing 10 random walk trajectories for each penetrant, are:  $D_{H_2} = 3.88(\pm 1.156) \times 10^{-8}$ ,  $D_{N_2} = 1.56(\pm 0.693) \times 10^{-9}$  and  $D_{O_2} = 1.98(\pm 0.955) \times 10^{-9}$  m<sup>2</sup>/s.

Figure 2.7(b) compares the selectivities predicted by the resistances-in-series model and simulated selectivities for the chosen gas mixtures to illustrate the performance of the model for “nano”-scale constituent materials. Note that all parameters in the model are directly obtained from the MD simulations, and there are no fitting parameters. The predicted selectivities from the resistances-in-series model are much lower than the H<sub>2</sub>/N<sub>2</sub> and H<sub>2</sub>/O<sub>2</sub> selectivities obtained from the MD simulations. Cussler’s model was developed assuming a composite formed from two isotropic bulk materials, so that the isotropic diffusivities can be employed in Eq 2.2. However, when one of the dimensions of the inorganic material is reduced to the nanometer scale, the isotropic diffusivity fails to represent the transport accurately. The diffusion jump lengths of the permeants now become comparable to the thickness (~ 1 nm) of the layer. The resistance-in-series model appears to predict the selectivities (~ 1) for the O<sub>2</sub>/N<sub>2</sub> pair, but this agreement may be trivial since there is no diffusion selectivity for this pair in the present case.

#### 2.3.4. PDMS Segmental Dynamics

It is well known that penetrant transport through a rubbery polymer like PDMS is strongly influenced by the vibrational mobility of the polymer chains. Diffusion of the penetrants is aided by the transient appearance of microscopic ‘holes’ and ‘channels’ in the polymer. In the nanocomposite material, these polymer motions can be affected by confinement between the inorganic layers, with a resultant effect on the diffusion of permeants. The motion of the polymer chains is quantified by the average mean squared displacement of all the polymer atoms in the model. Figures 2.8(a) and (b) show the lateral (XY) and Z-directional PDMS segmental motion as a function of AMH-3 loading in the membrane <sup>121</sup>. The initial sharp increase is due to the transient motion of the polymer atoms, which leads to a plateau with increasing time as the polymer vibrates about a quasi-equilibrium position. The small upward slopes at longer times are due to the onset of slow diffusive motions of the polymer chains, which cannot be captured on the time scale of MD simulations and which do not appreciably affect the fast diffusion of gas molecules. Within the limits of statistical variation, the lateral and Z-directional motions are not significantly affected by the AMH-3 layers at low and moderate loadings. However, there is a sharp decrease in the vibrational motion of the PDMS chains at the high AMH-3 loading of 70 wt %, which marks the rigidification of the PDMS chains due to strong polymer-inorganic interactions under severe confinement (in a space of ~1.2 nm) between two AMH-3 layers. This is correlated with the sharp decrease in the diffusivities of He and H<sub>2</sub> in the nanocomposite at this loading.

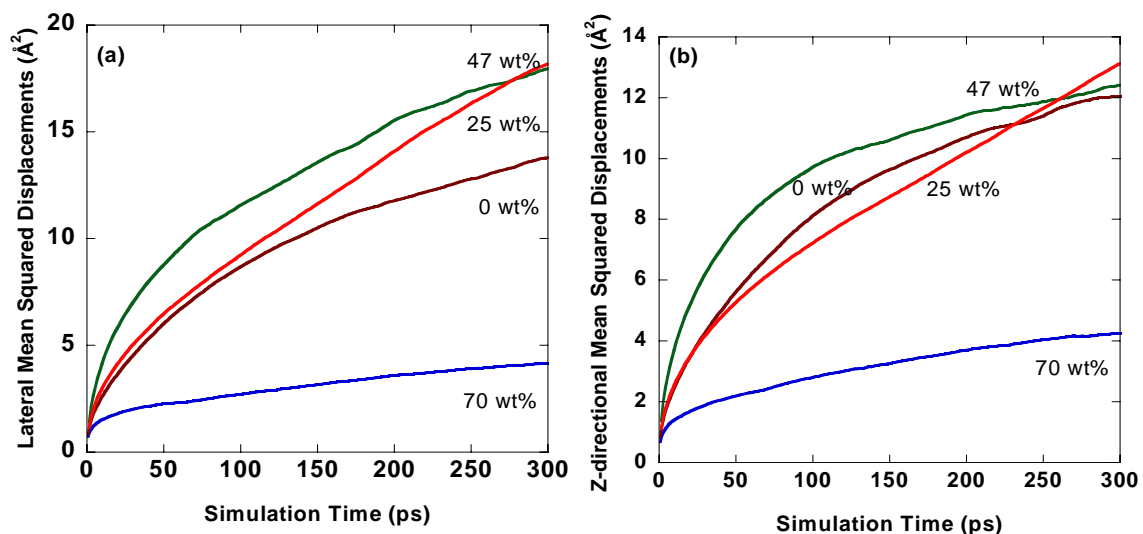


**Figure 2.8:** (a) Lateral and (b) Z-directional segmental motion of all polymer atoms in the nanocomposite membrane as a function of increasing confinement between the AMH-3 layers.

The above argument is further strengthened by considering the mean squared displacements of the polymer atoms in consecutive ‘slices’ of 0.5 nm thickness at different distances from the functional layer. For example, Figure 2.9(a) shows the mean square displacements for five slices in the 25 wt % nanocomposite. Slice 1 is at the polymer-inorganic interface, while slice 5 is in the central region of the polymer confined between the AMH-3 layers. There is no appreciable difference between slices 5, 4, and 3 which are located far from the interface. However, within a distance of  $\sim 1$  nm from the interface (i.e., slices 2 and 1), there is a considerable rigidification of the polymer chain, with mean squared displacements Z comparable to those seen in Figures 2.8(a) and 2.8(b) for the 70 wt % nanocomposite. Figure 2.9(b) shows a similar analysis performed for pure PDMS, to examine the possibility of any simulation artifacts. As expected, the different slices have no appreciable difference in polymer mobility, thus clearly indicating that the observed effects in the nanocomposite are physical and are caused by

short-range polymer-layer interactions. This conclusion is further corroborated by previous computational investigations that showed a reduction in polymer motion near clay and zeolite surfaces<sup>102,107,136,137</sup>. The current results further show the utility of atomistic simulations in developing structure-property relations in nanocomposite membranes, wherein nanoscale confinement effects alter the properties of the polymer and preclude a simple extrapolation of the nanocomposite properties from the bulk properties of the constituent materials.

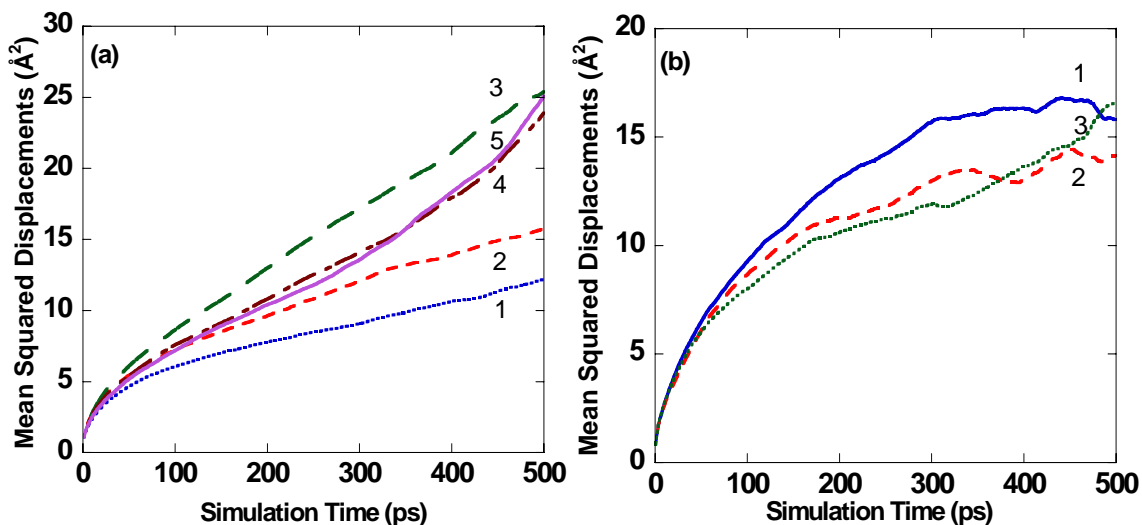


**Figure 2.9:** (a) Polymer mobility in the nanocomposite with 25wt% of AMH-3. Slice 1 is closest to the AMH-3 layer and slice 5 is the farthest. (b) Polymer mobility in different slices in a pure PDMS model.

## 2.4. Conclusions

In this study, it has been computationally shown that transport in polymer/porous inorganic layered silicate nanocomposite membranes can be controlled by several

quantifiable factors such as the inorganic content, the molecular sieving ability of the layer, the transport properties of the polymeric material, and the microstructure of the membrane. For example, in the case of penetrants like He and H<sub>2</sub> which diffuse fast in PDMS, the molecular sieving properties of the inorganic material AMH-3 allow a considerable increase in selectivity (with respect to slower molecules like N<sub>2</sub> and O<sub>2</sub>) as a function of loading. In the case of penetrant pairs such as N<sub>2</sub> and O<sub>2</sub> which diffuse more slowly through PDMS and also cannot be efficiently separated by the AMH-3 layer, the nanocomposite membrane does not offer an increase in selectivity in comparison to pure PDMS. At higher inorganic loadings, the transport properties are affected by rigidification of the polymer chains due to strong confinement between the layers. By careful choice of the polymeric and functional inorganic materials, the transport properties of the nanocomposite membranes can be tailored to attain superior permselectivity properties. However, the structure-property relations in these materials cannot be reliably inferred from those of the individual constituent materials (in their bulk form) or from those of conventional composites of the constituents. Atomistic simulations of idealized nanocomposite membranes can thus provide valuable guidance by predicting the performance of candidate systems as a function of the structural and compositional factors that influence transport properties. Such predictions, even if semi-quantitative, can be used to direct synthesis efforts towards suitable nanocomposite materials among the increasing number of potential nanoporous layered material/polymer combinations.

# CHAPTER 3

## DEVELOPMENT OF A FORCE FIELD FOR MODELING NANOPOROUS LAYERED ALUMINOPHOSPHATES

### 3.1. Introduction

Layered aluminophosphate (AIPO) materials are a new class of synthetic AIPOs that have potential applications in catalysis<sup>138</sup>, ion exchange, sorption<sup>139</sup>, and membrane technology<sup>42</sup>. Unlike the neutral microporous framework AIPOs with Al/P stoichiometry of 1, layered AIPOs are anionic and exhibit a variety of distinct structures and compositions owing to their Al/P stoichiometry ratio  $< 1$ . The anionic AIPOs contain  $\text{AlO}_4$  tetrahedra with occasional substitution of the tetrahedra with five- ( $\text{AlO}_5$ ) or six- ( $\text{AlO}_6$ ) coordinated Al atoms, and  $\text{PO}_4$  tetrahedra with one, two, three or four oxygen atoms bridging with the Al atoms to form AIPO materials with varying Al/P ratios<sup>140-142</sup>. These materials are synthesized *via* non-aqueous phase chemistry in the presence of an organic cation template to form one-dimensional (1-D) chains, two-dimensional (2-D) layers, or three-dimensional (3-D) open framework materials<sup>143-153</sup>. The dimensionality and composition of the AIPO materials is influenced by the organic amine cations that function as structure-directing agents to form AIPO materials with distinct structural architecture and porosity based on the size and shape of the cations<sup>154</sup>. The organic amine template molecules interact with AIPO framework *via* H-bonding and as a consequence the 1-D chains and 2-D layer structures can potentially be delaminated or the cations in 3-D frameworks can be exchanged to enable new applications as superior catalysts or construction of novel nanocomposite membrane materials. Here, we are

interested in 2-D layered porous AlPO materials as molecular sieves for use in construction of permselective polymer/inorganic layered nanocomposite membrane materials.

As demonstrated in Chapter 2, predictions of structure-transport property relations in nanocomposite materials using atomistic simulations rely on accurate force fields that can reliably describe the structure of individual components of the nanocomposite as well as the nanocomposite structure<sup>121</sup>. Previous efforts on force field development for AlPO systems focused on deriving interatomic interactions for 3-D neutral framework AlPO materials that have a structural chemistry different from layered AlPOs. On the other hand, the objective of the present study is to develop a force field for estimating the properties of a class of 2-D layered and 1-D chains of AlPOs with Al/P ratio of 3:4. The structure of these AlPO materials is composed of alternating  $\text{AlO}_4$  and  $\text{PO}_3(=\text{O})$  tetrahedra linked to form a layered AlPO network with organic cations in the interlayer spacing. A basic structural difference between these anionic AlPOs and neutral framework AlPOs is the presence of terminal double bonded phosphoxy bonds that has a shorter P=O bond length and larger O-P=O bond angle compared to the nominal tetrahedral P-O bond lengths and O-P-O bond angles<sup>142-153</sup>. Consequently, the force field parameters for terminal double bonded phosphoxy oxygen atoms will be different from the bridging single bonded phosphoxy oxygen atoms.

Our approach involves employing the existing force field parameters for neutral framework AlPOs, add new parameters for double bonded oxygen atoms and optimize

the parameters based on the crystal structures of layered AlPOs. The functional form of the force field is in accordance with the polymer consistent force field (PCFF) and is based on an ionic model containing Lennard-Jones (9-6) term coupled with electrostatic potential to describe the metal-oxygen interactions. The idea is to develop a simple force field that is easily transferable to other 1-D chains or 2-D layered AlPOs possessing the same stoichiometry albeit with different structural architecture and pore network. We validate the force field by comparing (i) structural properties, (ii) X-ray diffraction (XRD) patterns, and (iii) vibrational spectra between the predicted and experimental crystal structures of a variety of AlPO structures.

## **3.2. Methodology**

### **3.2.1. Computational Details**

#### **3.2.1.1. Force field Parameterization**

The functional form of the force field is based on the PCFF<sup>117,155</sup> force field with fractional charges assigned to each atom and 9-6 Lennard Jones (LJ) potential with 6<sup>th</sup> order combination rules to describe the Al-O, P-O, P=O and O-O interactions.

$$E = \frac{e^2}{4\pi\epsilon_o} \sum_{i \neq j} \frac{q_i q_j}{r_{ij}} + \sum_{i \neq j} \epsilon_{ij} \left[ 2 \left( \frac{r_{o,ij}}{r_{ij}} \right)^9 - 3 \left( \frac{r_{o,ij}}{r_{ij}} \right)^6 \right] \quad (3.1)$$

$$\text{Where } r_{o,ij} = \left( \frac{r_{o,i}^6 + r_{o,j}^6}{2} \right)^{\frac{1}{6}} \text{ and } \varepsilon_{ij} = 2\sqrt{\varepsilon_i \cdot \varepsilon_j} \left( \frac{r_{o,i}^3 \cdot r_{o,j}^3}{r_{o,i}^6 + r_{o,j}^6} \right)$$

For the organic amine template molecules, we adopted the complete potential model along with the force field parameters of the PCFF, which has been parameterized for organic and polymer molecules<sup>114,115,155-158</sup>. The initial estimates of partial charges and LJ parameters ( $\varepsilon$  and  $\sigma$ ) for Al, P, and O atoms in the layered AIPO network were obtained from the parameters for neutral framework AIPOs developed by van Beest et al.<sup>159</sup>. The 9-6 LJ parameters for framework AIPOs were optimized from reported Buckingham potential parameters using nonlinear least squares fit of the 9-6 LJ potential model to the Buckingham equation. The partial charges for Al, P and the bridging O atoms were assigned to be the same as the atoms in framework AIPOs. The initial values of 9-6 LJ parameters for Al, P and bridging O atoms were then optimized using the General Utility Lattice Program, GULP<sup>160</sup>, which employs nonlinear least squares analysis and energy minimization to fit the force field predictions to the experimental crystal structures of neutral framework AIPOs. Initially, berlinite (Hexagonal space group P3121 and lattice parameters  $a = b = 4.9423 \text{ \AA}$ ,  $c = 10.9446 \text{ \AA}$ ,  $\alpha = \beta = 90^\circ$ ,  $\gamma = 120^\circ$ )<sup>161</sup> was used in the parameter optimization procedure. The potential parameters were further refined by including the crystal structures of AIPO-18 (monoclinic space group C2/C and lattice parameters  $a = 13.711 \text{ \AA}$ ,  $b = 12.732 \text{ \AA}$ ,  $c = 18.571 \text{ \AA}$ ,  $\alpha = \gamma = 90^\circ$ ,  $\beta = 90^\circ$ )<sup>162</sup>, AIPO-31 (hexagonal space group R-3 and lattice parameters  $a = b = 20.82699 \text{ \AA}$ ,  $c = 5.003 \text{ \AA}$ ,  $\alpha = \beta = 90^\circ$ ,  $\gamma = 120^\circ$ )<sup>163</sup>, and AIPO-41 (orthorhombic space group CMC21 and lattice parameters  $a = 9.72 \text{ \AA}$ ,  $b = 5.831 \text{ \AA}$ ,  $c = 8.36 \text{ \AA}$ ,  $\alpha = \beta = \gamma = 90^\circ$ )<sup>164</sup> in the fitting

procedure. Once a good agreement was ensured between the experimental and predicted neutral framework AlPOs (i.e. maximum deviation in unit cell parameters  $\sim 3.2\%$ , bond lengths and angles  $\sim 4\%$ ), the resulting LJ parameters were then optimized for layered AlPOs materials. To begin with, the LJ parameters for the two O types in layered AlPOs were kept the same while the partial charge for the terminal double bonded phosphoxy O atoms was obtained *via* charge balance on the layered AlPO unit cell formula of  $[\text{Al}_3\text{O}_{12}\text{P}_4(=\text{O})_4]^{-3}$ . This parameter set gave a good prediction of layered AlPO structures with an exception of the P=O bond lengths that exhibited a deviation of  $>4\%$  from the experimental values. Hence, the LJ parameters for the double bonded terminal phosphoxy oxygen atoms were optimized using Materials Studio 3.2 molecular simulation program (Accelrys, Inc) by tuning the parameters in small (de-)increments ( $\sim 10\%$ ) until the predicted structure approximated the experimental crystal structure of layered AlPO with a triethylamine template ( $[\text{Al}_3\text{P}_4\text{O}_{16}]^{3-} \cdot 3[\text{CH}_3\text{CH}_2\text{NH}_3]^+$  monoclinic space group P21/m and lattice parameters  $a = 8.92 \text{ \AA}$ ,  $b = 14.896 \text{ \AA}$ ,  $c = 9.363 \text{ \AA}$ ,  $\alpha = \gamma = 90^\circ$ ,  $\beta = 106.07^\circ$ )<sup>149</sup>. The crystal structures of AlPO-triethylenetetramine ( $[\text{Al}_3\text{P}_4\text{O}_{16}][\text{C}_6\text{H}_{21}\text{N}_4]$  monoclinic space group P21/c and lattice parameters  $a = 9.55 \text{ \AA}$ ,  $b = 24.064 \text{ \AA}$ ,  $c = 9.601 \text{ \AA}$ ,  $\alpha = \gamma = 90^\circ$ ,  $\beta = 97.99^\circ$ )<sup>165</sup>, and AlPO-2-methylpiperazine ( $[\text{Al}_6\text{P}_8\text{O}_{32}]3 \cdot [\text{C}_5\text{N}_2\text{H}_{14}]$  trigonal space group P3 and lattice parameters  $a = b = 13.22 \text{ \AA}$ ,  $c = 9.533 \text{ \AA}$ ,  $\alpha = \beta = 90^\circ$ ,  $\gamma = 120^\circ$ )<sup>166</sup> were also added to further refine the force field parameters. Table 3.1 shows the final list of parameters. To validate the force field we compared (i) computed structural properties of a variety of layered AlPO models with similar or varying pore network and different template molecules with the experimental crystal structures, (ii) computed vibrational spectra of layered AlPO-triethylamine and AlPO-isopropanolamine with the

corresponding FTIR spectra, and (iii) computed X-ray diffraction (XRD) patterns of the predicted structures with computed XRD of solved crystal structures.

**Table 3.1:** Force field parameters for layered aluminophosphates with Al/P ratio of 3:4.

Species	Charge (e)	$E$ (kcal/mol)	$R_o$ (Å)
Tetrahedral Al	1.4	$8.7677 \times 10^{-5}$	4.0441
Tetrahedral P	3.4	$2.1697 \times 10^{-5}$	5.0244
Bridging oxygen between tetrahedral Al and tetrahedral P	-1.2	0.1076	3.8661
Double bonded phosphoxy oxygen	-1.6	0.1476	3.8661

### 3.2.1.2. Molecular Dynamics (MD) simulations

Atomistic models of 7 different layered AlPO structures along with the template molecules were constructed using published crystal structure data. All molecular simulations were performed on single unit cell structures of layered AlPOs with P1 symmetry using the Discover module of Materials Studio 3.2. The structures were initially subjected to energy minimizations with steepest descent, conjugate gradient, and Newton-Raphson algorithms until the maximum energy gradient at any atom was below 1 kcal/mol/Å. The unit cell parameters were allowed to relax during the energy minimizations and the normal-mode vibrational frequencies were calculated. The optimized structures were then subjected to equilibration NPT MD simulations at 1 bar

and 298 K with a 0.9 fs integration time step for 50 ps. A Berendsen thermostat and barostat with a decay constant of 0.1 were used to control the temperature and pressure, respectively. The energy and temperature of the systems was found to be equilibrated typically within 5-10 ps. Five independent energy minimization and MD simulations were performed on each structure and the results were averaged to obtain the predicted unit cell parameters, bond lengths and angles.

The X-ray diffractions (XRD) patterns were computed using the Reflex module of Materials Studio 3.2 by employing a Cu radiation source. The XRD patterns were calculated on solved crystal structures and were compared with the structures predicted using the current force field between a  $2\theta$  range of 5 and 40°. A Pseudo-Voigt function was employed to obtain the intensity profile.

### **3.2.2. Experimental Details**

#### **3.2.2.1. Fourier Transform Infrared Spectroscopy (FTIR)**

Powdered materials of layered AIPO-triethylamine and AIPO-isopropanolamine were synthesized and purified as described in the literature<sup>149,167</sup>. The solid samples were then used for measuring the FTIR spectra. The spectra were collected using a Bruker IFS 55v/S spectrometer with a resolution of 4 cm<sup>-1</sup> at 20°C. In order to provide a proper comparison between the absorption peak positions in the FTIR spectra and the corresponding computed vibrational bands from normal-mode analysis, the FTIR spectra of the layered AIPOs were deconvoluted into a series of Gaussian curves using least

squares analysis with the peak position of the Gaussians corresponding to the absorption peaks in FTIR spectra.

### **3.3. Results and Discussion**

#### **3.3.1. Structural Property Evaluation**

To evaluate the performance and to test the transferability of the developed force field, we simulated the structures of a variety of 2-D and 1-D layered AIPOs with Al:P ratio of 3:4 and compared the structural properties with the experimental data. In addition to the layered AIPOs employed in the force field parameterization, the structural properties of 1-D chain like AIPO-trimethylamine ( $[\text{Al}_3\text{P}_4\text{O}_{16}]^{3-} \cdot 3 \cdot [\text{CH}_3\text{NH}_3]^+$  triclinic space group P-1) <sup>168</sup>, 2-D layered AIPO-isopropanolamine ( $[\text{Al}_3\text{P}_4\text{O}_{16}]^{3-} \cdot 3 \cdot [\text{NH}_3\text{CH}_2\text{CH}(\text{OH})\text{CH}_3]^+$  trigonal space group R-3) <sup>167</sup>, 2-D layered AIPO-piperidinium+cyclobutylammonium ( $[\text{Al}_3\text{P}_4\text{O}_{16}]^{3-} \cdot [\text{C}_4\text{H}_7\text{NH}_3]^{2+} \cdot [\text{C}_5\text{H}_{10}\text{NH}_2]^+$  monoclinic space group P21) <sup>169</sup>, and 2-D layered AIPO-diaminopentane+piperidinium ( $[\text{Al}_3\text{P}_4\text{O}_{16}]^{3-} \cdot [\text{NH}_3(\text{CH}_2)_5\text{NH}_3]^{2+} \cdot [\text{C}_5\text{H}_{10}\text{NH}_2]^+$  monoclinic space group P21/c) <sup>170</sup> were also computed. The layered AIPOs under consideration differ in AIPO structural network containing 4- $\times$ 6- $\times$ 8- membered rings (MR), 4- $\times$ 6- $\times$ 12- MR or 6- $\times$ 8-MR, pore sizes, and template molecules occupying the interlayer spacings. Table 3.2 provides a summary of structural property comparison between the predicted and experimental crystal structures of layered AIPOs. The structural predictions from the force field are in good agreement with the experimental data with maximum deviations in unit cell parameters being  $\sim$ 3.6%, while bond lengths and angles exhibit a maximum deviation of  $\sim$ 2%. The accuracy of the

predictions obtained using our force field is typical of the force fields reported previously for inorganic clay or zeolites materials<sup>159,171-175</sup>. Comparison of the pore structures as well as the pore sizes of all the 4-, 6-, 8-, and 12- membered rings in the different layered AlPOs suggests a close approximation between the simulated and experimental crystal structures as observed from the snapshots of Figure 3.1. We note that the computed densities of layered AlPO materials indicated in Table 3.2 are in general lower (except for AlPO-Isopropanolamine) than the experimental values. This is due to an increase (~1-2%) in the interlayer distances in the structure that are in turn controlled by H-bonding between the terminal phosphoxy oxygens and protons of the ammonium group in the organic cation molecules. The force field parameters for the organic molecules were directly adopted from PCFF and hence no attempt was made to tune the nonbonded interactions of the protons on ammonium group. On the other hand, the current force field is based on a simple LJ and electrostatic potentials. Hence, any attempt to further tune the quality of the interaction parameters of phosphoxy oxygen atom resulted in poor structural prediction of layered AlPOs. Overall, the structure validation study suggests the applicability of the force field to the current layered AlPO systems.

**Table 3.2:** Structural property predictions in layered AIPOs

Structural parameter	AIPO-triethylamine		AIPO-2-methylpiperazine		AIPO-triethylenetetramine		AIPO-trimethylamine	
	Simulation	Expt	Simulation	Expt	Simulation	Expt	Simulation	Expt
a axis (Å)	$8.93 \pm 0.065$	8.92	$13.35 \pm 0.044$	13.22	$9.76 \pm 0.066$	9.55	$8.35 \pm 0.26$	8.37
b axis (Å)	$15.13 \pm 0.11$	14.9	$13.35 \pm 0.044$	13.22	$24.59 \pm 0.168$	24.06	$11.38 \pm 0.35$	11.27
c axis (Å)	$9.60 \pm 0.07$	9.36	$9.82 \pm 0.033$	9.53	$9.67 \pm 0.066$	9.60	$11.68 \pm 0.36$	11.46
$\alpha$ angle (deg)	$90 \pm 0.0$	90	$90 \pm 0.0$	90	$90 \pm 0.0$	90	$75.01 \pm 0.0$	72.4
$\beta$ angle (deg)	$107.56 \pm 0.0$	106.7	$90 \pm 0.0$	90	$100.18 \pm 0.0$	97.99	$90.18 \pm 0.0$	89.45
$\gamma$ angle (deg)	$90 \pm 0.0$	90	$120 \pm 0.0$	120	$90 \pm 0.0$	90	$83.37 \pm 0.0$	85.35
density (g/cc)	$1.61 \pm 0.04$	1.664	$1.35 \pm 0.02$	1.413	$1.77 \pm 0.04$	1.852	$1.78 \pm 0.16$	1.801
Al-O (Å)	$1.729 \pm 0.089$	1.728	$1.719 \pm 0.112$	1.717	$1.711 \pm 0.101$	1.74	$1.705 \pm 0.11$	1.729
P-O (Å)	$1.536 \pm 0.045$	1.536	$1.532 \pm 0.048$	1.528	$1.533 \pm 0.049$	1.536	$1.534 \pm 0.05$	1.533
P=O (Å)	$1.471 \pm 0.061$	1.492	$1.464 \pm 0.039$	1.492	$1.507 \pm 0.136$	1.488	$1.484 \pm 0.03$	1.488
O-Al-O (deg)	$109.44 \pm 9.08$	109.67	$108.97 \pm 10.19$	109.46	$109.97 \pm 11.6$	109.56	$111.18 \pm 11.86$	109.47
O-P-O (deg)	$106.68 \pm 3.89$	108.43	$106.50 \pm 4.51$	108.0	$107.37 \pm 4.05$	108.56	$107.40 \pm 6.02$	108.42
O-P=O (deg)	$112.11 \pm 3.57$	111.27	$112.8 \pm 5.44$	112.34	$111.42 \pm 4.59$	111.13	$111.24 \pm 5.24$	111.14

**Table 3.2:** Continued

Structural parameter	AlPO-isopropanolamine		AlPO-piperidinium+cyclobutylammonium		AlPO-diaminopentane+ piperidinium	
	Simulation	Expt	Simulation	Expt	Simulation	Expt
a axis (Å)	13.14 ± 0.03	13.11	9.08 ± 0.01	8.99	10.00 ± 0.03	9.80
b axis (Å)	13.14 ± 0.03	13.11	15.14 ± 0.02	14.88	14.97 ± 0.05	14.84
c axis (Å)	26.19 ± 0.06	26.94	10.05 ± 0.01	9.80	18.02 ± 0.06	17.82
α angle (deg)	90 ± 0.0	90	90 ± 0.0	90	90 ± 0.0	90
β angle (deg)	90 ± 0.0	90	104.44 ± 0.0	103.52	106.57 ± 0.0	105.65
γ angle (deg)	120 ± 0.0	120	90 ± 0.0	90	90 ± 0.0	90
density (g/cc)	1.75 ± 0.01	1.713	1.76 ± 0.09	1.80	1.67 ± 0.02	1.733
Al-O (Å)	1.714 ± 0.071	1.732	1.733 ± 0.074	1.731	1.723 ± 0.08	1.729
P-O (Å)	1.530 ± 0.028	1.528	1.538 ± 0.042	1.535	1.532 ± 0.05	1.534
P=O (Å)	1.468 ± 0.014	1.486	1.470 ± 0.043	1.50	1.467 ± 0.03	1.495
O-Al-O (deg)	109.06 ± 8.14	109.99	109.04 ± 8.09	109.40	109.16 ± 7.75	109.48
O-P-O (deg)	106.04 ± 3.10	108.08	107.31 ± 3.95	107.89	106.47 ± 3.96	107.7
O-P=O (deg)	112.63 ± 3.71	111.86	111.51 ± 3.03	111.69	112.47 ± 3.92	111.2

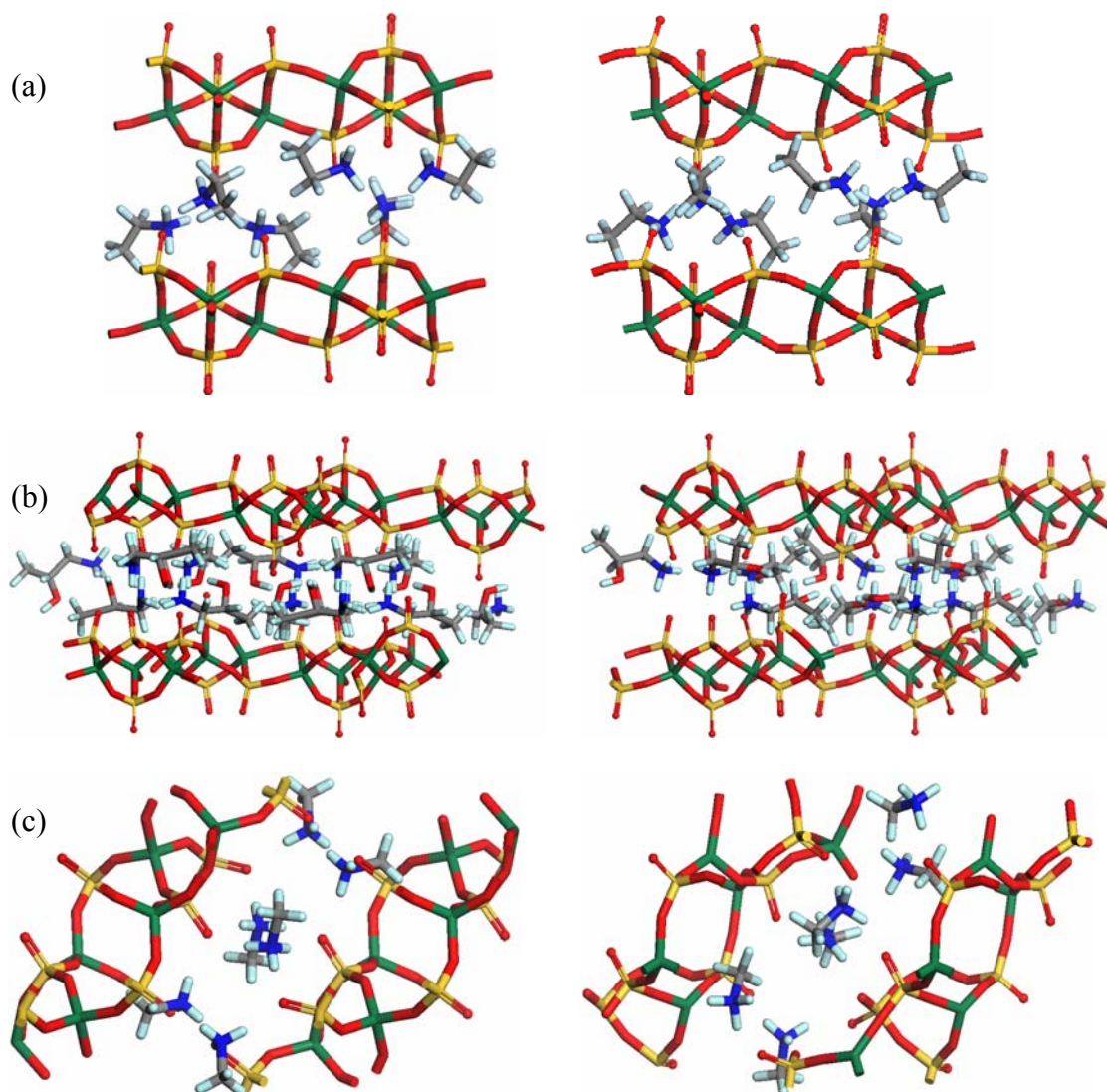


**Figure 3.1:** Comparison of experimental crystal structures (left) with predicted structures from molecular dynamics simulations (right). Snapshots show layered AlPOs with organic amine template molecules in the interlayer spacing. (a) 2D layered AlPO-triethylamine with  $4 \times 6 \times 8$  pore network, (b) 2D layered AlPO-isopropanolamine with  $4 \times 6 \times 12$  pore network, and (c) 1D chains of AlPO-trimethylamine with  $4 \times 8$  pore network. Al-green, P-gold, O-red, N-Blue, C-grey, H-Cyan.

### 3.3.2. Vibrational spectra

Comparison of the experimental IR spectra of AlPO-triethylamine and AlPO-isopropanolamine with the computed vibrational spectra of the structures forms a

stringent test of the force field as experimental spectroscopic data was not employed in the force field parameterization. Further, the AIPO pore network in layered AIPO-triethylamine (4-,6-,8-MR) and AIPO-isopropanolamine (4-,6-,12-MR) are different thus, providing an additional platform to test the transferability of the force field to different anionic AIPO structures with Al:P stoichiometry of 3:4. Figure 3.2 (a) and (b) show the results of comparison of the computed vibrational spectral positions with the deconvoluted experimental FTIR spectra for the two materials. Detailed evaluation of experimental and computed vibrational frequencies was obtained by directly comparing individual deconvoluted IR spectral bands with the normal-mode vibrational frequencies. Visual observation of the atomic vibrations *via* animation of normal modes allowed unique assignment of the vibrational modes to the frequency values as given in Tables 3.3 and 3.4, which are otherwise difficult to interpret from experiments due to the presence of a wide range of simultaneous atomic vibrations. The layered AIPO materials exhibit five prominent spectral bands: (i) frequencies between  $\sim 406 - 488 \text{ cm}^{-1}$  are due to stretching, bending vibrations in O-Al-O linkages and stretching in O-P-O linkages, (ii) frequencies in the range  $\sim 500 - 594 \text{ cm}^{-1}$  are due to O-P-O bending vibrations, (iii) frequencies between  $\sim 645 - 696 \text{ cm}^{-1}$  are due to Al-O-P bending vibrations, (iv) frequencies between  $\sim 707 - 742 \text{ cm}^{-1}$  are due to Al-O-P symmetric stretching and bending vibrations, and (v) frequencies between  $\sim 755 - 815 \text{ cm}^{-1}$  are due to asymmetric stretching and bending vibrations in Al-O-P linkages. As seen in Figure 3.2, the AIPO framework modes are constant between the two materials. The absorption peaks between  $1350-1550 \text{ cm}^{-1}$  are due to the stretching and bending vibration of C-C bonds as given in Tables 3.3 and 3.4. The small differences in vibrational peaks are due to the C-C

vibrations from  $\text{-CHOH}$  group in the isopropanolamine template molecule. The computed vibrational peak positions of hydrogen bonded alkyl ammonium N-H bonds agree well between the two structures as well as with the experimental frequency values<sup>176</sup> suggesting that the present force field works well in conjunction with the PCFF force field for the organic molecules to capture the hydrogen bonding phenomenon between the AIPO structure and the organic template molecule. The low intensity absorption peaks between  $2000\text{-}2400\text{ cm}^{-1}$  observed in the FTIR spectra of the two AIPO materials were not observed in the computed vibration spectra. The origin of these peaks is currently not well understood. Detailed spectroscopic studies including Raman spectroscopy measurements are underway to understand the occurrence of these absorption peaks. On the other hand, the absorption peaks between  $2400\text{-}2750\text{ cm}^{-1}$  in the FTIR spectra that are absent in the computed spectra could be related to the overtone vibrational modes of AIPO that cannot be captured by a normal-mode analysis. Overall, the predicted vibrational spectra for organic template molecules approximates the IR spectra suggesting that the incorporation of the metal-oxygen force field parameters in PCFF did not compromise the performance of PCFF in describing the organic molecules. Deviations of  $\sim 10\text{ cm}^{-1}$  are observed in the spectral peak positions between the computed power spectra and the experimental IR spectra. This is a typical level of deviation in force fields developed for inorganic oxide materials<sup>171,173,177</sup>. The results shown in Figure 3.2, and Tables 3.3 and 3.4 clearly suggest that the present force field well reproduces the experimental vibrational spectra irrespective of the difference in pore sizes as well as the organic template molecules in the interlayer spacing, and validate the applicability of the force field for the present investigation.

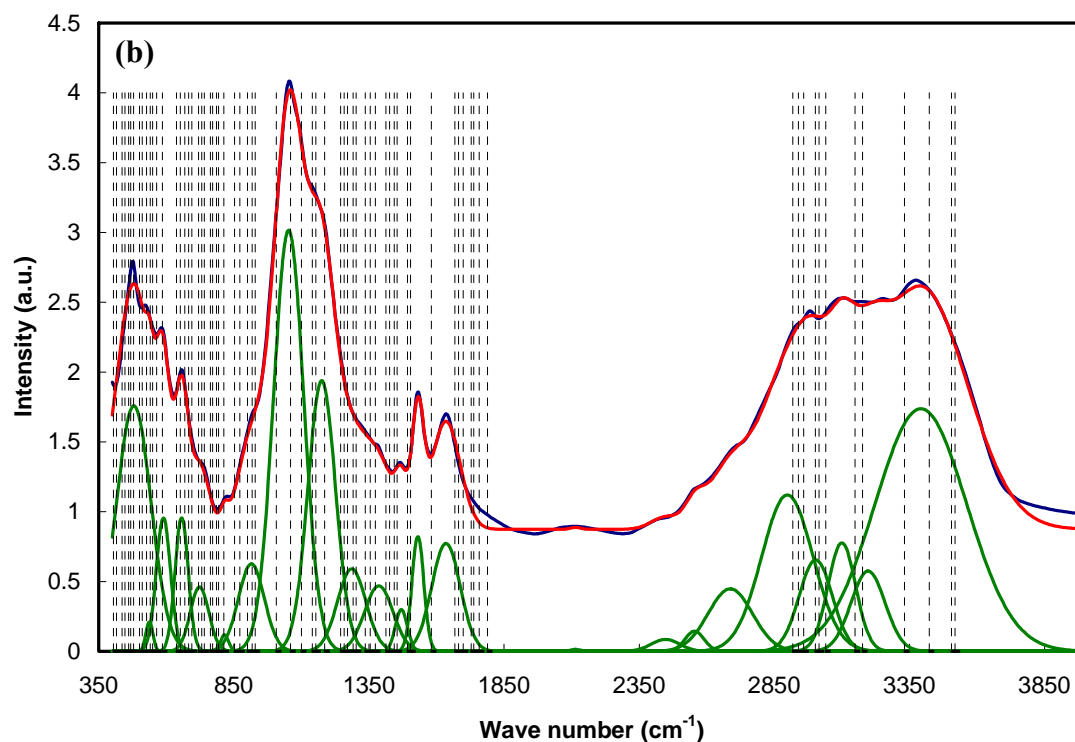
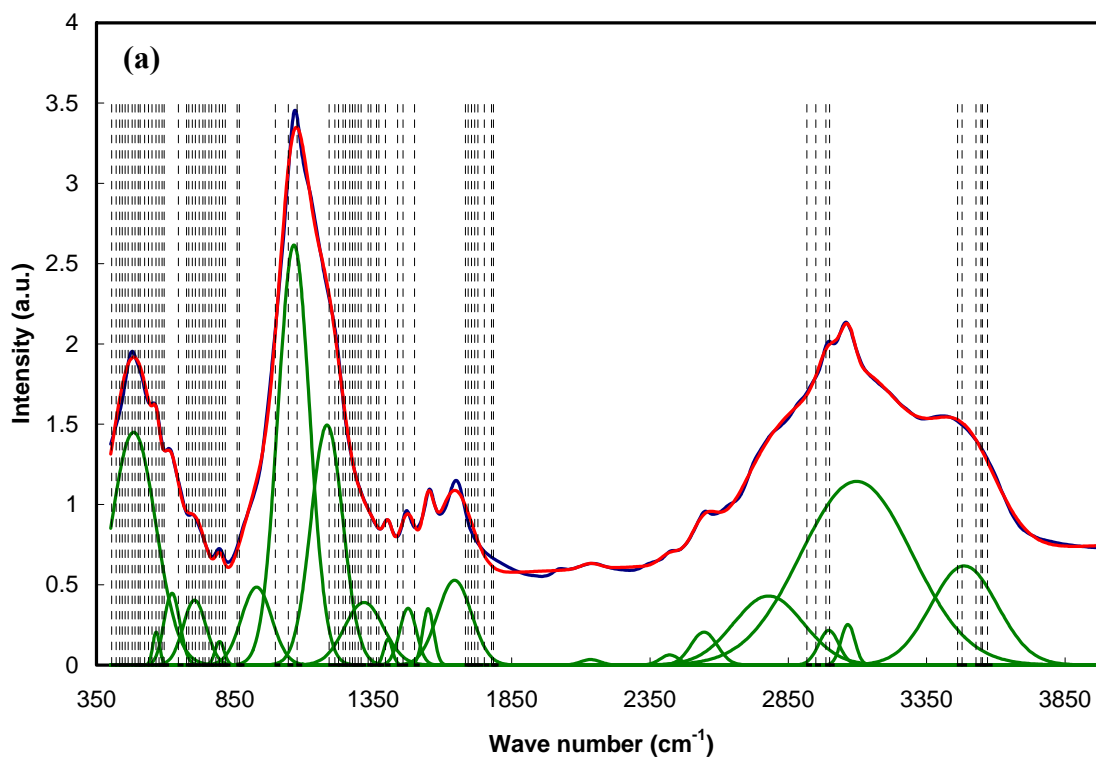


**Figure 3.2:** Comparison between computed vibrational spectral peak positions (dotted lines) and experimental IR spectral peak (blue solid line) for (a) 2D layered AlPO-triethylamine, and (b) 2D layered AlPO-isopropanolamine. Solid green lines denote Gaussian curves and solid red line denotes the Gaussian fit of the FTIR spectra.

**Table 3.3:** Comparison of experimental IR peak positions and normal mode vibrational frequencies for layered AlPO-triethylamine.

<b>FTIR peak positions (cm<sup>-1</sup>)</b>	<b>Normal-Mode Analysis (cm<sup>-1</sup>)</b>	<b>Vibrational Peak Assignments</b>
484 ± 80 566 ± 12	405, 421, 433, 443, 453, 464, 479, 489 500, 508, 524, 538, 550, 565, 576, 586, 594	AlPO framework vibrational modes
623 ± 28	646, 675, 683, 696	AlPO framework vibrational modes + weak twisting vibration of H-N-H in NH <sub>3</sub> <sup>+</sup>
705 ± 41	708, 721, 734, 743, 756, 766	AlPO framework vibrational modes + weak rocking vibrations of CH <sub>3</sub> and CH <sub>2</sub>
795 ± 16	781, 794, 805, 815	C-C stretching vibrations
929 ± 55 1063 ± 57	858, 866 996, 1042, 1075	C-C and C-N stretching vibrations
1183 ± 57 1317 ± 70	1190, 1212, 1224, 1241, 1249 1265, 1275, 1284 1296, 1306, 1332, 1341, 1361, 1370	C-C +C-N stretching coupled with weak rocking and twisting vibration of C-H in CH <sub>3</sub> , CH <sub>2</sub> and N-H in NH <sub>3</sub> <sup>+</sup>
1404 ± 15	1395, 1438	Symmetric bending of CH <sub>3</sub> and CH <sub>2</sub>

**Table 3.3:** Continued

1476 ± 30 1549 ± 20	1458, 1499	Wagging vibration of CH <sub>3</sub> and symmetric stretching of CH <sub>2</sub> at 1458 cm <sup>-1</sup> and wagging vibration of CH <sub>2</sub> at 1499 cm <sup>-1</sup>
1644 ± 61	1683, 1693 1705, 1716, 1728, 1752, 1777, 1784	Symmetric bending of N-H in NH <sub>3</sub> <sup>+</sup> coupled with wagging vibrations of N-H in NH <sub>3</sub> <sup>+</sup> (modes are weaker at higher frequencies)
2135 ± 35 2421 ± 34 2545 ± 47		Spectral bands associated with overtone vibrational modes of AlPO
2779 ± 126	2917, 2949	Symmetric C-H vibrations in CH <sub>3</sub> and CH <sub>2</sub>
2996 ± 36 3065 ± 25 3097 ± 201	2986, 2999	Asymmetric C-H vibrations in CH <sub>3</sub> and CH <sub>2</sub>
3485 ± 120	3462, 3477, 3528, 3546, 3551, 3570	N-H stretching vibrations in NH <sub>3</sub> <sup>+</sup> (symmetric 3462,3477 cm <sup>-1</sup> and asymmetric 3528-3570 cm <sup>-1</sup> )

**Table 3.4:** Comparison of experimental IR peak positions and normal mode vibrational frequencies for layered AlPO-isopropanolamine.

<b>FTIR peak positions (cm<sup>-1</sup>)</b>	<b>Normal-Mode Analysis (cm<sup>-1</sup>)</b>	<b>Vibrational Peak Assignments</b>
480 ± 64 538 ± 13 590 ± 26	405, 416, 437, 447, 460, 469, 479, 501, 512, 527, 541, 550 565, 586	AlPO framework vibrational modes
657 ± 24 723 ± 34	638, 652, 669, 683 695, 719, 731, 741	AlPO framework vibrational modes + weak twisting vibration of H-N-H in NH <sub>3</sub> <sup>+</sup> + rocking mode of O-H
816 ± 15	764, 772, 786, 794, 813	C-H rocking mode in CH <sub>3</sub> and CH <sub>2</sub> groups
915 ± 48	853, 872, 901, 918, 929	C-C stretching
1053 ± 56 1176 ± 51	1007, 1060, 1100 1141, 1154, 1186	C-C + C-N stretching
1286 ± 52 1387 ± 53	1245, 1258, 1271, 1292, 1303, 1337 1354, 1374, 1413	C-C+C-N stretching vibrations coupled with weak rocking vibration of CH <sub>3</sub> , CHOH, CH <sub>2</sub> , NH <sub>3</sub> <sup>+</sup>
1470 ± 22 1531 ± 22	1427, 1443, 1454, 1493 1504, 1581	C-H bending mode in CH <sub>3</sub> , CH <sub>2</sub> and CHOH
1635 ± 52	1668, 1682, 1699, 1728, 1737, 1758, 1788	N-H bending vibration mode in NH <sub>3</sub> <sup>+</sup> (symmetric bending at 1581-1699 cm <sup>-1</sup> ; wagging motion at 1728-1788 cm <sup>-1</sup> )

**Table 3.4:** Continued

2115 ± 19 2447 ± 52 2555 ± 35 2687 ± 82		Spectral bands associated with overtone vibrational modes of AlPO
2898 ± 95 3003 ± 61 3099 ± 51	2917, 2938, 2958, 3002, 3015, 3040	C-H stretching vibration mode (symmetric stretch in CH <sub>3</sub> at 2917 cm <sup>-1</sup> , CHOH at 2938 cm <sup>-1</sup> , CH <sub>2</sub> at 2958 cm <sup>-1</sup> ; asymmetric stretch in CH <sub>3</sub> at 3002 mc <sup>-1</sup> , CH <sub>2</sub> at 3015 cm <sup>-1</sup> , CH <sub>3</sub> and CH <sub>2</sub> at 3040 cm <sup>-1</sup> )
3197 ± 63	3148, 3176	O-H bond stretching vibration mode
3392 ± 170	3331, 3423, 3505, 3518	N-H stretching vibrations in NH <sub>3</sub> <sup>+</sup> (symmetric 3331cm <sup>-1</sup> and asymmetric 3423-3518 cm <sup>-1</sup> )

### 3.3.3. X-ray Diffraction

X-ray diffraction patterns for all the 7 layered AlPO materials were calculated by considering the final equilibrated structures from MD simulations. For each structure, the diffraction patterns from 5 independent simulations were averaged and compared with the XRD pattern calculated based on the experimental crystal structure data, as shown in Figure 3.3 (a)-(g). The XRD patterns for simulated layered AlPO structures are in good

agreement with that calculated based on the crystal structure data. The diffraction peak positions correspond very well between the observed and simulated structures, while the intensities exhibit slight deviations due to relaxation of the crystal structures during geometry optimization and equilibration MD simulations. Overall, the successful prediction of layered AIPO structures well-validates the applicability of the force field to layered AIPO models with Al/P stoichiometry ratio of 3:4.

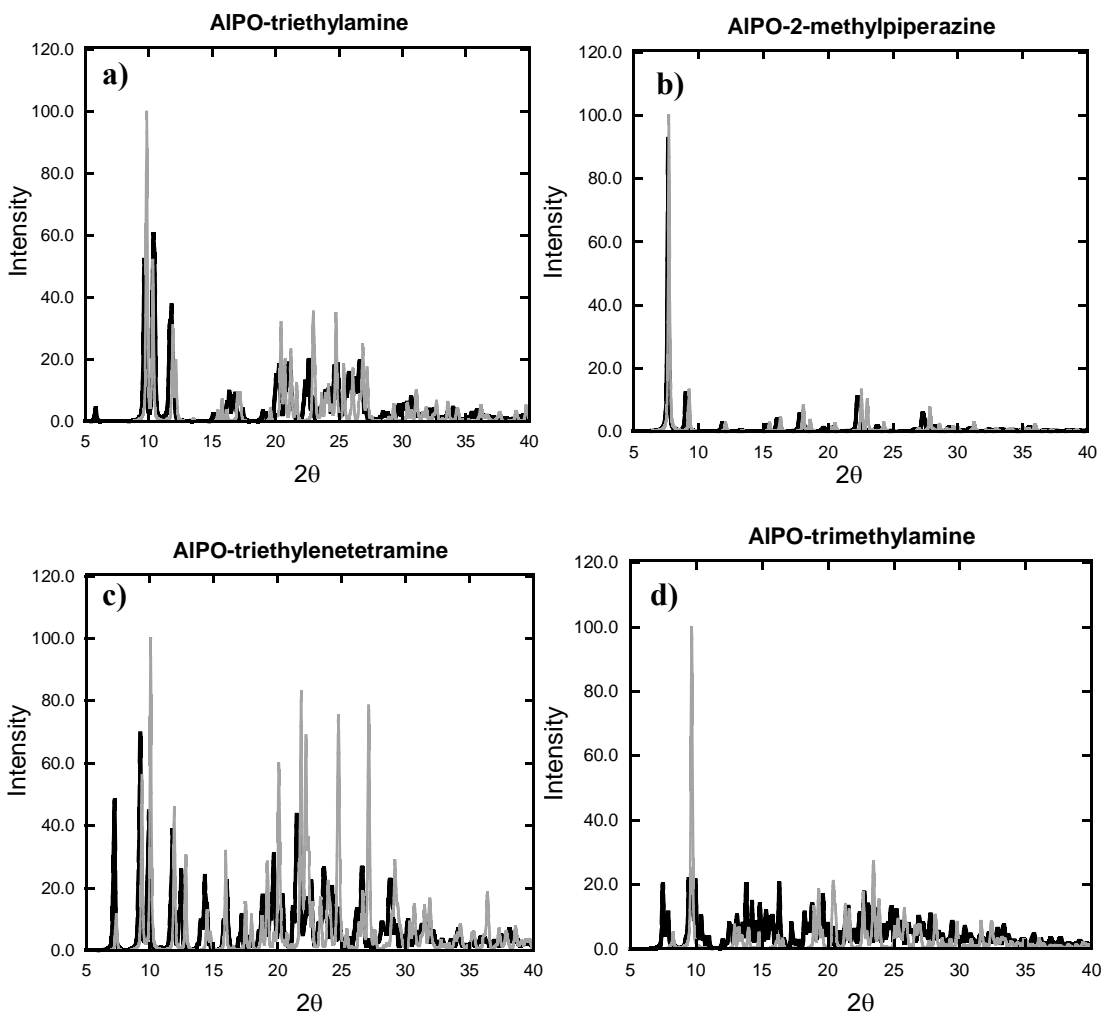


**Figure 3.3:** Comparison between computed X-ray diffraction patterns of 2D and 1D layered AIPOs crystal structures (black) and simulated structures (grey).

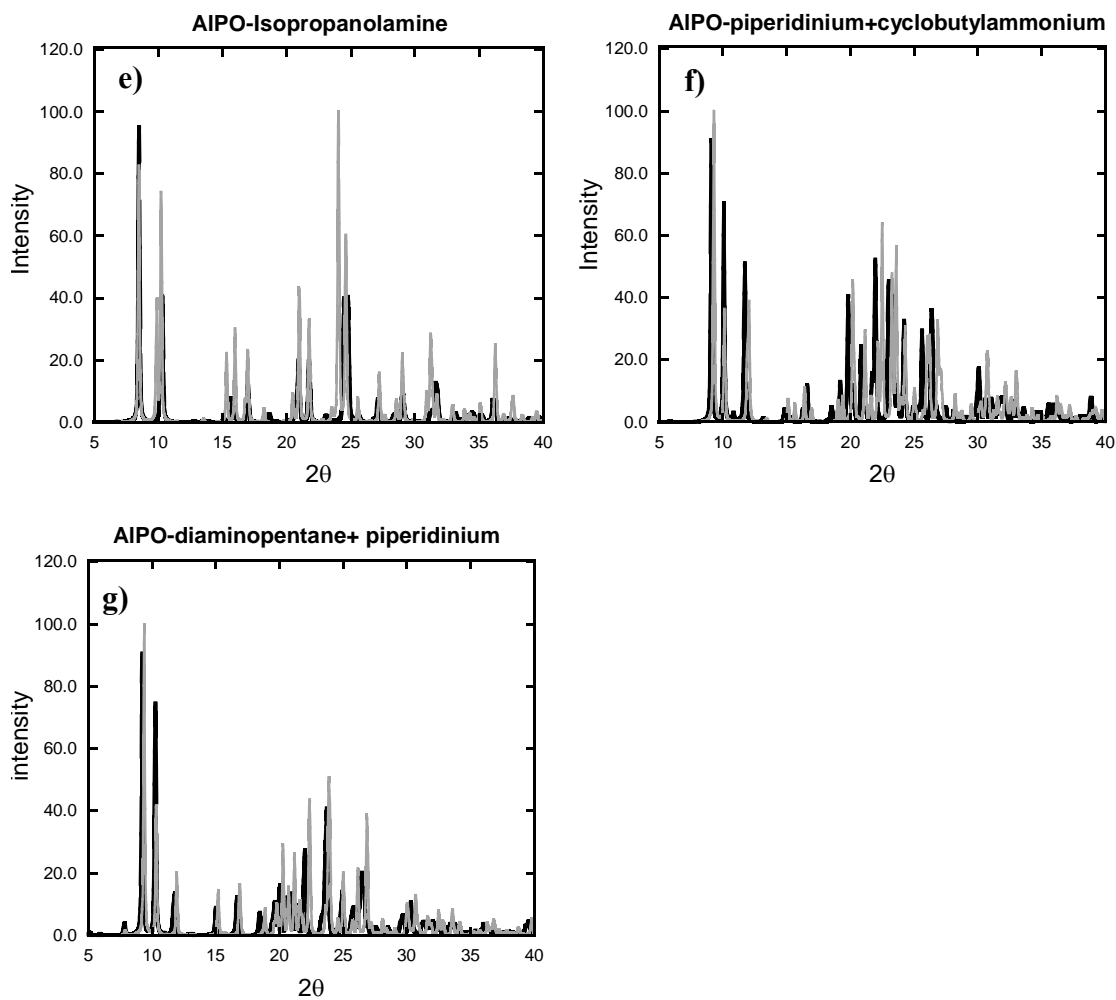


**Figure 3.3:** Continued

### **3.4. Conclusions**

In this study, the first force field for layered aluminophosphate materials is presented. The force field is based on a 9-6 Lennard Jones potential combined with an electrostatic potential, in accordance with the nonbond functional form of the PCFF, to describe the metal-oxygen atom interactions within the layered AIPO network. The force field parameters derived based on the crystal structures of 2D layered AIPO-triethylamine, AIPO-2-methylpiperazine, and AIPO-triethylenetetramine successfully

describe the bulk structures of a broad range of 2D and 1D layered AIPOs. In addition, the spectroscopic as well as the molecular structure of the layered AIPOs were also well reproduced demonstrating a good transferability of the force field to a variety of layered AIPO structures with varying AIPO network, pore sizes and template molecules. The current force field is specialized to layered AIPO materials with a 0.75 Al/P stoichiometry. The force field parameters are robust and can potentially be used to simulate dynamical properties such as diffusion of small molecules, or the interfacial structures of hybrid materials containing layered AIPOs.

# CHAPTER 4

## GAS TRANSPORT IN STIFF CHAIN POLYMER/NANOPOROUS INORGANIC LAYERED NANOCOMPOSITE MATERIALS

### 4.1. Introduction

Diffusion of penetrants in polymers involves random jumps of penetrant molecules between cavities *via* a connecting channel that are transiently created by polymer segmental mobility. In rubbery polymer, the frequency of these jump events was of the order of  $\text{ps}^{-1}$  due to relatively high mobility of polymeric chains resulting in estimation of diffusion coefficient within MD simulation timescales of ps to few ( $\sim 3$ ) ns<sup>107,121,122,125</sup>. However, for glassy polymers the segmental motion of the polymeric chains is restricted causing a decrease in the frequency of appearance of transient diffusion channels between the cavities. Consequently, the penetrant jump events were observed at ns timescales and involved jump between cavities with large activation energy barrier<sup>178-180</sup>. While MD simulations have proven to be very useful for providing detailed molecular understanding of the system dynamics, the simulations are limited to rather short timescale of up to few ( $\sim 10$ ) nanoseconds. Investigation of transport process in materials containing stiff chain polymers requires longer simulation timescale of several nanoseconds to allow the diffusion of penetrant molecules in the polymer matrix to attain random walk regime. In such cases, Monte Carlo Transition State Approach (MC-TSA) of Gusev and Suter<sup>181</sup> has been shown to be very successful in determining the diffusivities and solubilities of the penetrants in the polymeric membrane materials. This method captures only the penetrant jump events between cavities while excluding the

anomalous motion of the penetrant within the cavities to decrease the computational time of the simulations. Here, we will employ this method for the first time to calculate the diffusivities of small gas molecules in polymer/layered inorganic nanocomposite materials. We present here our preliminary results on ongoing efforts in developing MC-TSA method for the nanocomposite materials.

#### **4.2. Transition State Approach Methodology**

The main assumptions involved in the TSA method are that the diffusion of small molecules occurs via a series of activated hops between individual “holes” of the polymer matrix, and penetrant dynamics are dependant on the elastic motion of the polymer atoms but are independent of structural relaxation of the polymeric matrix. These assumptions limit the methodology to calculation of diffusivity of small penetrant molecules with sizes up to methane. The vibrations of the polymer atoms about their equilibrium positions are described by a normalized probability density function  $W(\{\Delta\})$  that follows Debye’s approach of isotropic elastic motion with the deviations  $\Delta_\alpha = X_\alpha - \langle X_\alpha \rangle$  of the host atoms.

$$w(\{\Delta\}) \propto \exp\left(-\sum_{\alpha=1}^N \frac{\Delta_\alpha^2}{2\langle \Delta_\alpha^2 \rangle}\right) \quad (4.1)$$

As a result, the probability of finding a penetrant at a point  $r$  in the polymer matrix is given by a modified equilibrium Boltzmann probability density distribution,  $\rho(r)$  (Eq.4.2).

$$\rho(r) = \int d\{\Delta\} W(\{\Delta\}) e^{-U(r,\{X\})/kT} \quad (4.2)$$

Here  $U(r,\{X\})$  is the potential energy of interaction between the penetrant and polymer atoms  $X_\alpha$  ( $\alpha \in \{1,\dots,N\}$ ). This distribution function is evaluated for all the penetrant molecules placed at periodic intervals in the polymer matrix, obtained by placing a grid on the simulation cell, to compute the probability of finding the penetrants at each of its allocated positions. The next step involves identifying the *sites* occupied by the penetrants by locating the local maxima of  $\rho(r)$  (or the local minima of potential energy). This can be achieved by starting a steepest descent algorithm at each grid point that terminates at the local maxima of  $\rho(r)$ , allowing unique grid point assignments to the set of sites. Then a configurational partition function ( $Z_j$ ) for a site,  $j$  with volume  $V_j$  and assigned with grid points  $\alpha,\dots,\delta$  can be evaluated as <sup>182</sup>:

$$Z_j = \int_{V_j} \rho(r) dV = \rho(r, \alpha) + \dots + \rho(r, \delta) \quad (4.3)$$

Following this, the configurational partition function ( $Z_{ij}$ ) for the crest surfaces ( $\Omega_{ij}$ ) between two adjacent grid points allocated to sites  $i$  and  $j$  can be evaluated taking into account that a grid point allocated to site  $i$  has at least one of its six nearest neighbors belonging to site  $j$  (Eq.4.4).

$$Z_{ij} = \int_{\Omega_{ij}} \rho(r) dS = f_\alpha \rho(r, \alpha) + \dots + f_\delta \rho(r, \delta) \quad (4.4)$$

Here  $f$  denotes weighting factor to account for the shape of the crest surface. Thus, for a grid point  $\alpha$  belonging to site  $i$ ,  $f = 1, 2^{1/2}, 1.41, 2.0, 0$  when one, two, three, four or five nearest neighbors of grid point  $\alpha$  belong to site  $j$ . Finally, a simple MC algorithm is employed to study the dynamics of the penetrant within the network of sites in the polymeric matrix. Briefly, the procedure is described as follows: (i) a residence site is randomly selected initially to start the penetrant's random walk, (ii) the target site for the penetrant's first jump is chosen according to the transition probability  $w_{ij}$  from site  $i$  to  $j$  as given by Eq.4.5. The jump is associated with a rate constant of  $R_{ij}$  (Eq.4.6) and a time increment  $\Delta t = \tau_i$  (Eq.4.7).

$$w_{ij} = \tau_i R_{ij} \text{ with } \sum_j w_{ij} = 1 \quad (4.5)$$

$$R_{ij} = \sqrt{\frac{kT}{8\pi m}} \frac{Z_{ij}}{Z_i} \quad (4.6)$$

$$\tau_i = 1 / \sum_j R_{ij} \quad (4.7)$$

Here  $m$  is the penetrant's mass. This step is repeated until a stochastic trajectory of the penetrant with predetermined number of jumps is obtained.

An important parameter of the TSA method is the '*smearing factor*' i.e.  $\langle \Delta^2 \rangle$  that needs to be determined to start the algorithm. One possible method to calculate  $\langle \Delta^2 \rangle$  is the self-consistent field procedure that determines a value for  $\langle \Delta^2 \rangle$  by employing mean squared displacements ( $s(t)$ ) of the polymer atoms obtained from a short (10-20ps) MD run<sup>107</sup>. The method comprises of a non-trivial iterative procedure that initially involves

approximating a value for  $\langle \Delta^2 \rangle$ , followed by determination of the residence times  $\tau_i$  via Eq.4.7. Then  $\tau_{\max}$  is calculated by mapping the distribution of mean residence times as a function of  $\tau$  to identify the distinct maximum (i.e.  $\tau_{\max}$ ). An assumption involved in the method is that the critical averaging time,  $t_{\text{crit}}$  at which  $\langle \Delta^2 \rangle = s(t_{\text{crit}})$  is equal to the most frequent residence times  $\tau_{\max}$  of the penetrant in the polymeric matrix. Hence, using this criterion a new value of  $\langle \Delta^2 \rangle$  is obtained. This procedure is repeated until the desired convergence criterion is fulfilled to correctly determine the value of  $\langle \Delta^2 \rangle$ .

Application of the TSA algorithm to simulate penetrant diffusion in nanocomposite materials does not challenge any assumptions involved in the method. However, one complexity involved in extending this method to nanocomposite materials is to correctly calculate a combined smearing factor for the polymeric and inorganic components.

### **4.3. Computational Methodology**

Equilibrated membrane (pure polymer or nanocomposite) models were constructed using Materials Studio 3.2 MD package (Accelrys, Inc) following the procedure outlined in Section 2.2 of Chapter 2. Then, an in-house Fortran code that was initially developed by Dr. Sankar Nair and Dr. Yeny Hudiono was modified accordingly to calculate the penetrant probability density distribution in the membrane model. As a first step, we develop the algorithm to calculate the diffusion of monoatomic gas

molecules (e.g. He) in a rigid matrix (e.g. PDMS). In such a case Eq. 4.2 reduces to a simple form as given by Eq. 4.8.

$$\rho(r) = \int e^{-U(r,\{X\})/kT} \quad (4.8)$$

The probability density distribution function was calculated by layering a 3D-grid with a fine grid resolution of 1/100<sup>th</sup> of lattice dimension over the simulation cell. Then a penetrant molecule was inserted at each grid node and the interaction energy between the penetrant atoms and the neighboring polymer atoms was calculated using the non-bonded 9-6 van der Waals potential energy equation with PCFF force field parameters. The calculation procedure was validated by visual comparison of the 3D probability density distribution map with the atomistic membrane models (see Section 4.4.1). Following this, we employed a steepest-descent method to calculate the local maxima of  $\rho(r)$ . The steepest-descent algorithm was started from each grid point, which terminated at local maxima of  $\rho(r)$  allowing unique assignment of the initial grid point as well as the local maxima grid point to a penetrant resident site. A geometry criterion such as the size of resident site, which is in turn estimated from the size of penetrant molecule as well as visual observation of sizes of ‘islands’ formed by local maxima of  $\rho(r)$  grid points, was employed to define all the resident sites (see Section 4.4.2). Calculation of crest surfaces and the configurational partition functions (given by Eq.s 4.3 and 4.4) are on-going to develop the MC algorithm for calculating the penetrant diffusivities. All the calculations described above were performed using Fortran programming language, while all the visualizations were performed using Matlab.

## **4.4. Results and Discussion**

### **4.4.1. Penetrant Probability Density Distribution**

The validation study for the penetrant probability density distribution calculation was performed for two cases; (i) diffusion of He atoms in zeolite MFI, and (ii) diffusion of He in pure polymer PDMS. Figures 4.1 and 4.2 show a comparison of the penetrant probability density distribution profiles with the atomistic models of MFI and PDMS, respectively. The gradient color scheme from dark blue to dark red in the distribution profiles indicates regions of low-high probabilities, respectively, of finding the penetrant molecules in the host matrix structures. Aluminosilicate zeolite MFI contains a two-dimensional pore structure with intersecting straight and sinusoidal channels. The distribution profile shown in Figure 4.1 (a)-(b) clearly show the two channels along with the channels intersections (dark red regions), indicative of the penetrant resident sites<sup>183</sup>, in the distribution profile. Likewise, the resident sites in pure polymer PDMS shown in Figure 4.2, correspond with high penetrant probability density regions in the distribution profile. Overall, these results well-validate our penetrant probability density distribution calculations.

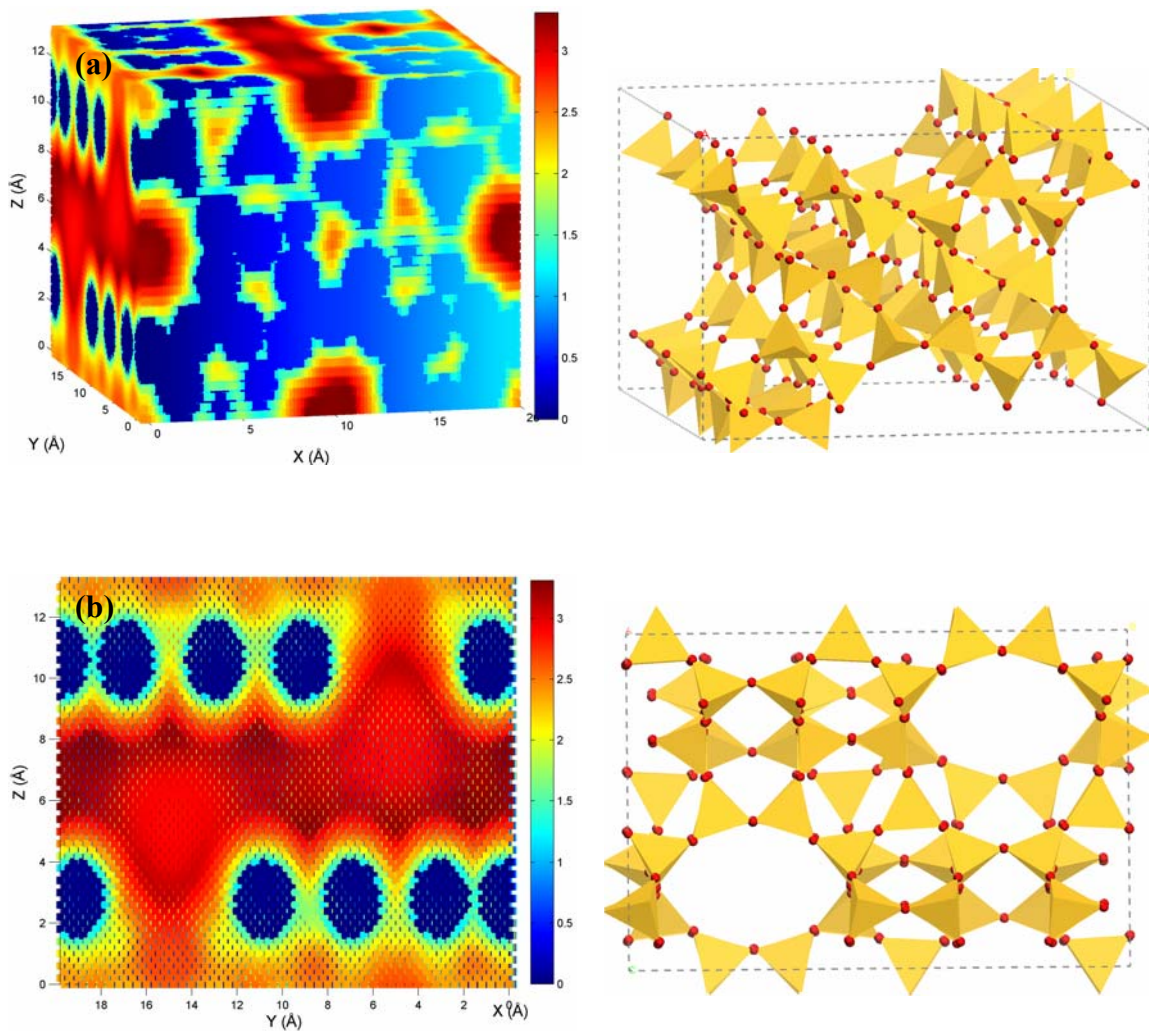


**Figure 4.1:** Penetrant probability density distribution map of He in MFI (left) indicating straight (a), and sinusoidal channels of MFI pore structure. Gradient in color from dark blue to dark red indicates transition from low-high probability of finding He atoms in MFI structure. MFI snapshots indicating the pore channels are given on the right. Si-Gold, O-Red.

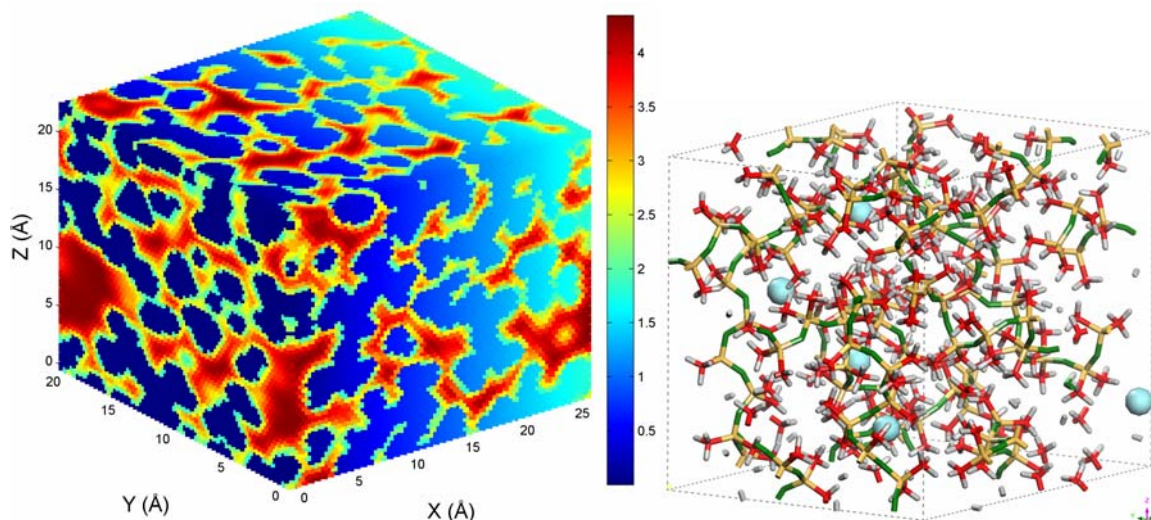


**Figure 4.2:** Penetrant probability density distribution map of He in PDMS (left). The location of high penetrant probability density regions closely approximate with the resident sites in the snapshot of the He atoms in PDMS (right). Si-Gold, O-Green, C-Red, H-Grey, He-Cyan.

#### 4.4.2. Resident Sites

Next, the local maxima of  $\rho(r)$  (or local minima of interaction energy) were calculated using steepest-descent method. Figure 4.3 indicates the regions of maximum penetrant probability. Visual observation of the local maxima regions suggests that the size of resident sites is  $\sim 5$  Å. We utilize this value as a distance cut-off parameter to assign the local maxima grid points to different resident sites. We then eliminate resident sites with sizes less than 2 Å (which is less than the 2.6 Å size of He atom) in the minimum dimension by visual examination to obtain sites that are large enough to accommodate the penetrant atom. Figure 4.4 shows the resident sites obtained by the described procedure.

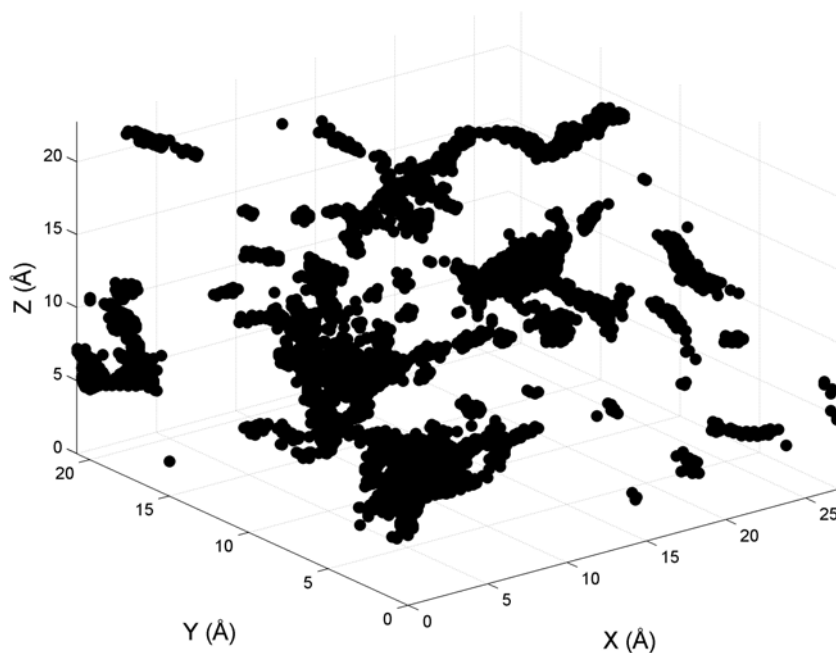


**Figure 4.3:** Local maxima of penetrant (He) probability density values in PDMS obtained using steepest-descent method.

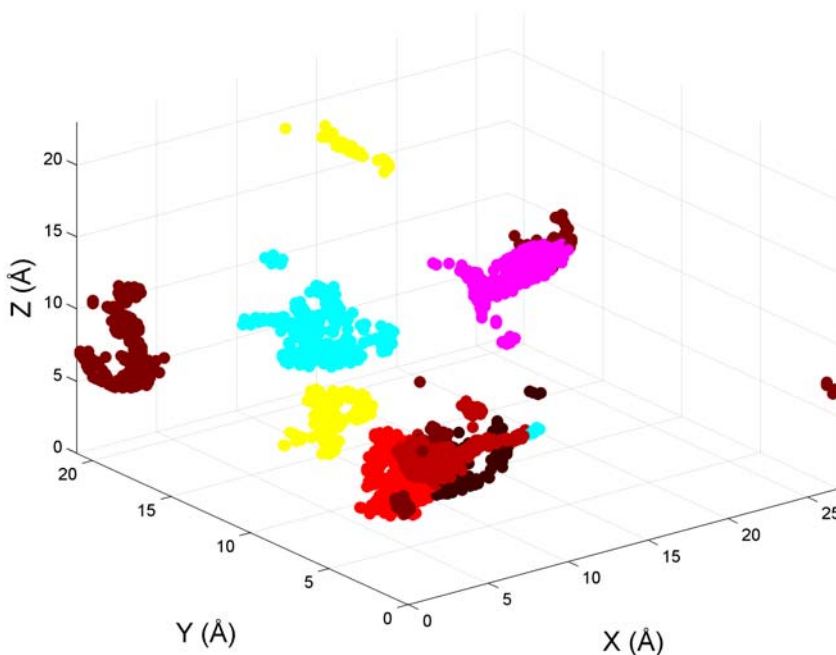


**Figure 4.4:** He resident sites in PDMS matrix. The sites are expressed in different colors for clarity.

### 4.4.3. Future Work

The next step involves calculating the crest surfaces between the adjacent sites. Crest surfaces are regions of high energy or low probability density that act as transition state between two resident sites. Consequently, the penetrant ‘jump’ probability is inversely proportional to these transition regions as given by Eqs. 4.5 and 4.6. The grid points belonging to the crest surface between two resident sites are obtained by matching the local maxima grid points of a resident site with the respective initial grid points of the steepest-descent paths. The configurational partition functions can then be calculated to perform the MC simulation for obtaining the penetrant diffusion trajectories using the procedure described in Section 4.2. The resulting diffusivity values can be validated with MD simulations results obtained in Chapter 2 for both PDMS and PDMS/AMH-3 models. Further studies on extending this procedure to include the diffusion of polyatomic penetrant molecules in membrane matrix exhibiting elastic motion of host atoms will establish a framework for providing qualitative/quantitative predictions of transport properties of gas molecules in polymer/porous inorganic layered nanocomposite materials.

# CHAPTER 5

## DIMENSION CONTROL OF SINGLE-WALLED METAL OXIDE NANOTUBES

### 5.1. Introduction

Control over nanotube diameter is of significance in manipulating their properties, which depend on their dimensions in addition to structure and composition. This aspect has remained a challenge in both carbon and inorganic nanotubes, since there is no obvious aspect of the formation mechanism that allows facile control over nanotube curvature. Inorganic metal oxide nanotubes<sup>184</sup> are a more recently emerging class of nanomaterials that can be synthesized with tunable compositions *via* low-temperature liquid-phase chemistry. Such materials are attractive because of the vast range of technologically relevant properties afforded by metal oxides, and because of the possibilities for more precise control over their dimensions, compositions, and resulting properties. Here, we investigate a class of metal-oxide aluminosilicogermanate ('AlSiGeOH') nanotubes<sup>86,185,186</sup> that are synthetic analogues of the naturally occurring aluminosilicate nanotube mineral, imogolite. The general empirical formula of the unit cell is  $(\text{OH})_3\text{Al}_2\text{O}_3\text{Si}_x\text{Ge}_{1-x}\text{OH}$ ,  $0 \leq x \leq 1$ . The energetics of the aluminosilicate end-member (i.e.,  $x = 1$ ) nanotube has been examined in a previous computational study. An internal energy minimum was observed as a function of increasing nanotube diameter<sup>187</sup> - a phenomenon that is not observed in the case of carbon nanotubes or their inorganic analogues wherein the internal energy declines monotonically with increasing diameter<sup>19,100</sup>. It was suggested early<sup>79</sup> that the curvature of the nanotube could be due to the

differing energies of the Al-O and Si-O bonds that can quite possibly be responsible for the experimentally well-known monodispersity in diameter of the synthetic aluminosilicate nanotube.

In this study, we re-examine the energy minimum of the AlSiGeOH nanotubes to determine whether there is a well-defined relationship between generalized AlSiGeOH nanotube diameter and internal energy, and to ascertain whether this relationship correlates with the composition of the nanotubes. We investigate the nanotube energetics *via* molecular dynamics (MD) simulations. We present an approximate quantitative model to describe the physics governing control over the nanotube diameter as well as to explain the correlation between the nanotube diameter, energy, and composition.

## **5.2. Computational Methodology**

### **5.2.1. Force field Parameterization**

We employed the functional form of the recently developed CLAYFF force field<sup>171</sup>, which was well validated for a range of aluminosilicate layered minerals, to describe the interactions between the atoms of the nanotube. The force field is based on the Born ionic model, with fractional charges assigned to each atom and Lennard-Jones (LJ) (12-6) potentials for Al-O, Si-O, Ge-O and O-O interactions. The O-H bonds are described by a harmonic bond-stretching term.

$$E = \frac{e^2}{4\pi\epsilon_o} \sum_{i \neq j} \frac{q_i q_j}{r_{ij}} + \sum_{i \neq j} \epsilon_{ij} \left[ \left( \frac{R_{o,ij}}{r_{ij}} \right)^{12} - 2 \left( \frac{R_{o,ij}}{r_{ij}} \right)^6 \right] + k_{ij} (r_{ij} - r_o)^2 \quad (5.1)$$

Where  $R_{o,ij} = \frac{1}{2}(R_{o,i} + R_{o,j})$  and  $\epsilon_{ij} = \sqrt{\epsilon_i \epsilon_j}$

The force field parameters for Al, Si, O and H were chosen to be the same as the reported CLAYFF parameters. We optimized LJ parameters (i.e.  $\epsilon$  and  $\sigma$ ) for Ge using the General Utility Lattice Program, GULP<sup>160</sup>, which employs nonlinear least squares and energy minimization to fit the force field predictions to the experimental crystal structures. We used the crystal structures of two known aluminogermanate materials with tetrahedrally coordinated Ge, namely the ‘C-phase’ of Na{AlGeO<sub>4</sub>} and the ‘D-phase’ of K{AlGeO<sub>4</sub>},<sup>188</sup> in addition to the structure of  $\alpha$ -GeO<sub>2</sub><sup>189</sup> (which is analogous to  $\alpha$ -quartz). Initially, the C-phase of Na{AlGeO<sub>4</sub>} (monoclinic space group P2<sub>1</sub>/n and lattice parameters  $a = 8.783 \text{ \AA}$ ,  $b = 15.432 \text{ \AA}$ ,  $c = 8.252 \text{ \AA}$ ,  $\alpha = \beta = 90^\circ$ ,  $\gamma = 90.09^\circ$ ) was used to derive the tetrahedral Ge-O LJ interaction parameters. The LJ values for the oxygen atoms were kept the same as the CLAYFF values in accordance with the procedures used for development of that force field, whereas the tetrahedral Al LJ parameters were optimized to reproduce the observed Al-O bond distances. The tetrahedral Al parameters given in CLAYFF were developed for Al-O-Si linkages and could not reproduce the ideal Al-O bond lengths in Al-O-Ge linkages. The partial charges for Ge and Al were assigned to be the same as the tetrahedral Si and octahedral Al atoms respectively, consistent with the parameter assignment procedure followed in CLAYFF to handle atoms in the same group of the periodic table. The initial Ge-O and Al-O interaction parameters were

further refined by including the crystal structures of  $\alpha$ - GeO<sub>2</sub> (hexagonal space group P3<sub>1</sub>21 and lattice parameters  $a = 4.9845 \text{ \AA}$ ,  $b = 4.9845 \text{ \AA}$ ,  $c = 5.6477 \text{ \AA}$ ,  $\alpha = \beta = 90^\circ$ ,  $\gamma = 120^\circ$ ) and the D-phase of K{AlGeO<sub>4</sub>} (hexagonal space group P6<sub>3</sub> and lattice parameters  $a = b = 18.429 \text{ \AA}$ ,  $c = 8.599 \text{ \AA}$ ,  $\alpha = \beta = 90^\circ$ ,  $\gamma = 120^\circ$ ) in the fitting procedure. Table 5.1 shows the final list of parameters.

**Table 5.1:** Force field parameters used in MD simulations for calculating the energetics of single-walled AlSiGeOH nanotubes. Parameters for Al, Si, O and H are the same as the original CLAYFF<sup>171</sup>, force field with additional parameters for Ge developed in this work using the same procedures as the CLAYFF.

<b>Nonbond parameters for the force field</b>			
<b>Species</b>	<b>Charge (e)</b>	<b><i>E</i> (kcal/mol)</b>	<b><i>R<sub>o</sub></i> (Å)</b>
Hydroxyl H	0.425	-	-
Hydroxyl O	-0.95	0.1554	3.5532
Bridging oxygen between octahedral Al and tetrahedral Si or Ge	-1.05	0.1554	3.5532
Octahedral Al	1.575	$1.3298 \times 10^{-6}$	4.7943
Tetrahedral Si	2.100	$1.8405 \times 10^{-6}$	3.7064
Tetrahedral Ge	2.100	$1.8405 \times 10^{-6}$	4.73412
<b>Bond parameters for the force field</b>			
<b>Species <i>i</i></b>	<b>Species <i>j</i></b>	<b><i>k</i> (kcal/mol Å<sup>2</sup>)</b>	<b><i>r<sub>o</sub></i> (Å)</b>
Hydroxyl O	Hydroxyl Hydrogen	554.1349	1.000

We test the force field by comparing the experimental and computed structural properties of the three structures. The crystal structures were subjected to energy minimization simulations with steepest descent followed by conjugate gradient algorithms until the maximum energy gradient at any atom was below 1 kcal/mol/Å. The values of Al-O and Ge-O bond lengths were obtained by averaging over all the Al-O and Ge-O bonds present in the crystal structure. To further validate the applicability of the force field, we compared the measured infrared spectra of the AlSiGeOH nanotubes at various compositions with the corresponding simulated vibrational power spectra of the nanotubes (see Section 5.3.1). The spectra were computed by a 4096-point Fast Fourier Transform of the VACF obtained from a 5 ps NVT-MD simulation with a timestep of 0.25 fs and trajectory sampling at every time step.

### **5.2.2. Molecular Dynamics (MD) simulations**

Atomically detailed models of AlSiGeOH nanotubes were built with  $x = 0, 0.25, 0.5, 0.75,$  and 1. The number of Al atoms in the circumference ( $N$ ) ranged between 14 to 50, corresponding to nanotube outer diameters of 1.5-4.1 nm. The models were built using locally-developed computer codes that construct the asymmetric units of the nanotubes, apply the cylindrical symmetry operations, and prepare the fractional coordinates of the nanotube atoms for input to the MD simulation. All the MD simulations were carried out using the Discover module of Materials Studio 3.2 molecular simulation (Accelrys, Inc). For AlSiGeOH nanotubes with both Si and Ge present, the substitution of Si with Ge atoms was carried out systematically proceeding

along the circumference. For example, at  $x = 0.5$  every alternate Si atom along the circumference was replaced with a Ge atom, and at  $x = 0.75$  one in every four Si atoms was replaced by Ge. The latter model was then used to obtain the structure for  $x = 0.25$  by “inverting” the Si and Ge atom locations. All simulations were performed on electrically neutral and isolated nanotubes to avoid any effects of inter-tube interactions. The  $a$  and  $b$  dimensions of the orthorhombic unit cell were maintained at 7 nm (at least) to avoid intertube interactions. To avoid system size effects and to generate a statistically valid ensemble, we used a supercell composed of 2 unit cells along the nanotube axis with a resulting  $c$ -axis dimension of 1.68 nm. Simulations done with only one unit cell produced essentially the same results albeit with a larger statistical error. The nanotube structures were first subjected to energy minimizations with steepest descent and conjugate gradient algorithms until the maximum energy gradient at any atom was below 1 kcal/mol/Å. The unit cell parameters were also allowed to be optimized during this step. The normal-mode vibrational frequencies were then calculated, and the radial breathing mode (RBM) frequency - which is sensitive to the nanotube diameter - was distinctly identified *via* the normal mode eigenvectors. The optimized structures were then subjected to equilibration NVT MD simulations at 298 K with a 0.9 fs integration time step for up to 20 ps. The energy and temperature of the systems was found to be equilibrated typically within 1–2 ps. Subsequently, 100 ps NVT MD simulations were performed to calculate the ensemble average internal energy (potential + kinetic) of the nanotubes as a function of their diameters using five 15 or 20 ps blocks of data to obtain an average energy and error bar. A Berendsen thermostat with a decay constant of 0.1 ps was used to control the temperature, because it was found to be much more stable than the Nosé-Hoover

thermostat. Specifically, it allowed us to maintain the average temperature at  $298\pm 7$  K, which could not be uniformly achieved using a Nosé-Hoover thermostat even after considerable effort in selecting the heat bath coupling strength. The equations of motion under the Berendsen thermostat do not strictly maintain the canonical ensemble (NVT) trajectories. However, it has been shown that with a decay constant of 0.1 ps or higher, the fluctuations in kinetic energy are comparable to fluctuations in the total energy of the system<sup>190</sup>. Moreover, we did not observe any drift of the total energy with time, indicating that the deviations from the NVT ensemble are negligible in this case. Hence, we use this thermostat consistently across all the simulations to provide physically realistic results.

### **5.3. Results and Discussion**

#### **5.3.1. Force field parameterization and validation**

Table 5.2 summarizes the comparison between the predicted and experimental structural properties of geometry-optimized C-phase of  $\text{Na}\{\text{AlGeO}_4\}$ , D-phase of  $\text{K}\{\text{AlGeO}_4\}$  and  $\alpha\text{-GeO}_2$ <sup>88</sup>. There is good agreement of the geometry-optimized lattice parameters and bond distances of tetrahedral Ge-O and Al-O bonds with the experimental crystal structures, thus strongly suggesting that the force field describes their crystal structures well.

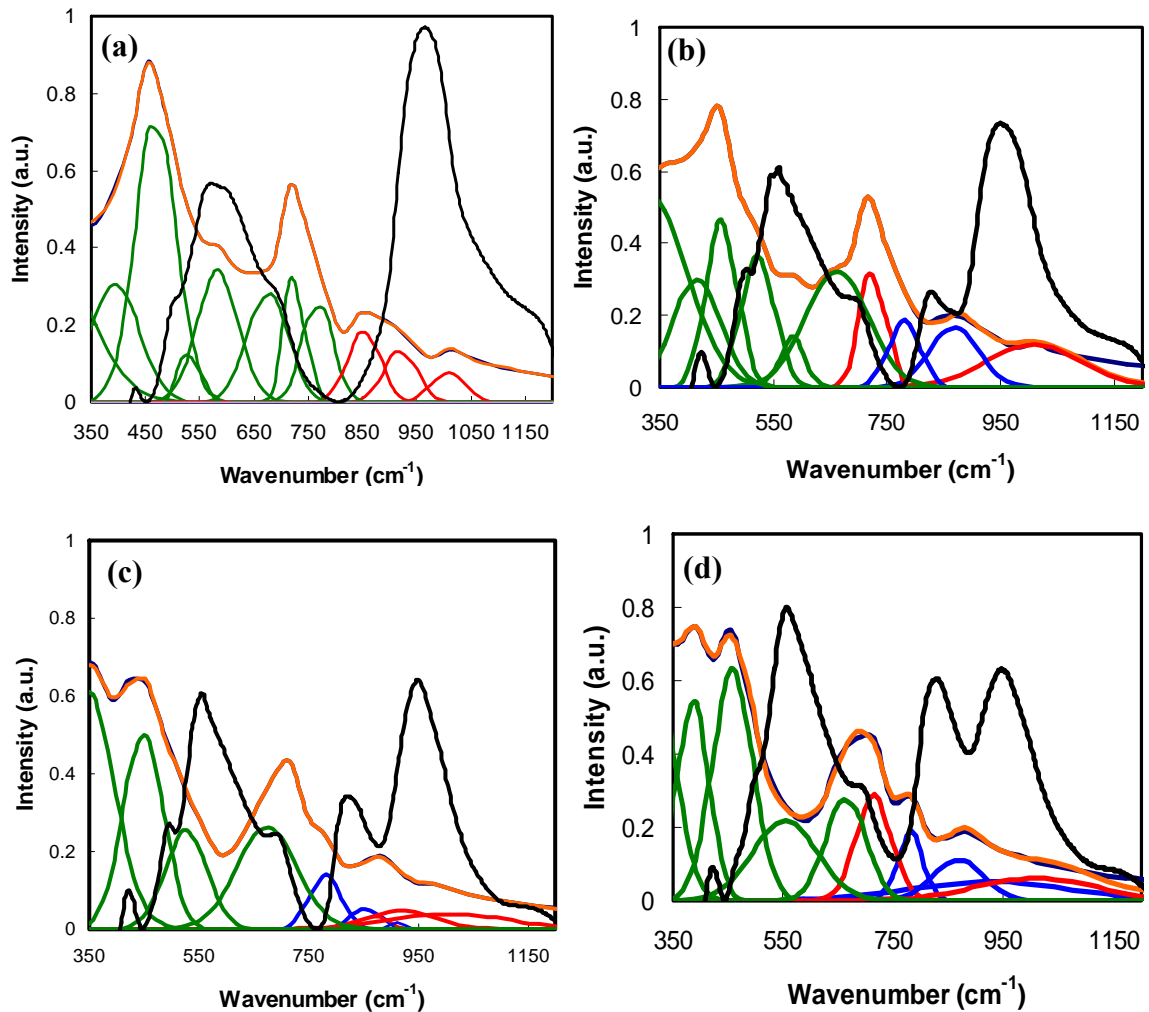
**Table 5.2:** Comparison of simulated (using final force field parameters) structural properties of C-phase of Na{AlGeO<sub>4</sub>}, D-phase of K{AlGeO<sub>4</sub>} and  $\alpha$ - GeO<sub>2</sub> with experimental crystal structure data.

	Na{AlGeO <sub>4</sub> }		K{AlGeO <sub>4</sub> }		$\alpha$ - GeO <sub>2</sub>	
	Comp.	Expt.	Comp.	Expt.	Comp.	Expt.
a (Å)	8.671	8.783	18.416	18.429	4.923	4.985
b (Å)	15.139	15.432	18.416	18.429	4.923	4.985
c (Å)	8.272	8.252	8.882	8.599	5.617	5.648
$\alpha$ (deg)	90	90	90	90	90	90
$\beta$ (deg)	90	90	90	90	90	90
$\gamma$ (deg)	90	90.1	120	120	120	120
$\rho$ (g/cc)	3.42	3.32	3.10	3.19	4.42	4.29
Al-O	1.738	1.751	1.747	1.747	----	----
Ge-O	1.732	1.741	1.727	1.745	1.744	1.738

The quality of the Ge parameterization was further ascertained by comparing power spectra of AlSiGeOH nanotubes (calculated using geometry optimized structures) with experimental FTIR spectra. In order to provide a direct comparison between the experimental IR and calculated vibrational spectra, each computed power spectrum was deconvoluted into a series of Gaussian peaks that correspond to vibrational spectral positions. The procedure briefly involves fitting the spectra of pure nanotubes (AlSiOH and AlGeOH) with a minimum number of Gaussian peaks to obtain an accurate fit. Then, the peak positions due to Al-O, Si-O and Ge-O vibrations are fixed while varying the

intensity and peak widths of all the Gaussians in the pure nanotube spectra to obtain the Gaussians fits for the intermediate AlSiGeOH nanotubes. Figures 5.1(a)-(e) show the computed vibrational spectra and the corresponding experimental IR spectra for AlSiGeOH nanotubes with  $x = 1, 0.75, 0.5, 0.25, 0.0$ , respectively<sup>88</sup>. Wada<sup>85</sup> previously assigned the vibrational modes observed in AlSiOH and AlGeOH nanotube materials into three groups: (i) frequencies between 400-700  $\text{cm}^{-1}$  are due to Al-O-Al vibrations involving a large number of atoms (i.e., phonon-like vibrations), (ii) higher frequency modes at  $\sim 930$  and  $975 \text{ cm}^{-1}$  in AlSiOH nanotubes are due to localized vibrations in Si-OH and Al-O-Si linkages, and (iii) frequency modes at  $\sim 819$  and  $883 \text{ cm}^{-1}$  in pure AlGeOH nanotubes are due to localized vibrations in Ge-OH and Al-O-Ge linkages. Analysis of our computed power spectra confirms these assignments. It should be noted that power spectra obtained from MD simulations can reliably reproduce only the positions of spectral bands observed in experimental vibrational spectrum. However, the intensities of the spectral bands cannot be compared directly between the computed power spectra and experimental vibrational spectra, because there is a large difference in the magnitude of atomic vibrations in MD simulations (that are ultimately reflected in the power spectrum) as compared to the fluctuations of the corresponding electric dipole moments (which are ultimately reflected in experimental IR spectra)<sup>171,177,191</sup>. The results shown in Figures 5.1(a)-(e) clearly suggest that the force field well reproduces the positions of the aforementioned absorption bands; although small deviations ( $\sim 10 \text{ cm}^{-1}$ ) in the peak positions for Si-O and Ge-O vibrations are observed in the computed vibrational frequencies relative to the experimental vibrational spectra. This is a typical level of deviation in force fields developed for inorganic oxide materials<sup>171,177,192</sup>. In

addition, the force field provides a very good prediction of the progressive shifts in the absorption band frequencies of Si-O and Ge-O vibrations with varying Ge content in the nanotubes. There are no significant differences between the different nanotube materials in the calculated low-frequency vibrational modes, as corroborated by the experimental vibrational spectra. Overall, our validation studies support the applicability of the force field for the present investigation.



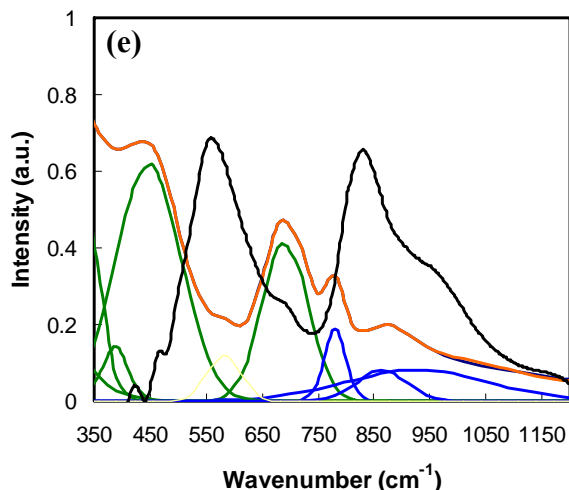


**Figure 5.1:** Comparison between computed vibrational power spectra (orange) and experimental IR spectra (black) for AlSiGeOH nanotubes (a)  $x = 1$ , (b)  $x = 0.75$ , (c)  $x = 0.5$ , (d)  $x = 0.25$ , and (e)  $x = 0$ . The Gaussian curves indicated in red are Si-O vibrations, blue are Ge-O vibrations and green are Al-O vibrations.

### 5.3.2. Energy Minima in Single-Walled Metal Oxide Nanotubes

Molecular dynamics simulations were employed to calculate the total internal energy (potential and kinetic) per atom of the nanotubes as a function of  $x$  (composition) and the diameter (expressed in terms of the number of Al atoms,  $N$ , in the circumference of the nanotube). Figure 5.2 shows the baseline-subtracted energy (see following discussions) of the nanotubes on a per-atom basis versus the nanotube diameter, for each composition investigated. It clearly indicates energy minima with respect to the diameter for each nanotube composition explaining the observed monodispersity in diameter in single-walled AlSiGeOH nanotubes<sup>88,193</sup>. Furthermore, the minima shift progressively to higher diameters with increasing Ge content. In contrast, carbon nanotubes and their analogous materials do not exhibit such a behavior, and their energy was found to decrease monotonically with increasing nanotube diameter<sup>100</sup> suggesting that internal

energy criteria cannot be employed to synthesize carbon nanotubes with desired diameters.

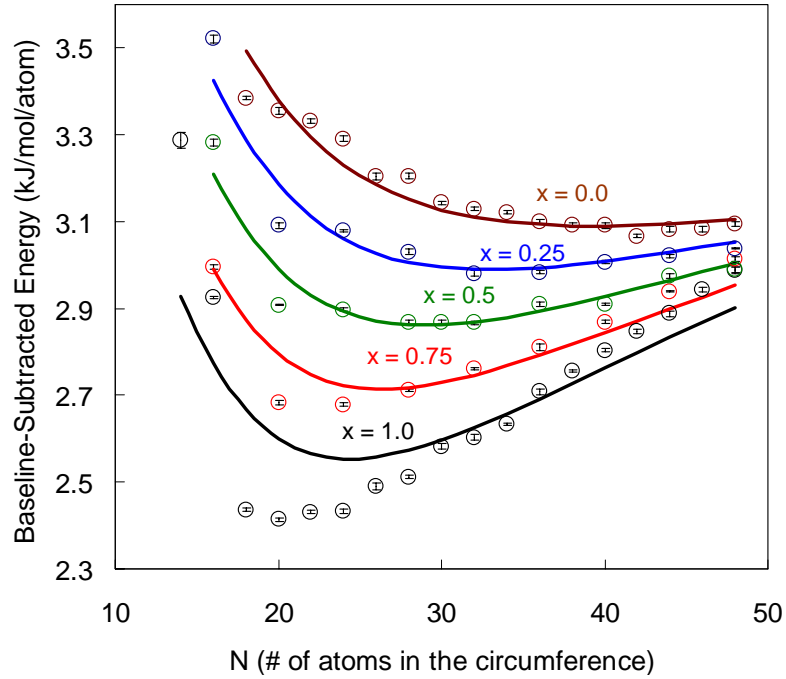


**Figure 5.2:** Total energy per atom at 298 K of AlSiGeOH nanotubes as a function of number of aluminum atoms ( $N$ ) in the nanotube circumference, for  $x = 1.0$  (black), 0.75 (red), 0.5 (green), 0.25 (blue) and 0 (brown). Open symbols denote MD calculations and solid lines denote harmonic strain energy model fits (see Section 5.3.3).

Figure 5.3 shows the computed radial breathing mode (RBM) frequency ( $f_{RBM}$ ) of the nanotubes as a function of the radius ( $R$ ). A power law dependence of the RBM frequency ( $f_{RBM} = CR^{-1}$ ) on the nanotube radius is observed for all the nanotube compositions. The constant,  $C$  ( $\text{cm}^{-1} \cdot \text{nm}$ ) listed in Table 5.3 decreases with increasing Ge content. This is intuitive considering both the increased mass of Ge-containing nanotubes as well as the red shifts of stretching frequencies observed in the IR spectra with

increasing Ge content (e.g., from  $\sim 930, 975 \text{ cm}^{-1}$  for AlSiOH to  $819, 883 \text{ cm}^{-1}$  for AlGeOH). The power law dependence is also predicted by our model (described below).

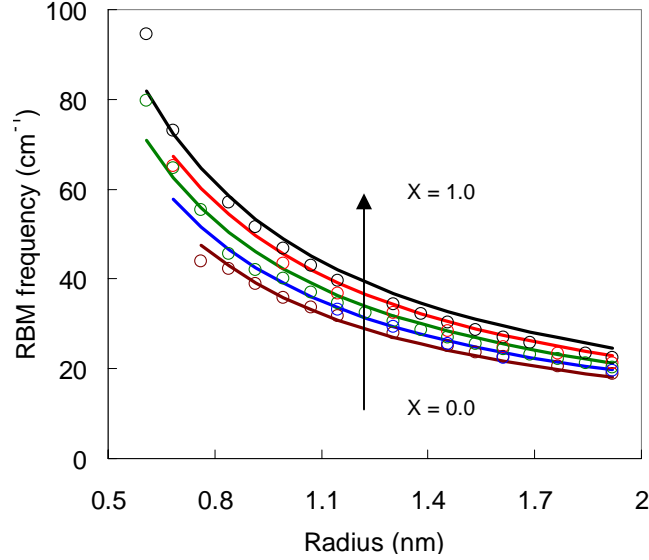


**Figure 5.3:** Computed Radial Breathing Mode (RBM) frequencies versus nanotube radius for AlSiGeOH nanotubes at  $x = 1$  (black),  $0.75$  (red),  $0.5$  (green),  $0.25$  (blue) and  $0$  (brown). Open symbols denote MD simulations and solid lines denote harmonic strain energy model fits.

**Table 5.3:** Comparison between computed (from normal mode analysis) and power law fits of the theoretical expression for the RBM frequency in different AlSiGeOH nanotube compositions.  $R$  is the nanotube radius in nm and the RBM frequencies are in  $\text{cm}^{-1}$ .

Composition ( $x$ )	Computed power law	Theoretical power law fit
1	$f_{\text{RBM}} = 47.5R^{-1.19}$	$48.6R^{-1.04}$
0.75	$f_{\text{RBM}} = 43.0R^{-1.10}$	$45.2R^{-1.04}$
0.5	$f_{\text{RBM}} = 41.0R^{-1.11}$	$42.0R^{-1.04}$
0.25	$f_{\text{RBM}} = 39.2R^{-1.14}$	$38.8R^{-1.04}$
0	$f_{\text{RBM}} = 35.5R^{-0.96}$	$35.7R^{-1.03}$

### 5.3.3. Harmonic Force Constant Model

To model the total energy of the nanotube, we consider the nanotube as a cylindrical structure that is composed of “semi-rigid” aluminum octahedra and silicon/germanium tetrahedra, connected by oxygen atoms. The octahedra and tetrahedra are assumed to maintain their ideal O-Al-O, O-Si-O and O-Ge-O bond angles ( $90^\circ$ ,  $109.5^\circ$ , and  $109.5^\circ$  respectively) but allow stretching of their Al-O, Si-O and Ge-O bonds<sup>88,193</sup>. This idealization is in the spirit of the “central force” models<sup>194,195</sup> that describe structural changes in terms of bond length changes rather than bond angles. Such a model is primarily useful for predicting the total energy and related properties, not for accurate predictions of the geometry. Indeed, a further refined model of this type can be constructed by including bond angle distortions (in addition to bond lengths) as harmonic functions. Similarly, the MD simulations can be used to track the nanotube geometry (bond lengths and angles) as a function of diameter and composition. However, we believe that these extensions are currently unwarranted, because one cannot separate the energetic effects of bond angle and bond length changes using force fields based upon the Born ionic model (such as the present one). In particular, they contain a combination of many-body long-range terms as well as two-body short-range terms. Within our model, the strain energy contribution from the metal-oxide bonds are given by harmonic bond stretching potentials<sup>193</sup>,

$$V_{Al-O} = K_1(d_1 - d_{1e})^2, V_{Si-O} = K_2(d_2 - d_{2e})^2 \text{ and } V_{Ge-O} = K_3(d_3 - d_{3e})^2 \quad (5.1)$$

Here  $K_1$ ,  $K_2$  and  $K_3$  are the force constants,  $d_1$ ,  $d_2$  and  $d_3$  are the bond lengths, and  $d_{1e}$ ,  $d_{2e}$  and  $d_{3e}$  are the equilibrium bond lengths of Al-O, Si-O and Ge-O bonds, respectively. The peripheral O-H bonds would make no contribution to the strain energy, and are not considered. For a nanotube with  $N$  aluminum atoms in the circumference, there are  $4N$  Al-O bonds,  $3Nx$  Si-O bonds,  $3N(1-x)$  Ge-O bonds, and  $14N$  atoms in the unit cell. The total internal energy of the nanotube is written as a summation of strain-independent and strain-dependent terms as given by Eq. 5.2.

$$E(N) = E_0 + 4NK_1(d_1 - d_{1e})^2 + 3N[xK_2(d_2 - d_{2e})^2 + (1-x)K_3(d_3 - d_{3e})^2] \quad (5.2)$$

The strain-independent term ( $E_0$ ) contains the kinetic energy and the remaining interatomic potential energies (e.g., O-H) that do not depend on the nanotube radius but are still proportional to the number of atoms in the nanotube. Hence, we normalize the above equation by the total number of atoms in the unit cell.

$$\bar{E}(N) = \bar{E}_0 + \frac{2}{7}K_1(d_1 - d_{1e})^2 + \frac{3}{14}[xK_2(d_2 - d_{2e})^2 + (1-x)K_3(d_3 - d_{3e})^2] \quad (5.3)$$

The bond lengths are a function of number of atoms in the circumference and can be geometrically-related to the nanotube radius as given by Eq.5.3:  $d_1 = (2R/\sqrt{6})\sin(2\pi/N)$  and  $d_2 = d_3 = d_1/\sqrt{2}$ . The expression for the RBM frequency was derived by considering the Lagrangian of the strain-dependent term in Eq.5.2.

$$L = \frac{1}{2} m \dot{R}^2 - 4NK_1(d_1 - d_{1e})^2 - 3N[xK_2(d_2 - d_{2e})^2 + (1-x)K_3(d_3 - d_{3e})^2] \quad (5.4)$$

A Lagrangian equation,  $d(\partial L / \partial \dot{R}) / dt = \partial L / \partial R$ , was then used to obtain the harmonic RBM frequency:  $\omega_{RBM} = 2\pi f_{RBM} = \sqrt{4N(4K_1 + 1.5[xK_2 + (1-x)K_3]) / 3M} \sin(2\pi / N)$ . Here, the unit cell mass is  $M = N(2m_{Al} + xm_{Si} + (1-x)m_{Ge} + 7m_O + 4m_H)$ . The two expressions for  $\bar{E}$  (Eq. 5.3) and  $f_{RBM}$  (Eq. 5.4) are then fitted simultaneously by nonlinear least squares to the MD data (internal energies and RBM frequencies) to obtain the physical parameters:  $K_1$ ,  $K_2$ ,  $K_3$ ,  $d_{1e}$ ,  $d_{2e}$ ,  $d_{3e}$ , and  $\bar{E}_0$  (the latter parameter varies with the composition). The best fits for the equilibrium bond lengths are  $d_{1e} = 0.197$  nm,  $d_{2e} = 0.159$  nm and  $d_{3e} = 0.173$  nm. These are in accord with the nominal octahedral Al-O ( $\sim 0.19$  nm) and tetrahedral Si-O ( $\sim 0.16$  nm), Ge-O ( $\sim 0.175$  nm) bond lengths observed in oxide materials<sup>171,188,196,197</sup>. The fitted values for the harmonic force constants are:  $K_1 = 2.541 \times 10^4$  kJ mol<sup>-1</sup> nm<sup>-2</sup>,  $K_2 = 5.849 \times 10^4$  kJ mol<sup>-1</sup> nm<sup>-2</sup>, and  $K_3 = 1.567 \times 10^4$  kJ mol<sup>-1</sup> nm<sup>-2</sup>, respectively. These values suggest that the Ge-O bond has the weakest force constant, while that of Al-O bond is intermediate between the Si-O and Ge-O bonds. The theoretical predictions yield power law fits of the RBM frequencies as a function of the radius, which are in very good agreement with the power law fits obtained from the MD simulations as seen in Figure 5.3. The fitted values of the strain-independent baseline energy  $\bar{E}_0$  are -571.26 kJ mol<sup>-1</sup> ( $x = 1$ ), -564.50 kJ mol<sup>-1</sup> ( $x = 0.75$ ), -557.69 kJ mol<sup>-1</sup> ( $x = 0.5$ ), -550.98 kJ mol<sup>-1</sup> ( $x = 0.25$ ), and -544.26 kJ mol<sup>-1</sup> ( $x = 0$ ). Considering that  $\bar{E}_0$  is only a baseline energy parameter which is not correlated with the other parameters, the number of fitting parameters is quite small in relation to the quantity of data, as well as the internal

constraints in the model which ensure convergence to physically realistic parameter values. For example, the RBM frequency depends only on a weighted summation of the three force constant parameters, which are therefore constrained since they must also be positive in sign. Additionally, the equilibrium bond distances and force constants are constrained further by the harmonic potential terms, which rapidly increase if these parameters assume unrealistic values.

The solid lines in Figure 5.2 show the predictions of the model with the final set of fitted parameters. The model well reproduces the progressive minima in the nanotube energy as a function of nanotube diameter, and also predicts the internal energy versus  $N$  in close agreement with the computational data. Figure 5.4 shows Al-O, Si-O and Ge-O bond strain energies as a function of  $N$  calculated using Eq. 5.1 and the parameters obtained from the fits. While the contribution of Al-O bond-strain energy to the total energy per atom of the nanotube decreases monotonically with increasing nanotube diameter, the Si-O and Ge-O bond strain energies increase. If the inner and outer surfaces of the nanotube are identical, with no silanol or germanol groups bound on the inner surface, then the last two terms in Eq. 5.3 would not exist. Then the total energy of the nanotube would decrease monotonically with increasing  $N$ , and the lowest-energy structure will be that of the planar gibbsite sheet. For the same reason, a grapheme sheet has a lower energy than the carbon nanotube<sup>100,198</sup>. However, due to the functionalization of the inner surface with silanol or germanol groups, and the difference in Si-O/Ge-O and Al-O bond energies, a strain energy minimum is observed in Figure 5.2. Due to a weaker Ge-O force constant in comparison to Si-O, the minimum shifts

towards larger diameters as the Ge content increases. Thus, the incremental substitution of different tetrahedral metal atoms on the inner surface of a nanotube as a potential means of tuning the nanotube diameter, indeed exhibits a strong correlation with the composition-dependent changes in the internal energy of the nanotube, as illustrated by the present case of Si/Ge substitution.

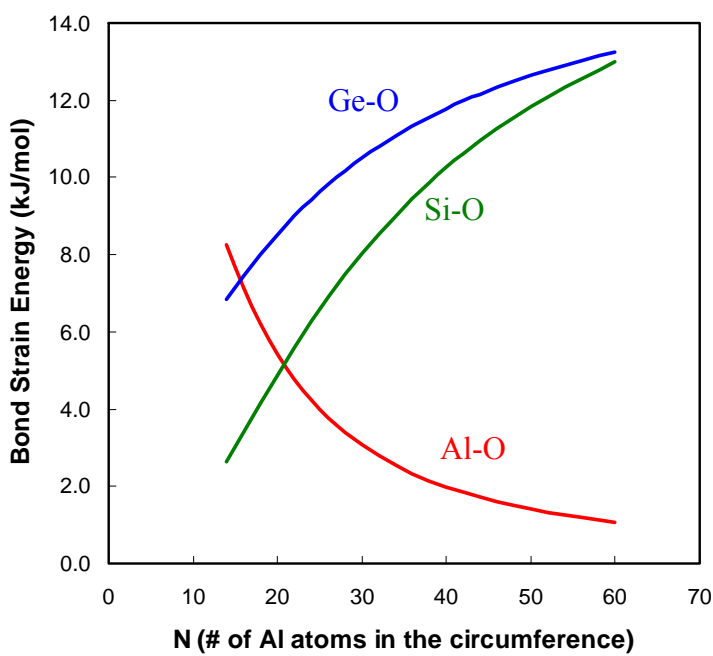


**Figure 5.4:** Bond strain energies of Al-O(red), Si-O(green)/Ge-O(blue) as a function of the number of aluminum atoms (N) in the circumference.

#### 5.3.4. Comparison of experimental and predicted nanotube diameters

In order to quantitatively investigate whether the predicted continuous shift in outer diameter with composition occurs under real synthesis conditions, we compare, in Figure 5.5, the experimental estimates of nanotube diameter with the computational predictions and the predictions from the fitted strain energy model, as a function of the

composition. The experimental values of nanotube diameter were obtained from X-ray diffraction (XRD) and transmission electron microscopy (TEM) techniques<sup>88</sup>. The low-angle Bragg peak (d-spacing) in the XRD pattern was correlated to the nanotube diameter. The effect of packed morphology of the tubes on the diameter was incorporated using an ‘offset’ value determined from TEM images of the nanotubes. In the case of the computational and theoretical predictions, the nanotube whose diameter corresponds to the lowest internal energy is taken as the product expected in the synthesis carried out with that particular composition. The computational and model predictions match well, as might be expected considering that the physical parameters in the model were fitted using the computational data. Furthermore, they also correctly capture the experimentally observed trend in the diameter which increases with increasing Ge content. In other words, our current results clearly establish that there is a strong correlation between the composition, diameter, and internal energy of the AlSiGeOH nanotubes. The quantitative deviations of the experimentally estimated diameters from the computational and model predictions may be due to several factors. Firstly, the relation between the XRD peak position and the diameter is semi-quantitative. Detailed modeling and fitting of the XRD patterns is required to obtain the diameter more accurately, and is beyond the scope of this work. Secondly, the force field itself is fundamentally an approximation of the true energetics of the system. Finally, although the internal energy is almost always used to parameterize force fields and to investigate the relative stability of similar materials, it is possible that a more accurate analysis would involve the calculation of quantities such as the free energy, as well as the consideration of the solution properties and mechanistic details of the synthesis. Although quantitative knowledge of the synthesis mechanism<sup>185</sup>

is emerging, the above complications (i.e., interpretation of experimental data, lack of accurate thermodynamic properties) are frequently encountered in the characterization and analysis of nanoscale materials. In our view, the present study shows for the first time a clear connection between nanotube dimensions, composition, and internal energy, thus substantiating the possibility of nanotube engineering *via* manipulation of interatomic potential energies and hence the thermodynamic properties.

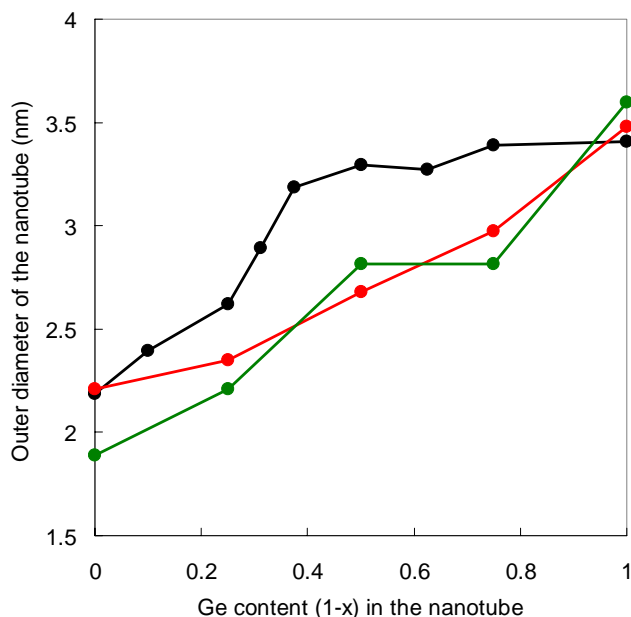


**Figure 5.5:** Comparison of AlSiGeOH nanotube diameters versus nanotube compositional parameter  $x$ : computed (green), theoretical (red), and experimental (black) results.

#### **5.4. Conclusions**

The present study successfully demonstrates the existence of a thermodynamic ‘handle’ for tuning the diameter of single-walled metal oxide nanotubes that can already

be synthesized with tunable compositions. Due to a difference in interatomic bond energies between the octrahedral (Al-O) and tetrahedral (Si-O and/or Ge-O) bonds on the outer and inner surface of the nanotube respectively, a substantial energy minimum occurs with respect to the diameter. Furthermore, the energy minimum can be shifted to different diameters by changing the ratios of the two tetrahedrally coordinated elements (Si and Ge), as corroborated by the experimental results. Finally, the harmonic force constant model that relates the composition of the material to the nanotube energy can provide semi-quantitative guidelines for tuning nanotube dimensions *via* appropriate selection of the octahedral/tetrahedral species combinations.

# CHAPTER 6

## WATER TRANSPORT AND ADSORPTION IN SINGLE-WALLED ALUMINOSILICATE NANOTUBES

### 6.1. Introduction

Single-walled aluminosilicate nanotubes are attractive materials for construction of nanofluidic devices due to their unique properties that are quite different from those of carbon nanotubes, including short lengths, complex internal structure, hydrophilicity due to the presence of hydroxyl groups on the inner and outer surfaces of the nanotube, functionalizable interiors due to the presence of hydroxyl groups, and ability to disperse in polar solvents. Unlike the atomically smooth and uniform pores of the carbon nanotubes, these nanotubes present a non-uniform interior with periodic wide (inner diameter  $\sim 1.6$  nm) and narrow (diameter  $\sim 1$  nm) pore regions as seen in Figure 6.1. Currently, very little is known about the molecular transport properties of these nanotube materials, and their relation to the transport properties of other nanoporous materials like zeolites and carbon nanotubes.

We therefore present a systematic investigation of water adsorption and diffusive water transport in these nanotube materials<sup>199</sup>. First, we report the results of molecular dynamics simulations to calculate the axial self-diffusivity of water molecules through the nanotubes as a function of water content. We then calculate the transport diffusivity *via* the Darken approximation, by use of the thermodynamic correction factor obtained from adsorption isotherms computed using the Grand Canonical Monte Carlo (GCMC)

simulation technique. We also experimentally study the adsorption of water vapor in the aluminosilicate nanotubes *via* gravimetric sorption analysis technique and compare them with the computed isotherms. Next, we quantify the predictions for diffusive fluxes in the present nanotube materials and make a comparison with those measured and predicted in carbon nanotube membranes and zeolite membranes. The transport fluxes depend substantially on the nanotube length (and also possibly the diameter), which in our nanotube system are well tunable parameters from an experimental viewpoint. We briefly discuss the relevance of our predictions towards the construction of ultra-thin (15-100 nm) nanotube membranes from realistic nanotube materials. Along with the possibility of organic functionalization of the nanotube interior, one can potentially obtain highly permeable nanotube membranes with a range of tunable selectivities.

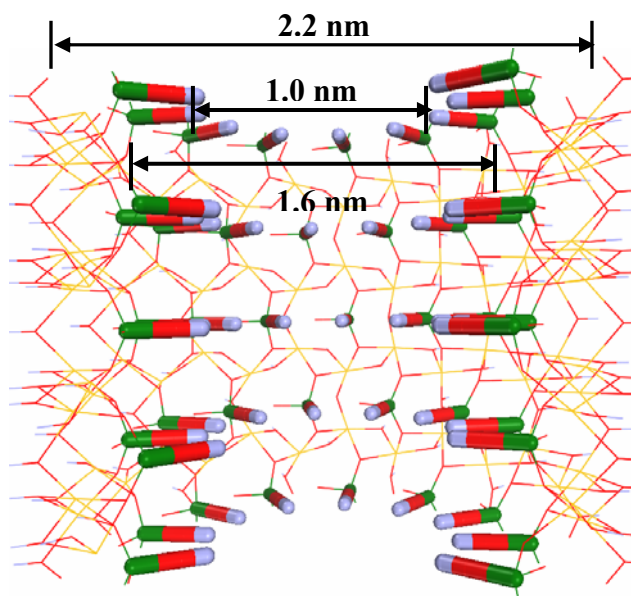


**Figure 6.1:** Side view of an aluminosilicate nanotube shell showing nanotube interior with periodic wide and narrow pore regions. The constrictions of the pore are represented by stick model of silanol groups on the interior nanotube wall, while the rest of the linkages in the nanotube structure are represented by line model. Al (gold), Si (green), Nanotube-O (red), H (purple), Water-O (blue).

## **6.2. Methodology**

### **6.2.1. Computational Details**

#### **6.2.1.1. Nanotube-Water Model Construction**

Single-walled aluminosilicate nanotube models were built using symmetry operations of cylindrical point group  $C_{2nh}$  via locally-developed computer codes to construct the asymmetric units of the nanotubes, apply the cylindrical symmetry operations, and generate the fractional coordinates of the nanotube atoms. Atomically detailed models of the nanotube membranes were then constructed using hexagonally packed aluminosilicate nanotubes with varying numbers of water molecules randomly inserted in the nanotubes. To minimize system size effects and to generate a statistically valid ensemble, we used a supercell ( $2.4 \text{ nm} \times 2.4 \text{ nm} \times 1.68 \text{ nm}$ ) composed of one nanotube with twice the axial unit cell dimension of  $1.68 \text{ nm}$  along the  $c$ -axis. We considered the nanotubes to be flexible, thereby allowing all the atoms to move, and employed a recently developed CLAYFF force field<sup>171</sup> to describe the interactions between the atoms of the nanotube. The force field (Eq. 5.1) is based on an ionic description for metal-oxygen interactions, with fractional charges assigned to each atom and Lennard-Jones (LJ) (12-6) potentials for Al-O, Si-O, and O-O interactions. The interaction between water and the nanotube is described with SPC water parameters in the same manner as described in detail earlier<sup>171</sup>. Bond stretching and bond-bending terms are described with harmonic terms.

All the MD simulations presented here were performed on 3-dimensionally periodic simulation cells using the Discover module of Materials Studio 3.2 molecular simulation program (Accelrys, Inc). Following the insertion of water molecules in the nanotubes, the simulation cells were initially subjected to energy minimizations with steepest descent and conjugate gradient algorithms until the maximum energy gradient for every atom displacement was below 1 kcal/mol/Å. The unit cell parameters were also optimized during this step. The optimized models were then subjected to equilibration NVT-MD simulations at 298 K for 20 ps with a 0.9 fs integration time step. For all the simulations, Ewald summation was used for Coulombic interactions. The energy and temperature were found to be equilibrated typically within 5-10 ps. A Nosé-Hoover thermostat was used to control the temperature during the simulations.

#### 6.2.1.2. Adsorption Isotherms

Adsorption isotherms were calculated at temperatures of 298, 308, 318 and 325 K using a GCMC module incorporated in the MUSIC simulation code<sup>200,201</sup>. The nanotube models employed for the adsorption simulations were larger than the models used in the diffusion study and were constructed as orthorhombic (4.16 nm × 4.8 nm × 3.36 nm), composed of four nanotubes with an axial cell dimension of 3.36 nm along the *c*-axis. The GCMC simulations, which in the current case are computationally less expensive than the MD simulations for diffusion, required larger simulation cells to compute reliable adsorption isotherms. In contrast to the diffusion simulations, we assumed the nanotubes employed for the adsorption simulations to be rigid with the water molecules treated as rigid units. A spherical cutoff distance of 1.3 nm was employed for all the

interactions, while the electrostatic interactions were treated with the smooth cutoff scheme<sup>202</sup>. For each isotherm data point, the GCMC simulations included  $3 \times 10^7$  equilibration Monte Carlo moves and  $7 \times 10^7$  production Monte Carlo moves. An individual Monte Carlo attempt included an insertion, deletion, translation or rotation of a randomly selected water molecule. At the fairly low pressures considered in our study, water vapor was modeled as an ideal gas with fugacity equal to the pressure.

### 6.2.1.3. Diffusivity and Molecular Distribution

The equilibrated nanotube-water models were subjected to NVT-MD simulations for 500-600 ps at 298 K. The average axial self-diffusivities ( $D_s$ ) were calculated for water loadings ranging from near zero to near saturation loading (as determined from adsorption isotherms) using at least five 50-100 ps blocks of diffusion trajectories. The self-diffusion coefficients were derived from the mean square displacements (MSDs) of the water molecules along the axis of the nanotube by employing the power-law form of the Einstein equation (Eq. 6.1):

$$\langle |r(t) - r(0)|^2 \rangle = (2D_s)t^\alpha \quad (6.1)$$

Here  $r(t)$  and  $r(0)$  are the penetrant displacements at simulation times  $t$  and  $t = 0$ , respectively, and  $\alpha$  is the power law exponent. In all cases considered here, we found  $\alpha$  to be very close to 1, confirming that the water molecules are undergoing random-walk diffusion in the nanotubes. The transport diffusivity ( $D_t$ ), which describes the

macroscopic diffusive transport under the influence of a concentration gradient, was then calculated using the Darken approximation given by Eq.6.2<sup>203</sup>.

$$D_t(C) \cong D_s(0) \left( \frac{\partial \ln f}{\partial \ln C} \right)_T \quad (6.2)$$

Here,  $f$  is the fugacity of the bulk gas phase that is in equilibrium with the concentration,  $C$  of the adsorbed phase at a fixed temperature,  $T$ . The thermodynamic correction factor, which is the partial derivative term in the above equation, was obtained from the computed adsorption isotherm of water vapor in the aluminosilicate nanotubes by assuming fugacity and pressure to be equal in the low pressure range considered in the study. In the infinite dilution limit, the corrected diffusivity in the Darken equation can be equated to self-diffusivity as given in Eq.6.2<sup>203</sup>. Following the data production MD simulations, the distribution of water in the nanotubes was obtained by calculating the pair correlation function between the inner hydroxyl groups and water molecules, O-H and O-O pairs of the water molecules, and the axial concentration profile of water in the nanotubes by averaging over configurations, collected at a frequency of 0.45 ps, from a 200 ps trajectory of the nanotube-water system.

## **6.2.2. Experimental Details**

### **6.2.2.1. Nanotube Synthesis and Gravimetric Moisture Sorption Analysis**

Aluminosilicate nanotube synthesis and purification were performed as described in detail elsewhere<sup>87,204</sup>. The quality of the nanotube product was verified by X-ray diffraction. Dialyzed samples were then freeze-dried and used for water vapor adsorption measurements. Adsorption isotherms were measured at the same temperatures as that of the computed isotherms (298, 308, 318 and 325 K) using an automated gravimetric moisture analysis instrument, IGASorp (Hiden Analytical, Warrington, UK). At the beginning of each experiment, about 35 mg of the nanotube sample was dried for 12 h at 200°C using a heater built into the instrument. The adsorption isotherm was then generated by measuring the equilibrium uptake of water by the sample from 0% to 95% relative humidity (RH). At each RH, the sample was allowed to equilibrate for 2 - 8 h until the fluctuation in the sample weight was below 5%, after which the asymptotic value of the sample weight was predicted by the instrument using first order relaxation kinetics.

## **6.3. Results and Discussion**

### **6.3.1. Water Adsorption in Aluminosilicate Nanotubes**

Typically, nanotube bundles present three types of adsorption sites: (i) within the pores of the nanotubes, (ii) within interstitial spaces between the nanotubes, and (iii) in the spaces between individual bundles of the nanotubes<sup>186</sup>. The computed and measured

adsorption isotherms are shown in Figure 6.2 (a)-(b). Both data show a large fraction of water uptake (~13 wt%) occurring in the nanotube bundles below 50 % RH. The computed isotherms exhibit a transition from slow water uptake below 10 % RH to a rapid increase in adsorption between 10-50% RH before attaining saturation at higher pressures. Further, the isotherms at all temperatures exhibit hysteresis during desorption (See Section B.1 in Appendix B), indicative of capillary condensation phenomena. The experimental data, on the other hand, show a higher uptake at low partial pressure/RH but converges towards the computed results above 10% RH. The predictions of saturation loading of water molecules (~ 63 molecules/simulation cell or 0.85g/cc) from the GCMC simulations compare very well with the experimental values. Quantitative differences observed between the measured and computed isotherms can be due to (i) the fixed-lattice approximation which does not account for additional interstitial sorption due to possible swelling of the nanotube bundle, and (ii) possibility of further tuning of the force field employed in the present study.

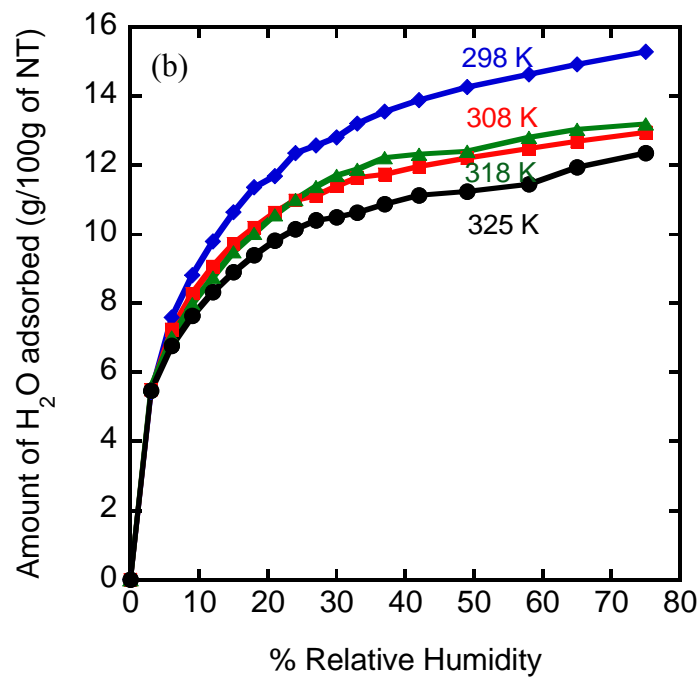
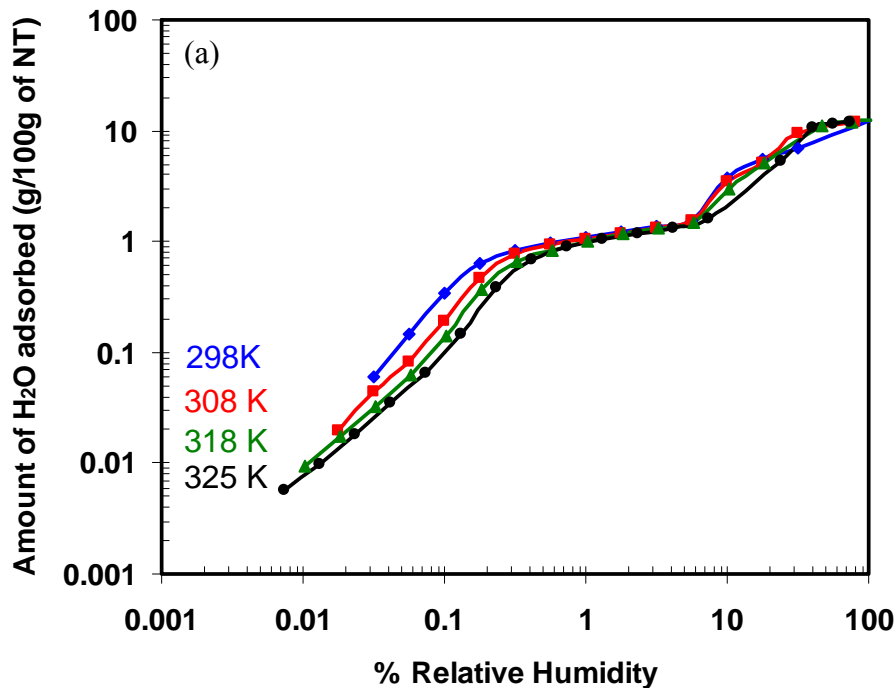


**Figure 6.2:** (a) Computed adsorption isotherms of water adsorbed in single-walled aluminosilicate nanotube as a function of relative humidity at  $T = 298$  (Blue), 308 (Red), 318 (green), and 325 K (black). (b) Measured adsorption isotherms showing amount of water adsorbed in single-walled aluminosilicate nanotube as a function of relative humidity at the same temperatures.

Figure 6.3 shows the site-specific differentiation of the computed total water uptake at 298 K into its components: water uptake in the nanopore, and water uptake in the interstitial spaces between the nanotubes as shown in the snapshot of Figure 6.4. Section B.1 in Appendix B contains similar results at other temperatures. The results suggest that water molecules preferably adsorb into the pores of the nanotube, whereas adsorption into the interstitial spaces becomes significant only at higher pressures. Our data conclusively demonstrates that the nanotube interior is quite hydrophilic - being able to adsorb about 10% by weight of water – without the presence of metal cations. This result is significant, since the metal cations located in the pores of hydrophilic zeolites partially obstruct/slow down the diffusion of water molecules. This limitation is not encountered in the present materials. The temperature dependence of the water loading follows the expected trend for sorption in inorganic porous materials, with a decrease in the amount of water adsorbed with increasing temperature. The apparently higher uptake of water at 318 K compared to 308 K at  $RH > 20\%$  in the experimental isotherms, and at 325 K compared to 298 K at higher relative humidity values in the computed isotherms, is simply a result of normalizing all the isotherms by the saturation vapor pressure so that they can be plotted on a single RH scale. The computed internal energy of adsorption of water vapor in the nanotube was found to be in the range of 40-60 kJ/mol depending upon the loading (see Section B.2. in Appendix B) and is comparable to those reported for hydrophilic aluminosilicate zeolites such as zeolites 3A, 4A and 5A (which are in the range of 47-57 kJ/mol)<sup>205-207</sup>.

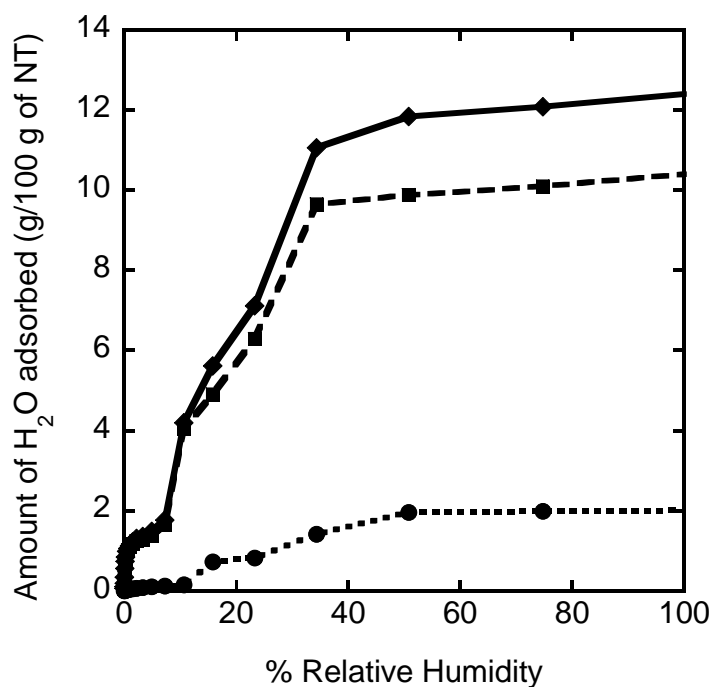


**Figure 6.3:** Deconvolution of computed adsorption isotherms (solid line) of water in Aluminosilicate nanotubes at 298 K into water sorption in the pores of the nanotube (dashed line) and water sorption into the interstitial spaces between the nanotubes (dotted line).

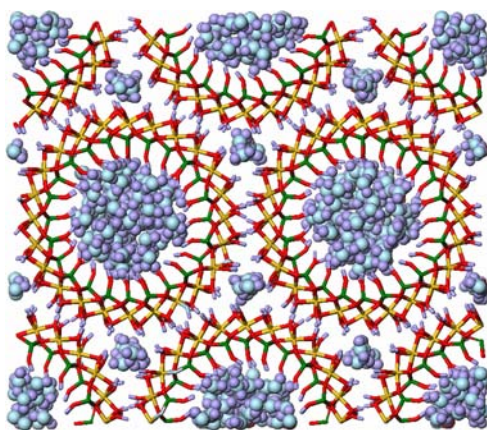


**Figure 6.4:** Snapshot of aluminosilicate nanotube membrane with adsorption of water molecules into nanopores as well as the interstitial spaces between the nanotubes at 100% RH and 298 K. Al (gold), Si (green), Nanotube-O (red), H (purple), Water-O (blue).

As the main objective of our present adsorption simulations is to obtain the thermodynamic correction factors for calculating transport diffusivities, we restrict our discussion of adsorption properties to the essential aspects described above. Our present study is aimed at making a quantitative estimate of the water transport rate through the nanotubes, and also does not consider water dynamics in the interstitial spaces. We therefore evaluate the thermodynamic correction factor of Eq.6.2 using only the computed water uptake in the pores of the nanotube.

### **6.3.2. Water Structure in the Nanotube**

The pair correlation functions and the axial concentration profiles of water in the aluminosilicate nanotubes were obtained from the molecular dynamics trajectories, and are useful in understanding the structure of water inside the nanopores. Figure 6.5 shows the pair correlation function between the oxygen atoms of the water molecules and the hydrogen atoms of the silanol groups on the inner wall of the nanotube. It exhibits two peaks close to the inner wall of the nanotube, with the first peak located at a distance of  $\sim 0.175$  nm and a second peak at 0.295 nm. The occurrence of the first peak very close to the pore wall is observed even at very low water loadings (1 molecule/simulation cell), suggesting that water molecules initially prefer to adsorb and diffuse along the nanopore walls owing to the hydrophilic nature of the hydroxyl groups. With increasing water content, the distribution function shows further well-defined peaks due to next-nearest neighbor contributions. In addition, the location of the second peak – arising from the next-nearest neighbor coordination shell - very close to the first peak indicates a tight (liquid-like) packing of water molecules in the nanopore. Figure 6.6 shows the

distribution profiles of water molecules along the nanotube axis, as calculated from the molecular dynamics trajectories. For clearer representation on a single plot, the profiles have been normalized to have the same total area under all the curves. The observed concentration profiles reveal an interesting evolution of water structure within the aluminosilicate nanotubes. At low water content, the water-nanotube interactions influence the structure of the water molecules, and cause the water molecules to be concentrated in the larger pore spaces ( $\sim 1.6$  nm diameter) between the periodic silanol groups (whose distribution is also shown in Figure 6.6). With increasing water content, well-defined clusters of water molecules are formed in these larger pore spaces as seen in the simulation snapshot of Figure 6.7. The clusters are separated by constricted pore regions ( $\sim 1$  nm diameter) bounded by the silanol groups positioned on the inner wall of the nanotubes. Furthermore, at higher water content, there is a structural transition wherein the water clusters become connected to each other by water molecules located in the narrower regions of the nanotube, as evinced by the appearance of non-zero water concentrations in these regions of the profile. Such a structural transition for adsorbed water appears to be unique among nanotube materials, and is a direct result of the complex internal structure of the present nanotube. The relative peak intensities in the pair correlation functions of the water molecules (Section B.3 in Appendix B) also approach the liquid-like structure of bulk water as the water content increases. Although, the axial concentration profiles of water molecules in the nanotube suggest the formation of water clusters at higher water content in the nanotubes, visual observation of water molecule motion does not indicate any coordinated movement of water clusters diffusing through the nanotubes.

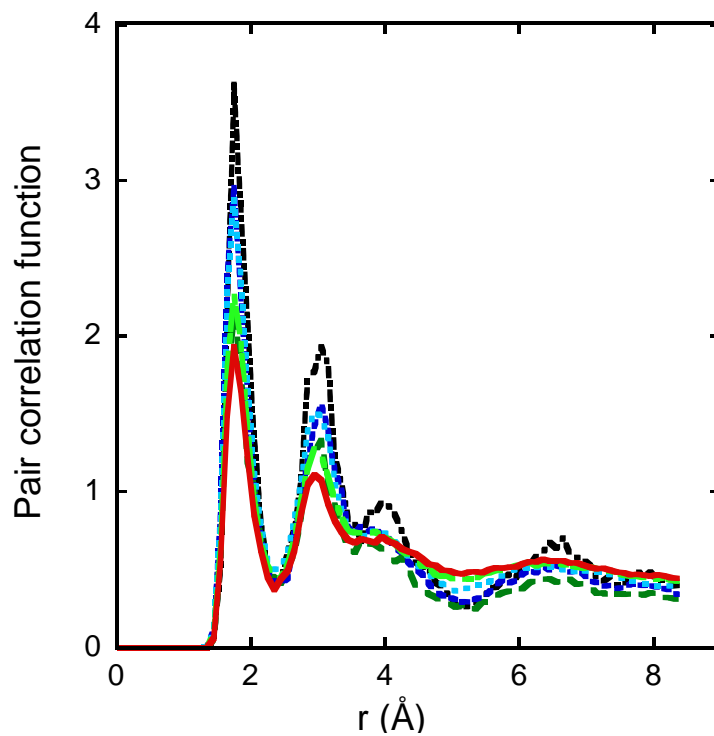


**Figure 6.5:** Pair correlation function between hydrogen atoms of silanol groups and oxygen atoms of water molecules at various loadings of water molecules in the nanotube,  $N = 1$  (black dot and small dashed line), 4 (dark green medium dashed line), 8 (dark blue small dashed line), 16 (light blue dotted line) 32 (bright green large dashed line), 46 (red solid line). Values on y-axis are ratios of local density of water molecules to the average density in the nanotube. Correlation profiles have been increased by 25-50% of their original values to vertically shift the curves with respect to each other for better clarity of the figure.

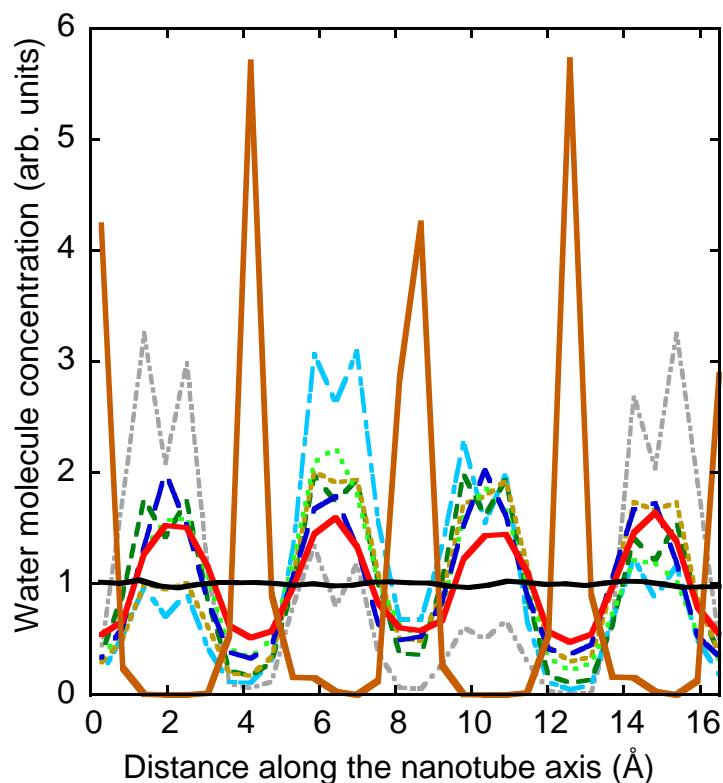


**Figure 6.6:** Normalized distribution profiles of water molecules and silanol groups along the nanotube axis at various loadings of water molecules,  $N = 1$  (grey dot and small dashed line), 2 (light blue dot and large dashed line), 4 (dark green medium dashed line), 8 (dark gold small dashed line), 16 (bright green dotted line), 32 (blue large dashed line), 46 (red solid line), silanol groups (brown solid line), bulk water (black solid line). For better representation on a single plot, the profiles are normalized such that the total area under each curve is the same. To obtain the actual concentration profiles, each curve should be scaled by the corresponding number of water molecules ( $N$ ).

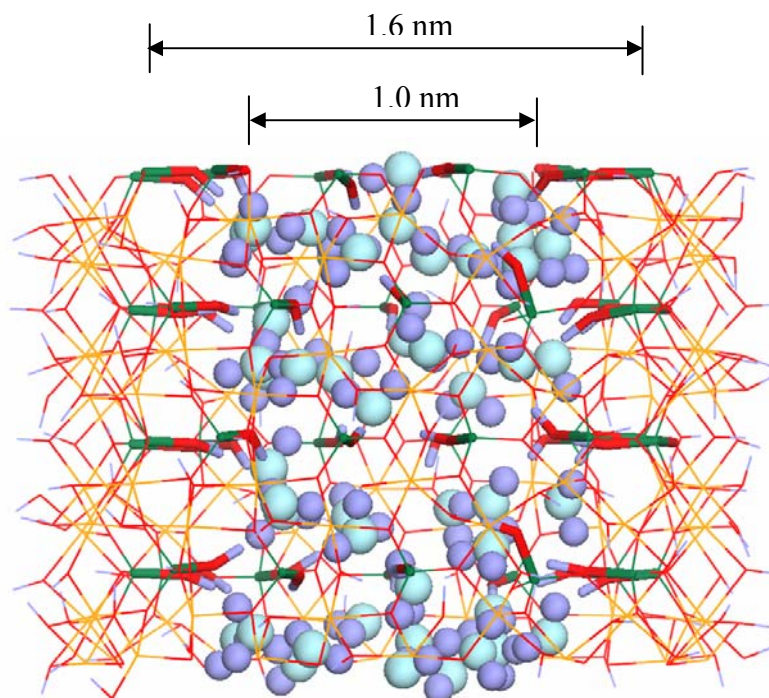


**Figure 6.7:** Snapshot of molecular distribution of water in single-walled aluminosilicate nanotube. Picture shows water segregation into the wider regions of the nanotube at near saturation loading of water molecules (46 water molecules/simulation cell). Al (gold), Si (green), Nanotube-O (red), H (purple), Water-O (blue).

### 6.3.3. Diffusivity and Transport Flux

The axial self-diffusivity of water in the nanotube was calculated as a function of water, from near the infinite dilution limit to the saturation limit. Detailed analysis of the diffusion trajectories revealed a Fickian mechanism ( $\alpha \sim 1$ ) of transport in the nanotubes at all water loadings and throughout the simulation time scales employed in this study (25 – 600 ps)<sup>199</sup>. This is in contrast to the case of carbon nanotubes wherein the water molecules were reported to exhibit a dual transport mechanism: ballistic transport ( $\alpha \sim 2$ ) at simulation time scales  $< 500$  ps followed by slower Fickian diffusion at longer time scales<sup>28,208</sup>. In the present study, 50-100 ps blocks of diffusion trajectories were

sufficient to reliably estimate the averages and error bars in the calculations of the self-diffusion coefficient. Further, we also performed an independent simulation at water content of 16 molecules to see the effect of system size on the self-diffusivities and found that the water diffusivity ( $1.34 \pm 0.318 \times 10^{-9} \text{ m}^2/\text{s}$ ) in a  $\sim 25 \text{ \AA}$  long aluminosilicate nanotube was comparable to the diffusivity ( $1.54 \pm 0.515 \times 10^{-9} \text{ m}^2/\text{s}$ ) in the present  $\sim 16.8 \text{ \AA}$  long nanotube suggesting that the chosen simulation cell dimensions were sufficient to accurately estimate the diffusivities. The axial self-diffusivities of water in the nanotubes are shown in Figure 6.8. In the infinite-dilution limit, the self-diffusivity is about the same as that of bulk liquid water ( $\sim 2.5 \times 10^{-9} \text{ m}^2/\text{s}$ ). The Knudsen diffusion of small hard-sphere molecules in rough nanopores has been studied computationally and theoretically by previous authors<sup>29,209</sup>. For a nanopore of diameter 1-1.7 nm and assuming all molecule-wall collisions to be diffuse, the lower-bound Knudsen diffusivity of water varies from  $6.3 \times 10^{-9} \text{ m}^2/\text{s}$  to  $1 \times 10^{-8} \text{ m}^2/\text{s}$ . The calculated self-diffusivity is considerably lower than the Knudsen value, not only due to the presence of adsorptive wall-molecule interactions but also due to the small pore diameter which is only 4-6 times the kinetic diameter of water (0.27 nm). As a result, the diffusion mechanism can be expected to more closely resemble those found in nanoporous materials such as zeolites. Furthermore, the self-diffusivity decreases with an increase in water content as observed in Figure 6.8. This trend is often seen in simulations of molecular diffusion through zeolite materials as well as carbon nanotubes<sup>208,210</sup>. The loading-dependence of transport of small Lennard-Jones molecules in small nanopores ( $\sim 1 \text{ nm}$  diameter) has also been studied theoretically<sup>211</sup>. This theory indeed predicts a decrease in the self-diffusivity as loading increases, due to repulsive interactions between the adsorbed

molecules. In the context of diffusion in zeolites, a similar interpretation is made by the Maxwell-Stefan theory <sup>212</sup>, with a limiting case of “single-file” diffusion. However, a significant difference between the present nanotubes and zeolites is that the diffusivity in the nanotubes is significantly higher and approaches that of bulk liquid water, whereas the diffusivity of water in hydrophilic zeolites is in the range of  $10^{-10} - 10^{-12} \text{ m}^2/\text{s}$  <sup>213</sup>. This is due to the fact that the pore diameter of the nanotube is somewhat larger than that of typical zeolites, although still well below that of mesoporous materials (2 nm and higher), which affects the diffusivity <sup>214</sup> as well as the absence of pore-blocking metal cations in the nanotube presenting wider pore spaces for the diffusing molecules.

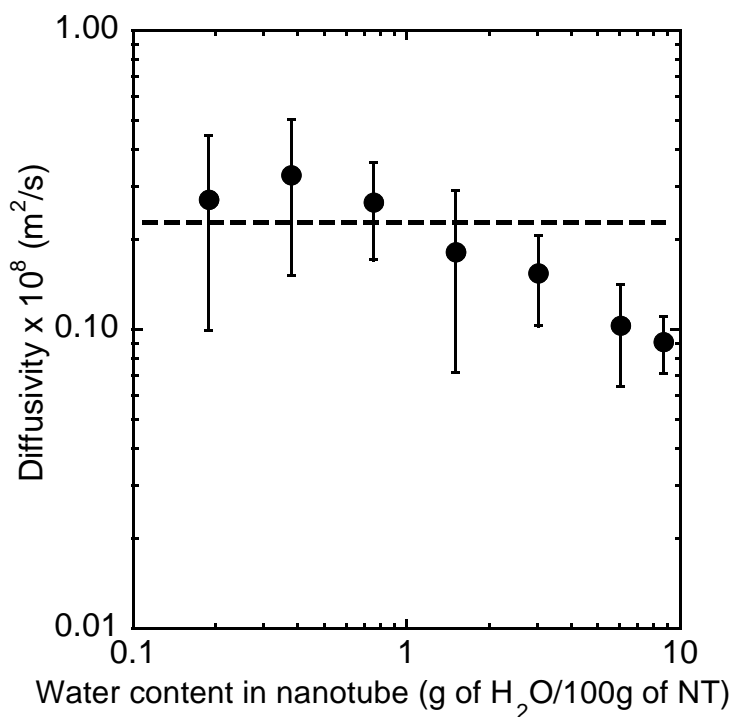


**Figure 6.8:** Axial self-diffusivities ( $D_s$ ) of water in single-walled aluminosilicate nanotubes as a function of water content in the nanotube, calculated at water loadings varying from 1 to 46 water molecules/simulation cell (corresponding to a water content of 0.19 to 8.7 gm of  $\text{H}_2\text{O}/100$  gm of nanotube). Dashed line indicates diffusivity of bulk water.

The mechanistic similarities between the transport behavior of water in the nanotubes and in other nanoporous materials, allows the use of similar approaches towards estimating the transport diffusivity and predicting the water flux through the nanotubes. The transport diffusivities were determined by combining the self-diffusivity at infinite-dilution obtained from MD simulations with the thermodynamic correction factor calculated from computed adsorption isotherm at 298 K, by means of the so-called Darken approximation (Eq. 6.2). As previously demonstrated by Skoulidas and Sholl <sup>97</sup>, the Darken approximation is quite accurate for predicting the transport diffusivities of molecules with sizes considerably smaller than the nanopore diameter, which is the case here since the inner diameter of the aluminosilicate nanotubes is about five times larger than the size of a water molecule. A slight overestimation of the transport diffusivities may be possible as the Darken approximation assumes that the corrected diffusivity is entirely independent of pore loading. Nevertheless, the approximation is unlikely to cause any order-of-magnitude errors in the diffusivity predictions. The predicted transport diffusivity of water in aluminosilicate nanotubes monotonically increased with an increase in water content, while the self-diffusivity decreased with increasing water content. In general, the transport of water through the present nanotube materials is considerably faster than in hydrophilic zeolites and other similar nanoporous oxide materials. Although the narrowest constrictions of the pore in the nanotubes (comprising a nuclear distance of about 1 nm between oxygen atoms on diametrically opposite silanols) are comparable to the corresponding distances in medium-pore and large-pore zeolite materials, a major difference between the two types of materials is the fact that the aluminosilicate nanotube framework is charge-balanced and does not ordinarily include

metal cations in the pores. Previous elemental analysis studies<sup>88</sup> do not reveal any significant concentration of alkali metal cations inside these materials. On the other hand, aluminosilicate zeolite frameworks have a net negative charge balanced by metal cations (such as Na<sup>+</sup>, K<sup>+</sup>, or Ca<sup>2+</sup>). As a result, the strong water binding sites and partial obstruction of the pore apertures caused by the metal cations in zeolites, do not appear in the present nanotube material and are an important cause of the significantly higher transport diffusivity in the nanotube.

The combination of relatively high water diffusivity with the capability to obtain very short (15-100 nm) nanotubes of the present structural type<sup>87,204</sup> leads to a number of possibilities for fabricating high-throughput membrane devices. Furthermore, the complexity of the internal structure in contrast to materials such as carbon nanotubes (specifically, the existence of pendant silanol groups) creates the potential for attachment of functional groups capable of molecular recognition, selective transport, or switching/gating behavior in response to an external stimulus. Short nanotubes of this nature can be considered as prototypes of devices that can mimic several aspects of the function of biological ion channels. We can employ the calculated transport diffusivities to estimate the steady state flux of water that can be expected through a thin film (Figure 6.9(a)) containing a substantial volume fraction of the aluminosilicate nanotubes embedded in a nonporous matrix (such as a polymer). The diffusive flux ( $J$ ) through a 15-nm and 100-nm thin membrane was calculated as follows<sup>215</sup>:

$$J = -\frac{1}{L} \int_{C_o}^{C_L} D_t(C) dC \cong -\frac{1}{L} \int_{\theta_o}^{\theta_L=0} D_s(0) \left( \frac{\partial \ln P}{\partial \ln \theta} \right) d\theta \quad (6.3)$$

Here  $L$  is the thickness of the membrane.  $C_o$  and  $C_L$  are the water vapor concentrations on the upstream and downstream side of the membrane, respectively. Figure 6.9(b) shows the predicted flux as a function of increasing  $C_o$  (expressed in terms of water partial pressure in mm Hg on the feed side of the membrane) with vacuum downstream ( $C_L = 0$ ). The relationship between partial pressure ( $P$ ) and water loading ( $\theta$ ) in the nanotube is obtained from the computed adsorption isotherm. The results (Figure 6.9(b)) demonstrate that very high water fluxes ( $10^2$ - $10^3$  mol/m<sup>2</sup>/s) can be obtained in the nanotubes even at very low pressure differentials of the order of 25 mm Hg (the saturation vapor pressure of water at room temperature). The observed inflection in water flux at low pressure differentials is due to the observed inflections in the GCMC isotherm (Figure 6.2(a)), which lead to peaks in the partial derivative of Eq. 6.2 that are ultimately reflected in the water flux predictions.

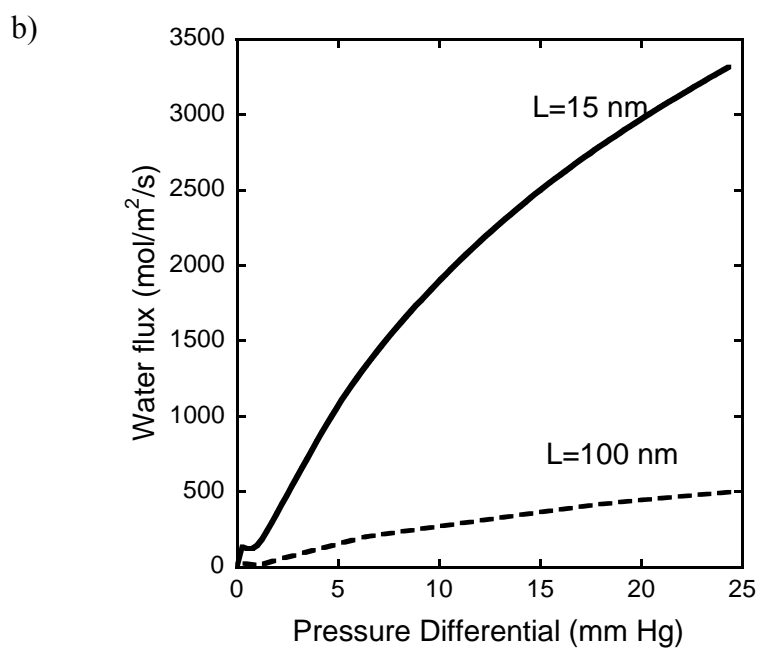
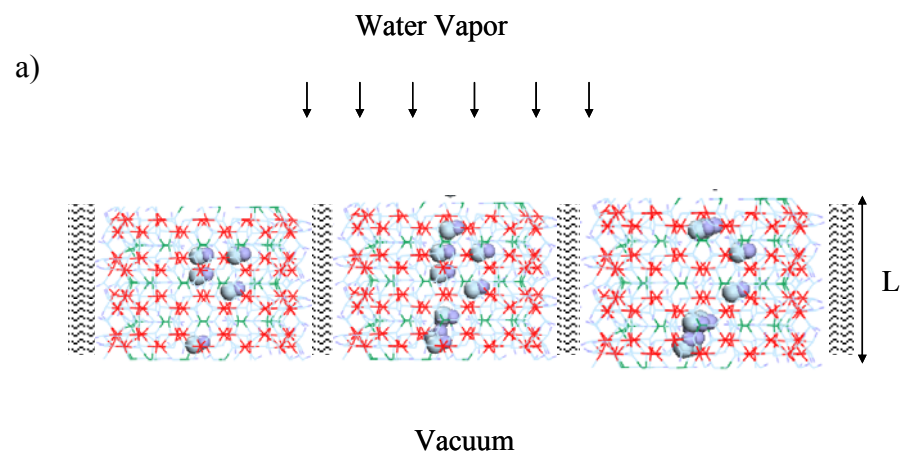


**Figure 6.9:** (a) Schematic of aligned aluminosilicate nanotube thin film with water transport driven by a vapor pressure differential across the membrane and with vacuum on the permeate side.  $L$  is the membrane thickness. (b) Predicted water flux through 15 nm and 100 nm thin nanotube membranes as a function of vapor pressure differential across the membrane.

To the best of our knowledge there has been no documented study of transport diffusivity of water in carbon nanotubes, hence, we make an approximate comparison between the water flux calculated in the present nanotube materials with that obtained in carbon nanotubes as measured recently <sup>89</sup>. In the present case, a water flux of  $\sim 10^3$  mol/m<sup>2</sup>/s was obtained in an aluminosilicate nanotube membrane containing a number density of  $\sim 1.7 \times 10^{13}$  nanotubes/cm<sup>2</sup> at a pressure differential of 25 mm Hg. On the other hand, the water flux measured through a carbon nanotube membrane with a number density of  $5 \times 10^{10}$  nanotubes/cm<sup>2</sup> was found to be two orders of magnitude lower ( $\sim 7$  mol/m<sup>2</sup>/s) at a pressure differential of 760 mm Hg. Further, the inner diameter ( $\sim 1$  nm) of the present nanotubes is much less than the inner diameter of the carbon nanotubes considered previously ( $\sim 7$  nm), so that the number density of the carbon nanotube membrane (assuming a diameter of 1 nm) is about  $2.5 \times 10^{12}$  nanotubes/cm<sup>2</sup>. Our predictions for water flux are conservative estimates, based on Fickian diffusivities calculated with periodic boundary conditions. However, external/interfacial resistances to mass transport were assumed to be negligible in all our calculations. A recent computational study on gas transport through sub-100-nm zeolite and carbon nanotube thin films suggested that surface resistances are significant for membrane thicknesses in the range considered in the present study <sup>215,216</sup>. For a nanoporous zeolite membrane with 15 nm thickness and a pressure differential of 760 mm Hg for CH<sub>4</sub> at 298 K, the transport resistance at the membrane interfaces was found to be approximately equal to the resistance within the membrane. On the other hand, the surface resistances for carbon nanotube membranes are significantly higher than the zeolite membranes for the same membrane thickness. It has been shown that for a carbon nanotube membrane with twice

the diameter as compared to aluminosilicate nanotube and a pressure differential of 5 bar for CH<sub>4</sub> at 300 K, the transport resistance at the membrane interfaces was approximately 10 times greater than the resistance within the membrane. Assuming that similar values for the surface resistance apply at the interfaces of the present nanotube membranes, we estimate that the resulting fluxes would at maximum be reduced by one order of magnitude of those shown in Figure 6.9(b). Most importantly, the water transport rates predicted through the nanotubes are very large and would no longer limit the throughput of the membrane. This is a combined effect of the characteristic short length of the present nanotubes (that can indeed be readily synthesized *via* aqueous-phase chemistry using relatively inexpensive Al, Si and Ge precursors<sup>87,88,204</sup>) as well as the hydrophilic nature of the material and the internal structure of the pore. Furthermore, detailed studies of the adsorption and transport properties of other molecules in the nanotubes, as well as their temperature and diameter-dependence, should yield a number of interesting results and are presently under investigation.

#### **6.4. Conclusions**

We have studied some essential aspects of the diffusion and adsorption properties of water in single-walled aluminosilicate nanotubes through a combination of molecular dynamics, monte carlo simulations and experimental sorption measurements. Sorption of water into the nanotubes predominantly occurs into the pores of the nanotubes with a large fraction of adsorption occurring at low pressures. The transport mechanism is governed by Fickian diffusion, with the resulting diffusivities being comparable to bulk water diffusivities and showing a loading dependence consistent with that observed in

other nanoporous materials rather than mesoporous materials. The structure of water in the nanotubes displays a loading-dependent transition from isolated to connected clusters of water molecules. Using the calculated self-diffusivities along with Darken's approximation and thermodynamic correction factors obtained from the adsorption data, we predict that high water fluxes can be attained in membranes fabricated from such nanotubes. The predicted fluxes are high due to a combination of short nanotube length, hydrophilic interior, as well as the near-bulk-water diffusivity in the nanotube. The water flux values may further be enhanced by the onset of the ballistic transport regime in shorter nanotubes ( $\sim 15$  nm) that can also be synthesized readily. It is proposed that the present nanotube materials are attractive candidates for the construction of nanocomposite films with polymers to form highly selective, high-throughput membranes.

## CHAPTER 7

### CONCLUSIONS AND FUTURE RESEARCH DIRECTIONS

#### 7.1. Conclusions

A detailed understanding of the structure-property relationships and an ability to control the dimensions of nanomaterials are required for a rational design of functional nanodevices and nanostructured assemblies using nanomaterials. In this thesis, we established that molecular simulations are very useful to obtain qualitative as well as quantitative information on the factors influencing dimension control in nanotubes, and molecular transport mechanism in relation to the structure of porous nanomaterials. Firstly, we employed molecular dynamics simulations to study gas transport properties of polymer/porous inorganic layered nanocomposite materials. The study has shown that transport in nanocomposite membranes can be controlled by several quantifiable factors such as the inorganic content, the molecular sieving ability of the layer, the transport properties of the polymeric material, and the microstructure of the membrane. For example, in the case of penetrants like He and H<sub>2</sub> which diffuse fast in PDMS, the molecular sieving properties of the inorganic material AMH-3 allow a considerable increase in selectivity (with respect to slower molecules like N<sub>2</sub> and O<sub>2</sub>) as a function of loading. In the case of penetrant pairs such as N<sub>2</sub> and O<sub>2</sub> which diffuse more slowly through PDMS and also cannot be efficiently separated by the AMH-3 layer, the nanocomposite membrane does not offer an increase in selectivity in comparison to pure PDMS. At higher inorganic loadings, the transport properties are affected by rigidification of the polymer chains due to strong confinement between the layers. By

careful choice of the polymeric and functional inorganic materials, the transport properties of the nanocomposite membranes can be tailored to attain superior permselectivity properties. Molecular dynamics simulations of nanocomposite membranes can provide valuable guidance by predicting the performance of candidate systems as a function of the structural and compositional factors that influence transport properties. Such predictions can be used to direct synthesis efforts toward suitable nanocomposite materials among the increasing number of potential nanoporous layered material/polymer combinations.

Next, we developed robust force field parameters for simulating layered aluminophosphates for use as functional inorganic layers in constructing nanocomposite membrane materials. The force field is based on the nonbond functional of the PCFF force field, and contains 9-6 Lennard Jones potential combined with the coulomb electrostatic potential, to allow direct incorporation of the force field parameters into the existing PCFF parameter database. The force field parameters derived based on the crystal structures of 2D layered AIPO-triethylamine, AIPO-2-methylpiperazine, and AIPO-triethylenetetramine successfully describe the structures of a broad range of 2D and 1D layered AIPOs. In addition, the developed parameters work well in conjunction with the PCFF parameters for the organic molecules (as understood from the comparison of computed and experimental infrared vibrational spectra) to correctly reproduce the hydrogen-bonding phenomenon between the AIPO layer and the organic cation amine template molecules. The current force field is specialized to layered AIPO materials with a 0.75 Al/P stoichiometry and can potentially be used to simulate dynamical properties

such as diffusion of small molecules, or the interfacial structures of hybrid materials containing layered AIPOs.

We then outlined the Transition State Approach-Monte Carlo technique for improving the computational times on calculation of gas transport properties in polymer/porous inorganic layered nanocomposites. We set the initial stage for developing the simulation methodology to perform the first calculations of gas transport properties in nanocomposite membrane materials. In a parallel study, we investigated the dimension control phenomenon of single-walled metal oxide nanotubes by examining the energetics of the nanotube as a function of its diameter. The observed monodispersity in diameter of the nanotubes is due to a difference in interatomic bond energies between the octahedral (Al-O) and tetrahedral (Si-O and/or Ge-O) bonds on the outer and inner surface of the nanotube, respectively, resulting in the occurrence of a substantial energy minimum with respect to the diameter. Furthermore, the energy minimum can be shifted to different diameters by changing the ratios of the two tetrahedrally coordinated elements (Si and Ge). We also developed an analytical model that relates the composition of the material to the nanotube energy and provides diameter predictions that can be used as guidelines for tuning nanotube dimensions *via* appropriate selection of the octahedral/tetrahedral species combinations.

Finally, we studied the diffusion and adsorption properties of water in single-walled aluminosilicate nanotubes through a combination of molecular dynamics, monte carlo simulations and experimental sorption measurements. The interior of these nanotubes

was found to be quite hydrophilic with a large fraction of adsorption of water molecules occurring into the pores of the nanotubes at low pressures. The unique periodic wide and narrow regions of the nanopore result in a loading-dependent structure transition from isolated to connected clusters of water molecules. The transport mechanism is governed by Fickian diffusion, with the resulting diffusivities being comparable to bulk water diffusivities. Using the calculated self-diffusivities and thermodynamic correction factors obtained from the adsorption data, we predict that high water fluxes ( $10^2$ - $10^3$  mol m<sup>-2</sup>s<sup>-1</sup> at 24 mm Hg pressure differential) can be attained in membranes fabricated from such nanotubes. The predicted fluxes are high due to a combination of short nanotube length, hydrophilic interior, as well as the near-bulk-water diffusivity in the nanotube, and can be used as guidelines for the construction of nanofluidic devices such as nanocomposite films with polymers to form highly selective, high-throughput membranes.

Overall, this research represents two examples of the progress in developing a predictive basis for the design and analysis of nanostructures. The simulation procedures established in this thesis, the insights attained on the molecular mechanism of observed macroscopic properties, and the predictions of transport properties impact the new science and technology of porous nanomaterials and nanodevices constructed with porous nanomaterials.

I conclude this thesis by presenting some future directions that are in line with the studies presented here. These studies, upon successful completion, would significantly

further the ongoing efforts in understanding the properties of porous nanomaterials and enabling their use in various technological applications.

## **7.2. Future Research Directions**

### **7.2.1. Nanocomposite Membrane Materials with Layered Aluminophosphate**

In this thesis, we have shown that enhanced gas separation performance of the polymer/porous inorganic layered nanocomposite materials is influenced by the molecular sieving ability of the inorganic layer among other factors. In addition to layered silicate AMH-3, porous layered aluminophosphates, such as those investigated in Chapter 3 of this thesis, have been identified as potential inorganic materials for constructing nanocomposite membrane materials<sup>42</sup>. These inorganic layers are 2-D porous sheet like structures as opposed to 3-D porous slab like structure of AMH-3. Hence, there will not be any penetrant diffusion within the inorganic layer (as was observed for AMH-3), which may lead to different molecular selectivity as well as permeability values compared to nanocomposites with AMH-3. Further, the layered AlPOs can be synthesized with varying pore network and dimensions that facilitates construction of nanocomposite materials tailored for a desired application. For example, layered AlPO-triethylamine contains 8 MRs ( $4.44 \times 3.29 \times 3.17 \text{ \AA}$ ) with smaller pore sizes compared to the 8 MRs of AMH-3 ( $4.24 \times 4.10 \times 3.40 \text{ \AA}$ ) that may be desirable for separations involving  $\text{O}_2/\text{N}_2$  or  $\text{CO}_2/\text{CH}_4$ .

A systematic investigation of gas transport properties with varying porous inorganic materials in the nanocomposite can provide detailed understanding on the transport phenomena of these materials and is important for practically realizing the application of these materials as gas separation devices in membrane technology. The layered AIPO force field developed in this thesis coupled with the simulation methodologies developed and proposed here can be directly employed to provide useful predictions of the gas separation performance of these nanocomposite membrane materials.

### **7.2.2. Gas Transport in Polymer/Porous Inorganic Layered Nanocomposite Materials**

In Chapter 4, we suggested the possibility of extending the Monte Carlo-Transition State Approach for calculating the diffusion of gas molecules in nanocomposite membrane materials. We presented preliminary work on diffusivity calculation of monoatomic gases in rigid membrane materials. The algorithms developed in this study can be extended to diffusivity calculations of polyatomic molecules by incorporating rotational motion of penetrant molecules in the solute distribution function. In such a case, the penetrant-matrix interactions will be a summation of interactions at varying spatial orientations of the penetrant molecules at each grid point. Further, the elastic motion of the host matrix atoms can also be incorporated in the solute distribution function (given by E.q. 4.1) for a more accurate estimation of the gas diffusivities. Development of such a simulation technique will provide a framework for predicting the transport properties of a variety of nanocomposite materials. The knowledge from such

studies can be directly employed towards synthesizing desired robust, economical nanocomposite membrane materials.

### **7.2.3. Molecular Transport in Single-Walled Metal-Oxide Nanotubes**

#### 7.2.3.1. Alcohol and Water/Alcohol Mixture Transport in Aluminosilicate Nanotubes

Single-walled metal-oxide nanotubes are unique candidates for application in nanofluidic devices as they present a well-defined solid-state structure, precisely tunable length and diameter, as well as a hydrophilic and functionalizable interior for tuning transport and adsorption selectivity. Our study on water transport in single-walled aluminosilicate nanotubes has demonstrated high water fluxes due to fast Fickian diffusivity of water molecules that can facilitate their application as high-throughput nanofluidic devices. To enable other potential applications such as molecule sensors, separation devices, energy storage devices etc., an understanding on selective transport mechanism of molecules in these nanotubes is required. Studying the adsorption and diffusion of less polar molecules such as methanol and ethanol as well as water/methanol and water/ethanol mixtures can provide an insight on the influence of liquid-liquid and liquid-surface interactions, effects of competitive transport on the fluid transport properties which can then be used to elucidate the overall transport mechanism of molecules in these nanotubes. In addition, the dependence of adsorption and diffusion properties on the nanotube diameter, a factor for tuning the transport properties of the nanotubes, can also be estimated by comparing the performance of AlGe or AlGeSiOH nanotubes that have larger diameters than the AlSi nanotubes. The mentioned studies can

be readily performed following the MD and MC simulation procedures established in this thesis. The force field parameters for the alcohol molecules can be adopted from PCFF force field that is well parameterized for organic molecules.

#### 7.2.3.2. Transport in Functionalized Nanotubes

The inner and outer surfaces of the present nanotubes can potentially be functionalized with organic groups (e.g. methyl, ethylammonium) due to the presence of hydroxyl bonds. Functionalization on the inner surface can potentially alter the adsorption and diffusion properties of the nanotubes by influencing molecule-nanopore interactions as well as by introducing steric effects. The simulation procedures established in this thesis as well as organic molecule force field parameters from PCFF can be employed to investigate the effects of functionalization on nanotube transport properties. Further, the predictions from these studies can be compared to experimental measurements as the nanotubes can potentially be synthesized with functionalized silicate or germanate precursors to form nanotubes with functionalized nanopores.

## APPENDIX A

### PCFF FORCE FIELD EXPRESSION AND PARAMETERS

PCFF parameters used for simulating diffusion of inorganic gases in PDMS/AMH-3 nanocomposite membrane materials.

The van der Waals interactions are described by a 9-6 potential as;

$$E = \sum_{i>j} \varepsilon_{ij} \left[ 2 \left( \frac{r_{ij}^*}{r_{ij}} \right)^9 - 3 \left( \frac{r_{ij}^*}{r_{ij}} \right)^6 \right]$$

Where  $r_{ij}^* = \left( \frac{r_i^6 + r_j^6}{2} \right)^{(1/6)}$  and  $\varepsilon_{ij} = 2\sqrt{\varepsilon_i \varepsilon_j} \left( \frac{r_i^3 r_j^3}{r_i^6 + r_j^6} \right)$

The coulombic interactions are given as;

$$E = \sum_{i>j} \frac{q_i q_j}{\varepsilon_o r_{ij}}$$

**Table A.1:** PCFF force field parameters

#### Nonbond Parameters for PCFF Force field

Species	Partial Charge (e)	$\varepsilon$ (kcal/mol)	r (Å)
Hydrogen bonded to C in methyl group (hc)	0.053	0.020	2.9950
Hydrogen bonded to terminal O in PDMS (ho)	0.340	0.013	1.0980
Hydrogen bonded to terminal Si in PDMS (hsi)	-0.13	0.0230	2.940
Carbon in methyl group (c3)		0.054	4.010
Backbone silicone atom in PDMS (sio)	0.640*	0.070	4.284
Backbone oxygen atom in PDMS (osi)	-0.44*	0.240	3.35
Hydroxyl hydrogen in AMH-3 (hos)	0.064	0.09880	2.3541
Hydroxyl oxygen in AMH-3 (osh)	-0.194	0.1591	3.4618
Bridging oxygen between two Si atoms	-0.262	0.1622	3.4506

in AMH-3 (oss)			
Tetrahedral Silicon in AMH-3 (sz)	0.524	0.0001	0.0
Hydrogen bonded to H (h)	0.0	0.020	2.9950
Oxygen bonded to O in double bond (o=)	0.0	0.060	3.5350
Nitrogen bonded to N in triple bond (nz)	0.0	0.065	3.570
He atom (he)	0.0	0.0203	2.900

\* Si bonded to hsi atom has a charge of 0.55

\* O bonded to ho atom has a charge of -0.56

#### Bonded Parameters for PCFF Force field

$$\text{Bond } E = K_2(r - r_0)^2 + K_3(r - r_0)^3 + K_4(r - r_0)^4$$

i	j	$K_2(\text{kcal/mol } \text{\AA}^2)$	$K_3(\text{kcal/mol } \text{\AA}^3)$	$K_4(\text{kcal/mol } \text{\AA}^4)$	$r_0(\text{\AA})$
c3	hc	345.0	-691.890	844.60	1.1010
c3	sio	157.0049	-237.7023	356.0328	1.9073
hsi	sio	187.1010	-280.7306	258.8998	1.4802
ho	osi	540.3633	-1311.8663	2132.4446	0.9494
osi	sio	306.1232	-517.3424	673.7067	1.6562
hos	osh	702.8730	-1531.8700	1814.8300	0.9457
oss	sz	325.4430	-943.3640	1454.6700	1.6155
osh	sz	420.0240	-845.6110	1438.6300	1.6125
h	h	414.0	0.0	0.0	0.7414
nz	nz	1652.40	0.0	0.0	1.0977
o=	o=	847.44	0.0	0.0	1.2074

$$\text{Angle } E = K_2(\theta - \theta_0)^2 + K_3(\theta - \theta_0)^3 + K_4(\theta - \theta_0)^4$$

i	j	k	$K_2(\text{kcal/mol rad}^2)$	$K_3(\text{kcal/mol rad}^3)$	$K_4(\text{kcal/mol rad}^4)$	$\theta_0(\text{rad})$
hc	c3	hc	39.6410	-12.9210	-2.4318	107.660
hc	c3	sio	30.2481	-15.5255	0.0	111.536
ho	osi	sio	23.7764	-19.8152	9.6331	122.888
hsi	sio	osi	57.6643	-10.6506	4.6274	107.355
c3	sio	c3	23.0218	-31.3993	24.9814	114.906
sio	osi	sio	9.0740	-19.5576	8.500	157.026
c3	sio	hsi	38.5645	-17.8735	0.0	110.181
c3	sio	osi	23.0218	-31.3993	24.9814	114.906
osi	sio	osi	70.3069	-6.9375	0.0	110.693
hos	osh	sz	14.8634	-17.2643	57.7495	123.492
sz	oss	sz	18.8146	37.9749	42.8222	176.265
osh	sz	osh	68.3381	49.4314	116.240	115.031
osh	sz	oss	117.506	-49.8921	0.0	110.670
oss	sz	oss	154.1860	-68.6595	23.6292	110.612

$$\text{Torsion } E = V_1 [1 - \cos(\varphi - \varphi_1^\circ)] + V_2 [1 - \cos(2\varphi - \varphi_2^\circ)] + V_3 [1 - \cos(3\varphi - \varphi_3^\circ)]$$

i	j	k	l	V <sub>1</sub> (kcal/mol)	Φ <sub>1</sub>	V <sub>2</sub> (kcal/mol)	Φ <sub>2</sub>	V <sub>3</sub> (kcal/mol)	Φ <sub>2</sub>
hc	c3	sio	c3	-1.3513	0.0	0.00	0.0	-0.0580	0.0
hc	c3	sio	hsi	-0.9301	0.0	0.00	0.0	-0.1259	0.0
hc	c3	sio	osi	-1.3513	0.0	0.00	0.0	-0.0580	0.0
ho	osi	sio	c3	-0.6741	0.0	0.3661	0.0	-0.1008	0.0
ho	osi	sio	hsi	-0.7720	0.0	0.9364	0.0	-0.1169	0.0
sio	osi	sio	c3	0.00	0.0	0.00	0.0	-0.1300	0.0
ho	osi	sio	osi	-0.6741	0.0	0.3661	0.0	-0.1008	0.0
sio	osi	sio	hsi	0.00	0.0	0.00	0.0	-0.1300	0.0
sio	osi	sio	osi	0.300	0.0	0.3658	0.0	0.00	0.0
hos	osh	sz	osh	0.4267	0.0	0.1147	0.0	0.0390	0.0
hos	osh	sz	oss	2.3777	0.0	-0.0069	0.0	-0.5244	0.0
sz	oss	sz	osh	-0.2403	0.0	0.1673	0.0	0.0002	0.0
sz	oss	sz	oss	-0.3417	0.0	0.0961	0.0	0.1683	0.0

$$\text{Bond-Bond } E = K_{i,j,k} (r - r_0) (r' - r_0')$$

i	j	k	K <sub>i,j,k</sub> (kcal/mol Å <sup>2</sup> )
hc	c3	hc	5.3316
hc	c3	sio	6.3820
ho	osi	sio	6.3820
hsi	sio	osi	11.6183
c3	sio	c3	5.4896
sio	osi	sio	41.1143
c3	sio	hsi	4.6016
c3	sio	osi	5.4896
osi	sio	osi	41.1143
hos	osh	sz	8.8125
sz	oss	sz	178.8840
osh	sz	osh	72.1792
osh	sz	oss	25.1384
oss	sz	oss	178.8840

$$\text{Bond-Angle } E = K(r - r_0) (\theta - \theta_0)$$

i	j	k	K <sub>i,j,i-k</sub> (kcal/mol Å rad)	K <sub>j-k,i-j-k</sub> (kcal/mol Å rad)
hc	c3	hc	18.1030	
hc	c3	sio	14.7189	12.8694
ho	osi	sio	18.0902	31.0726
hsi	sio	osi	6.4278	20.5669
c3	sio	c3	4.0414	
sio	osi	sio	28.6686	

c3	sio	hsi	3.3072	7.8353
c3	sio	osi	6.4278	20.5669
osi	sio	osi	23.4380	
hos	osh	sz	25.8526	52.9983
sz	oss	sz	13.4905	
osh	sz	osh	69.9792	
osh	sz	oss	109.4210	62.4913
oss	sz	oss	87.3528	

**Angle-Angle**  $E = K (\theta - \theta_0) (\theta' - \theta_0')$

<b>i</b>	<b>j</b>	<b>k</b>	<b>l</b>	<b>K(kcal/mol rad<sup>2</sup>)</b>
osh	sz	osh	osh	33.2746
osh	sz	osh	oss	58.9474
oss	sz	osh	oss	107.4240
osh	sz	oss	osh	72.4464
osh	sz	oss	oss	116.6570
oss	sz	oss	oss	9.0179

**Angle-Angle-Torsion**  $E = K (\theta - \theta_0) (\theta' - \theta_0') (\varphi - \varphi_1^0)$

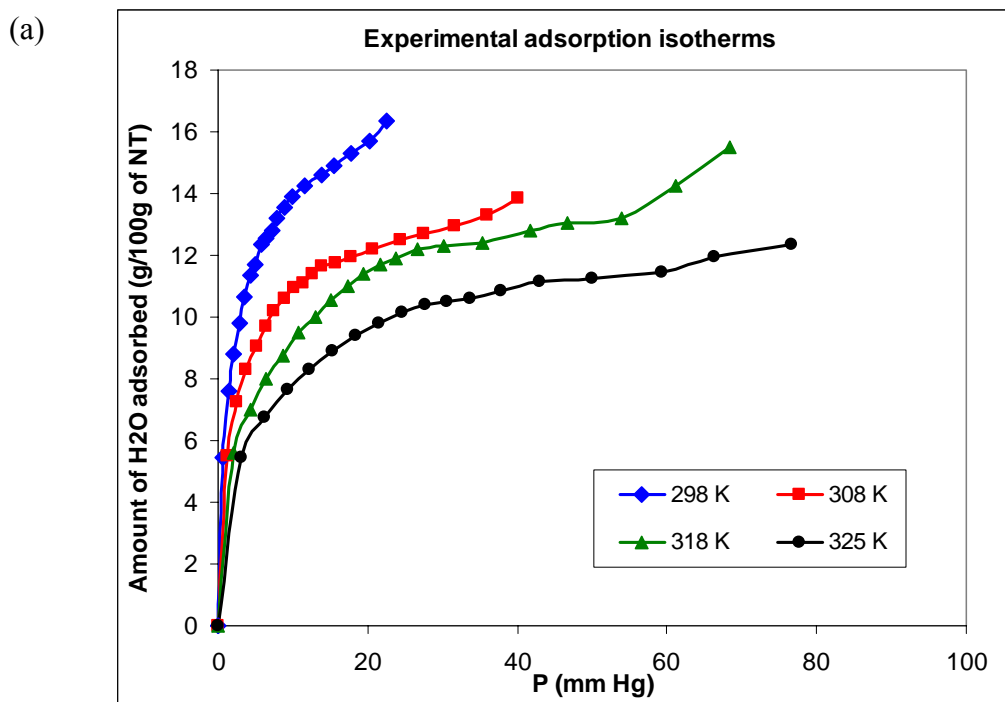
<b>i</b>	<b>j</b>	<b>k</b>	<b>l</b>	<b>K(kcal/mol rad<sup>2</sup>)</b>
hos	osh	sz	osh	5.0402
hos	osh	sz	oss	0.00
sz	oss	sz	osh	4.3761
sz	oss	sz	oss	5.7889

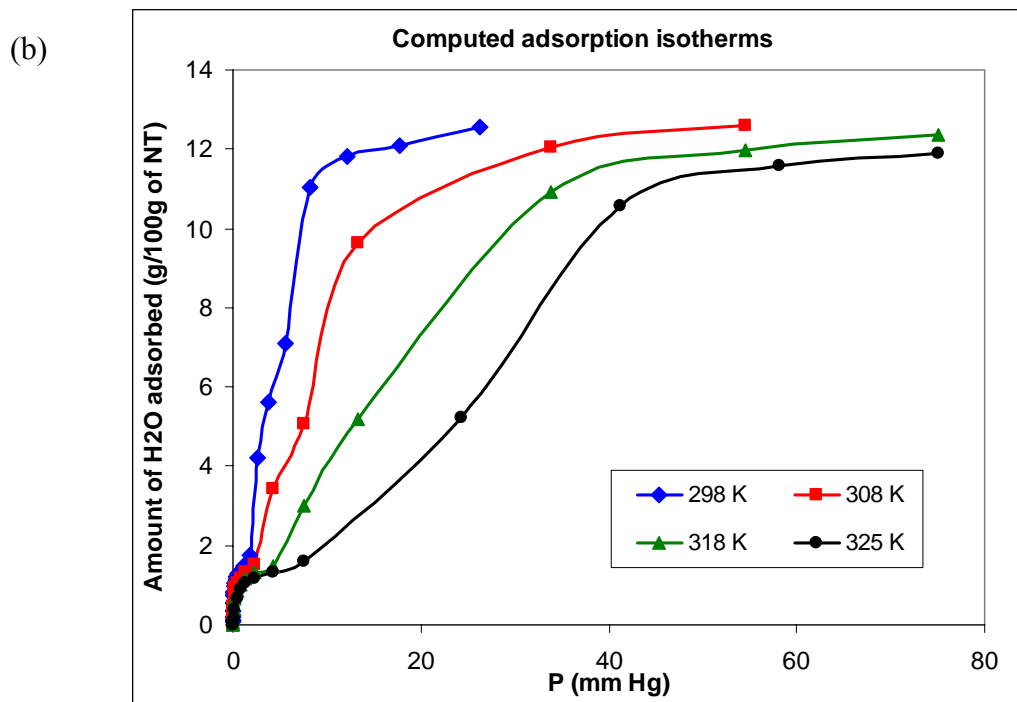
## APPENDIX B

### WATER ADSORPTION AND STRUCTURE IN SINGLE-WALLED ALUMINOSILICATE NANOTUBES

#### B.1. Water Adsorption Isotherms in Aluminosilicate Nanotubes

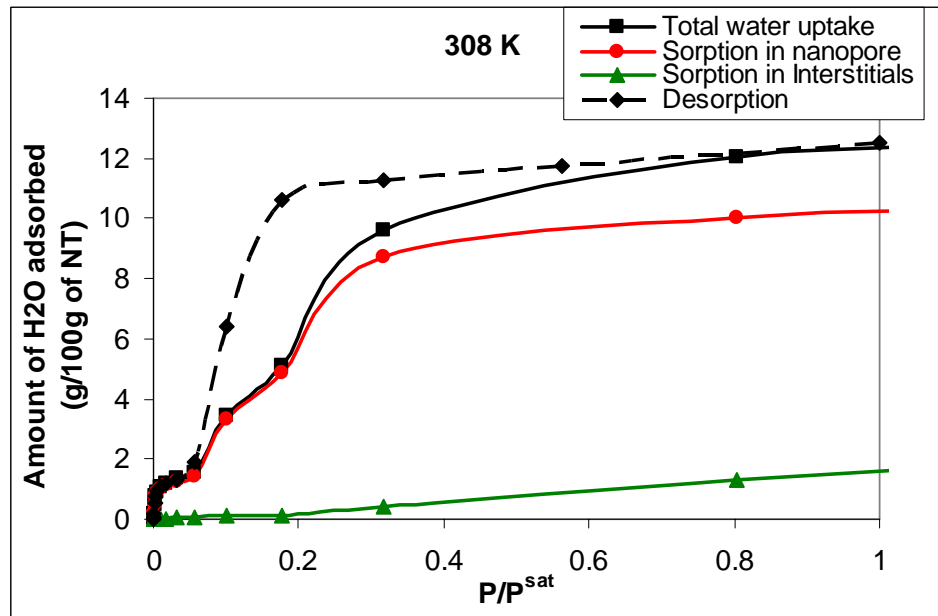
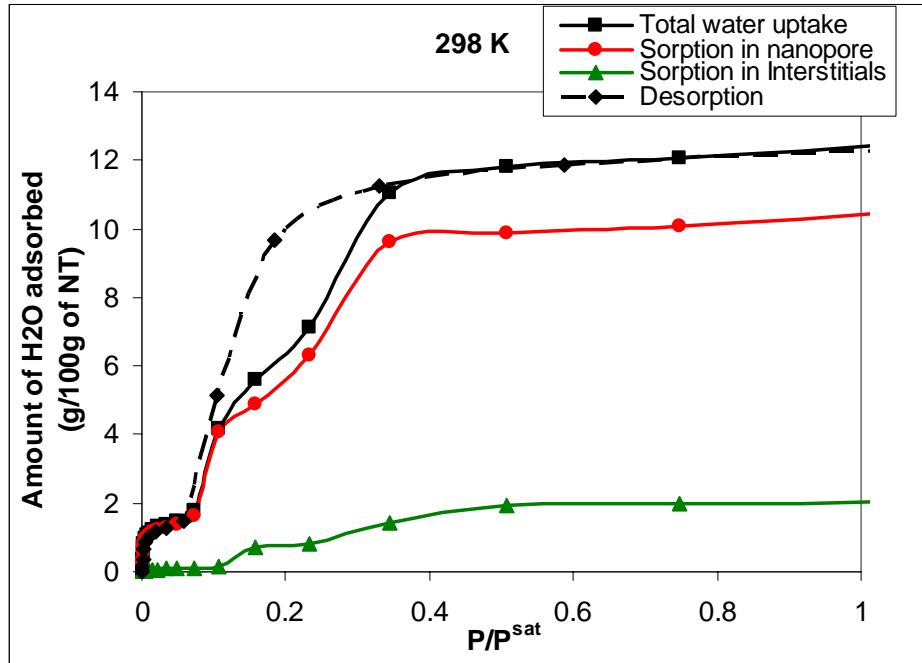
Figure B.1 (a)-(b) shows the measured and computed adsorption isotherms of water vapor in aluminosilicate nanotubes as a function of temperature. In Figure 6.2(a)-(b) of Chapter 6, the apparent “crossover” of isotherms at temperatures of 318 K and 308 K in the experimental isotherms, and at temperatures of 325 K and 298 K in computed isotherms, is introduced when the data are all normalized to a single relative humidity (RH) scale using saturation vapor pressures (which depend on temperature).





**Figure B.1:** (a) Measured adsorption isotherms showing amount of water adsorbed in single-walled aluminosilicate nanotube as a function of partial pressure at the same temperatures. (b) Computed adsorption isotherms of water adsorbed in single-walled aluminosilicate nanotube as a function of partial pressure at  $T = 298$  (Blue),  $308$  (Red),  $318$  (green), and  $325$  K (black).

We calculated the site-specific adsorption of water molecules in the aluminosilicate nanotubes and compare the contribution of different adsorption sites to the total uptake of water molecules in the nanotubes. Figure B.2 shows the results of adsorption of water molecules in the nanopore and interstitial spaces between the nanotubes at different temperatures. Also shown in the figure are the desorption isotherms to demonstrate the hysteresis between adsorption and desorption of water in aluminosilicate nanotubes.



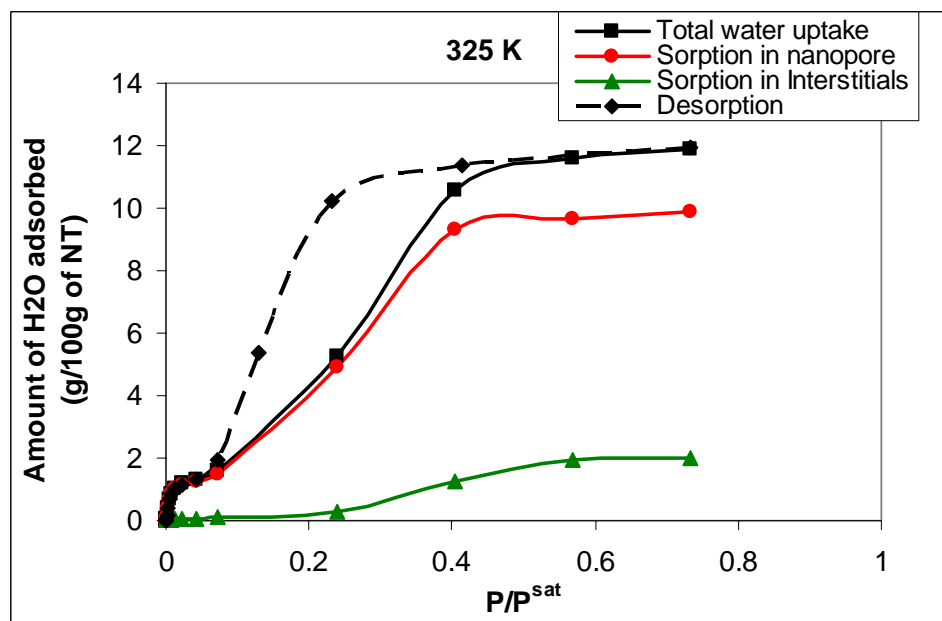
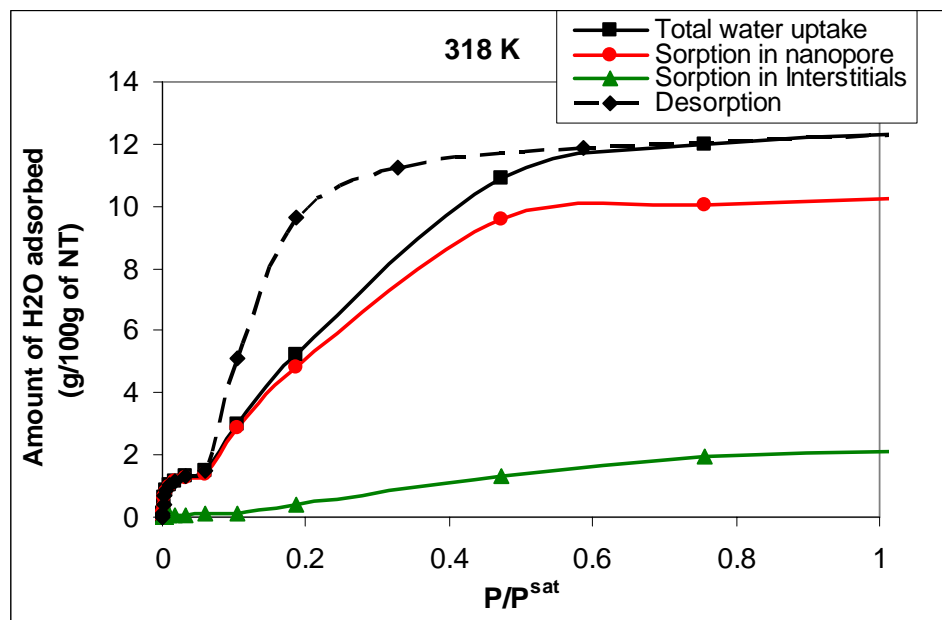


**Figure B.2:** Site-specific computed adsorption isotherms of water in single-walled aluminosilicate nanotubes. Solid black lines denote total uptake of water in the nanotubes. Dashed lines denote desorption. Solid red lines denote adsorption into the nanopores and solid green lines denote adsorption in the interstitial spaces.

## **B.2. Internal energy of adsorption**

We calculate the internal energy of adsorption of water vapor in aluminosilicate nanotubes by summing the water-nanotube and water-water interaction energies obtained from the GCMC trajectories. The internal energies were then averaged over all the four temperatures to obtain the sorption energy as a function of pressure, as shown in Figure B.3.

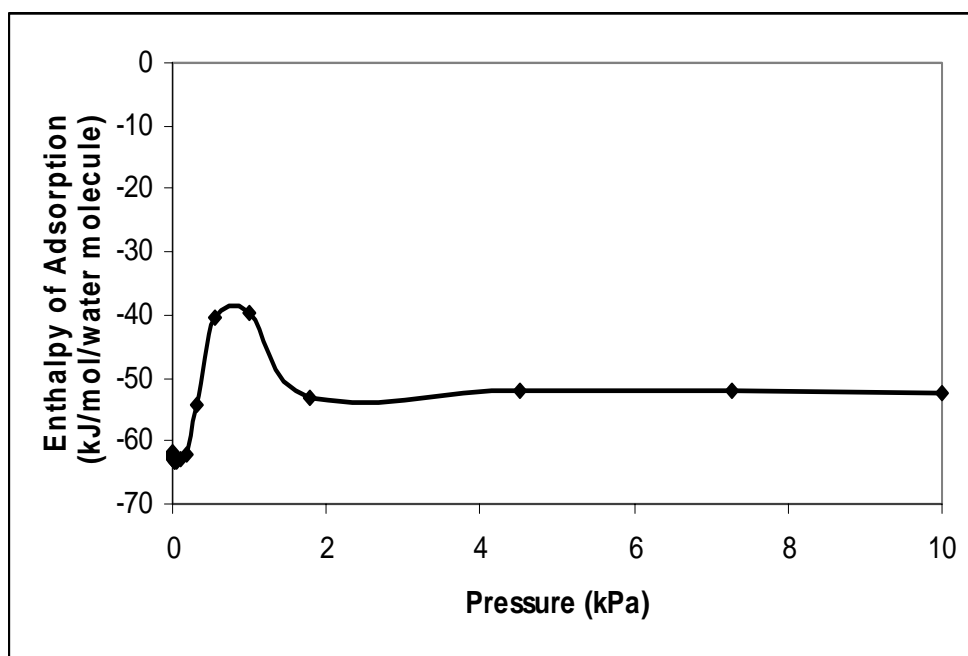


**Figure B.3:** Internal energy of adsorption of water molecules in the aluminosilicate nanotube as a function of pressure.

**B.3. O-O and O-H Pair correlation functions of water molecules in the aluminosilicate nanotube**

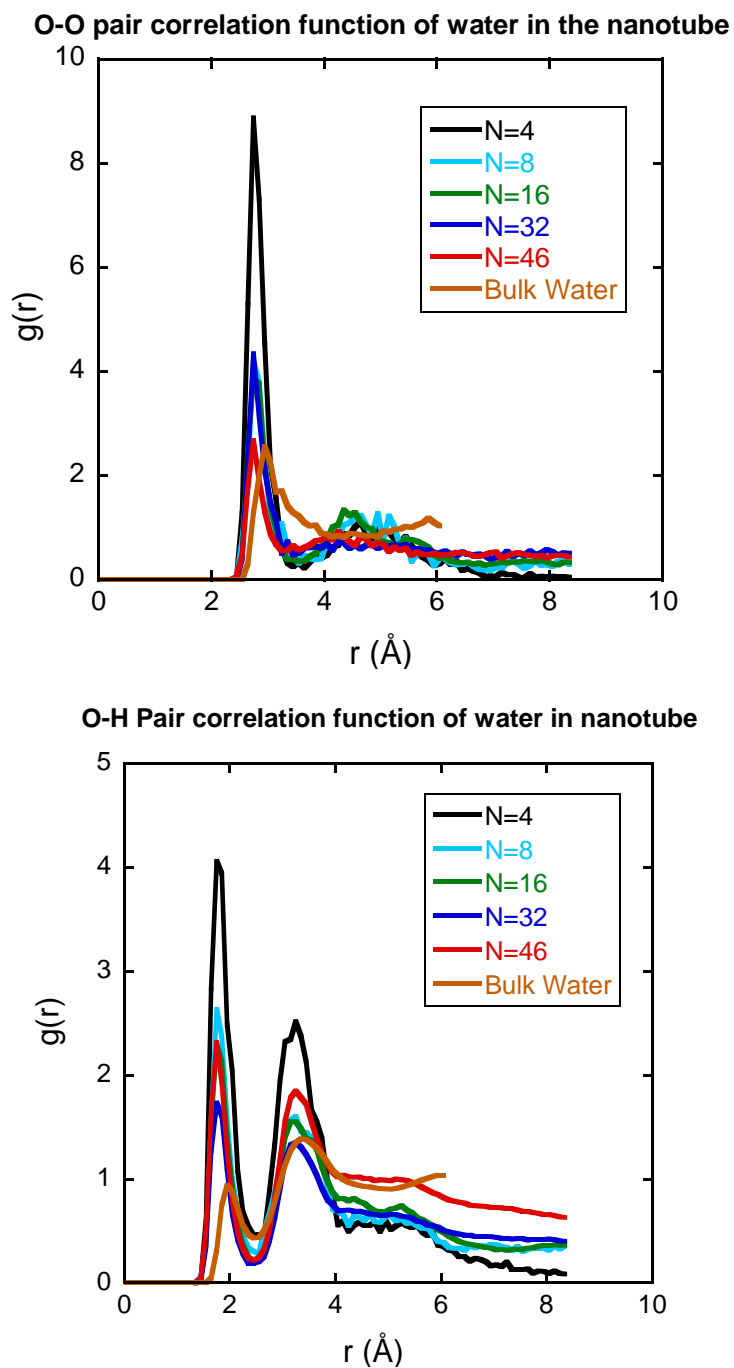


**Figure B.4:** O-O and O-H pair correlation functions of water molecules as a function of increasing water content in the nanotube. With increasing water content in the nanotube, the pair correlation functions for water molecules approximate the structure of bulk water.

## REFERENCES

1. Feynman, R. P. <http://www.zyvex.com/nanotech/feynman.html>. (1959).
2. Loo, C.; Lowery, A.; Halas, N.; West, J.; Drezek, R. *Nano Letters*. 5, 709-711, (2005).
3. Avouris, P. *Chemical Physics*. 281, 429-445, (2002).
4. de Heer, W. A.; Chatelain, A.; Ugarte, D. *Science*. 270, 1179-1180, (1995).
5. Zuttel, A.; Sudan, P.; Mauron, P.; Kiyobayashi, T.; Emmenegger, C.; Schlapbach, L. *International Journal of Hydrogen Energy*. 27, 203-212, (2002).
6. Lewis, N. S. *Science*. 315, 798-801, (2007).
7. Moraru, C. I.; Panchapakesan, C. P.; Huang, Q. R.; Takhistov, P.; Liu, S.; Kokini, J. L. *Food Technology*. 57, 24-29, (2003).
8. Sanguansri, P.; Augustin, M. A. *Trends in Food Science & Technology*. 17, 547-556, (2006).
9. Rogale, D.; Dragcevic, Z., 107-121, (2001).
10. Yuen, C. W. M.; Li, Y.; Ku, S. K.; Mak, C. M.; Kan, C. W. *Aatcc Review*. 5, 41-45, (2005).
11. El-Sayed, M. A. *Accounts of Chemical Research*. 34, 257-264, (2001).
12. Trindade, T.; O'Brien, P.; Pickett, N. L. *Chemistry of Materials*. 13, 3843-3858, (2001).
13. Sun, J.; Simon, S. L. *Thermochimica Acta*. 463, 32-40, (2007).
14. Haruta, M.; Date, M. *Applied Catalysis a-General*. 222, 427-437, (2001).
15. Kelly, K. L.; Coronado, E.; Zhao, L. L.; Schatz, G. C. *Journal of Physical Chemistry B*. 107, 668-677, (2003).
16. Allaoui, A.; Bai, S.; Cheng, H. M.; Bai, J. B. *Composites Science and Technology*. 62, 1993-1998, (2002).
17. Balasubramanian, K.; Burghard, M. *Analytical and Bioanalytical Chemistry*. 385, 452-468, (2006).
18. Baughman, R. H.; Zakhidov, A. A.; de Heer, W. A. *Science*. 297, 787-792, (2002).
19. Dresselhaus, M. S.; Dai, H. *Mrs Bulletin*. 29, 237-239, (2004).

20. Niu, C. M.; Sichel, E. K.; Hoch, R.; Moy, D.; Tennent, H. *Applied Physics Letters*. 70, 1480-1482, (1997).
21. Arico, A. S.; Bruce, P.; Scrosati, B.; Tarascon, J. M.; Van Schalkwijk, W. *Nature Materials*. 4, 366-377, (2005).
22. Klostranec, J. M.; Chan, W. C. W. *Advanced Materials*. 18, 1953-1964, (2006).
23. Drexler, K. E. *Proceedings of the National Academy of Sciences of the United States of America-Physical Sciences*. 78, 5275-5278, (1981).
24. Niemeyer, C. M. *Applied Physics a-Materials Science & Processing*. 68, 119-124, (1999).
25. Koga, K.; Gao, G. T.; Tanaka, H.; Zeng, X. C. *Nature*. 412, 802-805, (2001).
26. Stallmach, F.; Karger, J.; Krause, C.; Jeschke, M.; Oberhagemann, U. *Journal of the American Chemical Society*. 122, 9237-9242, (2000).
27. Gorring, R. L. *Journal of Catalysis*. 31, 13-26, (1973).
28. Hummer, G.; Rasaiah, J. C.; Noworyta, J. P. *Nature*. 414, 188-190, (2001).
29. Malek, K.; Coppens, M. O. *Journal of Chemical Physics*. 119, 2801-2811, (2003).
30. Demontis, P.; Stara, G.; Suffritti, G. B. *Journal of Physical Chemistry B*. 107, 4426-4436, (2003).
31. Adhangale, P.; Keffer, D. *Separation Science and Technology*. 38, 977-998, (2003).
32. Kojima, Y.; Usuki, A.; Kawasumi, M.; Okada, A.; Fukushima, Y.; Kurauchi, T.; Kamigaito, O. *Journal of Materials Research*. 8, 1185-1189, (1993).
33. Kojima, Y.; Usuki, A.; Kawasumi, M.; Okada, A.; Kurauchi, T.; Kamigaito, O. *Journal of Polymer Science Part A-Polymer Chemistry*. 31, 983-986, (1993).
34. Kojima, Y.; Usuki, A.; Kawasumi, M.; Okada, A.; Kurauchi, T.; Kamigaito, O. *Journal of Polymer Science Part A-Polymer Chemistry*. 31, 1755-1758, (1993).
35. Giannelis, E. P. *Advanced Materials*. 8, 29-35, (1996).
36. Giannelis, E. P. *Applied Organometallic Chemistry*. 12, 675-680, (1998).
37. Gilman, J. W. *Applied Clay Science*. 15, 31-49, (1999).
38. Messersmith, P. B.; Giannelis, E. P. *Journal of Polymer Science Part A-Polymer Chemistry*. 33, 1047-1057, (1995).

39. Ray, S. S.; Okamoto, M. *Progress in Polymer Science*. 28, 1539-1641, (2003).
40. Yano, K.; Usuki, A.; Okada, A. *Journal of Polymer Science Part A: Polymer Chemistry*. 35, 2289-2294, (1997).
41. Alexandre, M.; Dubois, P. *Materials Science and Engineering*. 28, 1-63, (2000).
42. Jeong, H. K.; Krych, W.; Ramanan, H.; Nair, S.; Marand, E.; Tsapatsis, M. *Chemistry of Materials*. 16, 3838-3845, (2004).
43. Giannelis, E. P.; Krishnamoorti, R.; Manias, E. *Polymers in Confined Environments*. Vol. 138, 107-147. (1999).
44. Lan, T.; Kaviratna, P. D.; Pinnavaia, T. J. *Chemistry of Materials*. 7, 2144-2150, (1995).
45. Wang, Z.; Pinnavaia, T. J. *Chemistry of Materials*. 10, 1820-1826, (1998).
46. Messersmith, P. B.; Giannelis, E. P. *Chemistry of Materials*. 6, 1719-1725, (1994).
47. Choi, S.; Coronas, J.; Jordan, E.; Oh, W.; Nair, S.; Onorato, F.; Shantz, D. F.; Tsapatsis, M. *Angewandte Chemie-International Edition*. 47, 552-555, (2008).
48. Choi, S.; Coronas, J.; Sheffel, J. A.; Jordan, E.; Oh, W.; Nair, S.; Shantz, D. F.; Tsapatsis, M. *Microporous and Mesoporous Materials*. 115, 75-84, (2008).
49. Choi, S. H.; Coronas, J. Q.; Lai, Z. P.; Yust, D.; Onorato, F.; Tsapatsis, M. *Journal of Membrane Science*. 316, 145-152, (2008).
50. Shu, S.; Husain, S.; Koros, W. J. *Journal of Physical Chemistry C*. 111, 652-657, (2007).
51. Mahajan, R.; Koros, W. J. *Industrial & Engineering Chemistry Research*. 39, 2692-2696, (2000).
52. Yong, H. H.; Park, N. C.; Kang, Y. S.; Won, J.; Kim, W. N. *Journal of Membrane Science*. 188, 151-163, (2001).
53. Duval, J. M.; Kemperman, A. J. B.; Folkers, B.; Mulder, M. H. V.; Desgrandchamps, G.; Smolders, C. A. *Journal of Applied Polymer Science*. 54, 409-418, (1994).
54. Li, Y.; Guan, H. M.; Chung, T. S.; Kulprathipanja, S. *Journal of Membrane Science*. 275, 17-28, (2006).
55. Hillock, A. M. W.; Miller, S. J.; Koros, W. J. *Journal of Membrane Science*. 314, 193-199, (2008).
56. Stern, S. A.; Trohalaki, S. *ACS Symposium Series*. Vol. 423, 22-59. (1990).

57. Kumins, C. A.; Roteman, J. *Journal of Polymer Science*. 55, 699-707, (1961).
58. Vrentas, J. S.; Duda, J. L. *Journal of Polymer Science Part B-Polymer Physics*. 15, 403-416, (1977).
59. Freeman, B. D. *Macromolecules*. 32, 375-380, (1999).
60. Karger, J.; Ruthven, D. M. *Diffusion in Zeolites and Other Microporous Solids*. 87-122. (1992).
61. Moore, T. T.; Mahajan, R.; Vu, D. Q.; Koros, W. J. *Aiche Journal*. 50, 311-321, (2004).
62. Mahoney, D.; Vonmeerwall, E. *Journal of Polymer Science Part B-Polymer Physics*. 31, 1029-1039, (1993).
63. Michaels, A. S.; Parker, R. B. *Journal of Polymer Science*. 41, 53-71, (1959).
64. Michaels, A. S.; Barrie, J. A.; Vieth, W. R. *Journal of Applied Physics*. 34, 1-12, (1963).
65. Suer, M. G.; Bac, N.; Yilmaz, L. *Journal of Membrane Science*. 91, 77-86, (1994).
66. Husain, S.; Koros, W. J. *Journal of Membrane Science*. 288, 195-207, (2007).
67. Vu, D. Q.; Koros, W. J.; Miller, S. J. *Journal of Membrane Science*. 211, 311-334, (2003).
68. Mitchell, D. T.; Lee, S. B.; Trofin, L.; Li, N. C.; Nevanen, T. K.; Soderlund, H.; Martin, C. R. *Journal of the American Chemical Society*. 124, 11864-11865, (2002).
69. Kohli, P.; Wirtz, M.; Martin, C. R. *Electroanalysis*. 16, 9-18, (2004).
70. Martel, R.; Schmidt, T.; Shea, H. R.; Hertel, T.; Avouris, P. *Applied Physics Letters*. 73, 2447-2449, (1998).
71. Lee, S. M.; Lee, Y. H. *Applied Physics Letters*. 76, 2877-2879, (2000).
72. Muthukumar, M. *Journal of Chemical Physics*. 111, 10371-10374, (1999).
73. Chen, H. B.; Johnson, J. K.; Sholl, D. S. *Journal of Physical Chemistry B*. 110, 1971-1975, (2006).
74. Majumder, M.; Chopra, N.; Andrews, R.; Hinds, B. J. *Nature*. 438, 44-44, (2005).
75. Holt, J. K.; Park, H. G.; Wang, Y. M.; Stadermann, M.; Artyukhin, A. B.; Grigoriopoulos, C. P.; Noy, A.; Bakajin, O. *Science*. 312, 1034-1037, (2006).

76. Little, R. B. *Journal of Cluster Science*. 14, 135-185, (2003).
77. Bae, S. Y.; Seo, H. W.; Park, J. H. *Journal of Physical Chemistry B*. 108, 5206-5210, (2004).
78. Liu, S. M.; Gan, L. M.; Liu, L. H.; Zhang, W. D.; Zeng, H. C. *Chemistry of Materials*. 14, 1391-1397, (2002).
79. Pauling, L. *Proceedings of the National Academy of Sciences of the United States of America*. 16, 578-582, (1930).
80. Yoshinaga, N.; Aomine, S. *Soil Science & Plant Nutrition*. 8, 22-39, (1962).
81. Cradwick, P. D.; Wada, K.; Russell, J. D.; Yoshinaga, N.; Masson, C. R.; Farmer, V. C. *Nature-Physical Science*. 240, 187-189, (1972).
82. Russell, J. D.; McHardy, W. J.; Fraser, A. R. *Clay Minerals*. 8, 87-99, (1969).
83. Wada, K.; Yoshinaga, N. *American Mineralogist*. 54, 50-71, (1969).
84. Wada, S. I.; Eto, A.; Wada, K. *Journal of Soil Science*. 30, 347-355, (1979).
85. Wada, S.; Wada, K. *Clays and Clay Minerals*. 30, 123-128, (1982).
86. Mukherjee, S.; Bartlow, V. A.; Nair, S. *Chemistry of Materials*. 17, 4900-4909, (2005).
87. Mukherjee, S.; Kim, K.; Nair, S. *Journal of the American Chemical Society*. 129, 6820-6826, (2007).
88. Konduri, S.; Mukherjee, S.; Nair, S. *ACS Nano*. 1, 393-402, (2007).
89. Hinds, B. J.; Chopra, N.; Rantell, T.; Andrews, R.; Gavalas, V.; Bachas, L. G. *Science*. 303, 62-65, (2004).
90. Liu, C.; Fan, Y. Y.; Liu, M.; Cong, H. T.; Cheng, H. M.; Dresselhaus, M. S. *Science*. 286, 1127-1129, (1999).
91. Dillon, A. C.; Jones, K. M.; Bekkedahl, T. A.; Kiang, C. H.; Bethune, D. S.; Heben, M. J. *Nature*. 386, 377-379, (1997).
92. Ohashi, F.; Tomura, S.; Akaku, K.; Hayashi, S.; Wada, S. I. *Journal of Materials Science*. 39, 1799-1801, (2004).
93. Chen, H. B.; Sholl, D. S. *Journal of Membrane Science*. 269, 152-160, (2006).
94. Kalra, A.; Garde, S.; Hummer, G. *Proceedings of the National Academy of Sciences of the United States of America*. 100, 10175-10180, (2003).

95. Kolesnikov, A. I.; Zanotti, J. M.; Loong, C. K.; Thiyagarajan, P.; Moravsky, A. P.; Loutfy, R. O.; Burnham, C. J. *Physical Review Letters*. 93, 035503 (1-4), (2004).
96. Sholl, D. S.; Fichthorn, K. A. *Physical Review Letters*. 79, 3569-3572, (1997).
97. Skoulidas, A. I.; Sholl, D. S. *Journal of Physical Chemistry B*. 106, 5058-5067, (2002).
98. Skoulidas, A. I.; Ackerman, D. M.; Johnson, J. K.; Sholl, D. S. *Physical Review Letters*. 89, 185901-1-185901-4, (2002).
99. Klinke, C.; Bonard, J. M.; Kern, K. *Physical Review B*. 71, 035403 (1-7), (2005).
100. Robertson, D. H.; Brenner, D. W.; Mintmire, J. W. *Physical Review B*. 45, 12592-12595, (1992).
101. Mukherjee, S.; Bartlow, V.; Nair, S. *Chemistry of Materials*. 17, 4900-4909, (2006).
102. Kупpa, V.; Foley, T. M. D.; Manias, E. *European Physical Journal E*. 12, 159-165, (2003).
103. Kупpa, V.; Manias, E. *Chemistry of Materials*. 14, 2171-2175, (2002).
104. Coombes, D. S.; Catlow, C. R. A.; Garces, J. M. *Modelling and Simulation in Materials Science and Engineering*. 11, 301-306, (2003).
105. Sutton, R.; Sposito, G. *Journal of Colloid and Interface Science*. 237, 174-184, (2001).
106. Smith, J. S.; Bedrov, D.; Smith, G. D. *Composites Science and Technology*. 63, 1599-1605, (2003).
107. Hofmann, D.; Fritz, L.; Ulbrich, J.; Schepers, C.; Bohning, M. *Macromolecular Theory and Simulations*. 9, 293-327, (2000).
108. Liu, Y. C.; Wang, Q.; Wu, T.; Zhang, L. *Journal of Chemical Physics*. 123, (2005).
109. Skoulidas, A. I.; Sholl, D. S.; Johnson, J. K. *Journal of Chemical Physics*. 124, (2006).
110. Merkel, T. C.; Bondar, V. I.; Nagai, K.; Freeman, B. D.; Pinnau, I. *Journal of Polymer Science Part B-Polymer Physics*. 38, 415-434, (2000).
111. Bixler, H. J.; Sweeting, O. J. *The Science and Technology of Polymer Films*; Interscience Publishers: NY, Vol. 2, (1971).
112. Barrer, R. M.; Chio, H. T. *Journal of Polymer Science Part C-Polymer Symposium*. 111-138, (1965).

113. Jeong, H. K.; Nair, S.; Vogt, T.; Dickinson, L. C.; Tsapatsis, M. *Nature Materials*. 2, 53-58, (2003).
114. Sun, H. *Macromolecules*. 28, 701-712, (1995).
115. Sun, H.; Rigby, D. *Spectrochimica Acta Part A: Molecular and Biomolecular Spectroscopy*. 53, 1301-1323, (1997).
116. Hill, J. R.; Sauer, J. *Journal of Physical Chemistry*. 98, 1238-1244, (1994).
117. DiscoverForcefield *Versions 1.0 and 3.0*, Biosym Technologies Inc, (1995).
118. Meier, W. M.; Olson, D.; Baerlocher, C. *Atlas of zeolite structure types*; Elsevier: New York, Vol. 4th revised edition, (1996).
119. Theodorou, D. N.; Suter, U. W. *Macromolecules*. 18, 1467-1478, (1985).
120. Stern, S. A. *Journal of Membrane Science*. 94, 1-65, (1994).
121. Konduri, S.; Nair, S. *Journal of Physical Chemistry C*. 111, 2017-2024, (2007).
122. Muller-Plathe, F.; Rogers, S. C.; Vangunsteren, W. F. *Chemical Physics Letters*. 199, 237-243, (1992).
123. Torquato, S. *International Journal of Solids and Structures*. 37, 411-422, (2000).
124. Kim, H. S.; Hong, S. I.; Kim, S. J. *Journal of Materials Processing Technology*. 112, 109-113, (2001).
125. Charati, S. G.; Stern, S. A. *Macromolecules*. 31, 5529-5535, (1998).
126. Nagumo, R.; Takaba, H.; Suzuki, S.; Nakao, S. *Microporous and Mesoporous Materials*. 48, 247-254, (2001).
127. Skoulidas, A. I.; Ackerman, D. M.; Johnson, J. K.; Sholl, D. S. *Physical Review Letters*. 89, (2002).
128. Makrodimitris, K.; Papadopoulos, G. K.; Theodorou, D. N. *Journal of Physical Chemistry B*. 105, 777-788, (2001).
129. Chakravarty, C. *Journal of Physical Chemistry B*. 101, 1878-1883, (1997).
130. Buch, V. *Journal of Chemical Physics*. 100, 7610-7629, (1994).
131. Dunne, J. A.; Mariwals, R.; Rao, M.; Sircar, S.; Gorte, R. J.; Myers, A. L. *Langmuir*. 12, 5888-5895, (1996).
132. Freeman, B.; Pinnau, I. *Trends in Polymer Science*. 5, 167-173, (1997).

133. Cussler, E. L. *Journal of Membrane Science*. 52, 275-288, (1990).
134. Karger, J. *Journal of Physical Chemistry*. 95, 5558-5560, (1991).
135. June, R. L.; Bell, A. T.; Theodorou, D. N. *Journal of Physical Chemistry*. 94, 8232-8240, (1990).
136. Zax, D. B.; Yang, D. K.; Santos, R. A.; Hegemann, H.; Giannelis, E. P.; Manias, E. *Journal of Chemical Physics*. 112, 2945-2951, (2000).
137. Manias, E.; Kuppa, V. *European Physical Journal E*. 8, 193-199, (2002).
138. Thomas, J. M.; Raja, R.; Sankar, G.; Bell, R. G. *Accounts of Chemical Research*. 34, 191-200, (2001).
139. Jhung, S. H.; Kim, H. K.; Yoon, J. W.; Chang, J. S. *Journal of Physical Chemistry B*. 110, 9371-9374, (2006).
140. Yan, W. F.; Yu, J. H.; Shi, Z.; Xu, R. R. *Chemical Communications*. 1431-1432, (2000).
141. Yu, J.; Terasaki, O.; Williams, I. D.; Quiv, S.; Xu, R. *Supramolecular Science*. 5, 297-302, (1998).
142. Williams, I. D.; Gao, Q. M.; Chen, J. S.; Ngai, L. Y.; Lin, Z. Y.; Xu, R. R. *Chemical Communications*. 1781-1782, (1996).
143. Jones, R. H.; Thomas, J. M.; Xu, R. R.; Huo, Q. S.; Xu, Y.; Cheetham, A. K.; Bieber, D. *Journal of the Chemical Society-Chemical Communications*. 1170-1172, (1990).
144. Williams, I. D.; Yu, J. H.; Gao, Q. M.; Chen, J. S.; Xu, R. R. *Chemical Communications*. 1273-1274, (1997).
145. Chippindale, A. M.; Powell, A. V.; Bull, L. M.; Jones, R. H.; Cheetham, A. K.; Thomas, J. M.; Xu, R. R. *Journal of Solid State Chemistry*. 96, 199-210, (1992).
146. Yu, J.; Sugiyama, K.; Zheng, S.; Qiu, S.; Chen, J.; Xu, R.; Sakamoto, Y.; Terasaki, O.; Hiraga, K.; Light, M.; Hursthouse, M. B.; Thomas, J. M. *Chemistry of Materials*. 10, 1208-1211, (1998).
147. Jones, R. H.; Thomas, J. M.; Xu, R. R.; Huo, Q. S.; Cheetham, A. K.; Powell, A. V. *Journal of the Chemical Society-Chemical Communications*. 1266-1268, (1991).
148. Vidal, L.; Gramlich, V.; Patarin, J.; Gabelica, Z. *European Journal of Solid State and Inorganic Chemistry*. 35, 545-563, (1998).
149. Gao, Q. M.; Li, B. Z.; Chen, J. S.; Li, S. G.; Xu, R. R.; Williams, I.; Zheng, J. Q.; Barber, D. *Journal of Solid State Chemistry*. 129, 37-44, (1997).

150. Thomas, J. M.; Jones, R. H.; Xu, R. R.; Chen, J. S.; Chippindale, A. M.; Natarajan, S.; Cheetham, A. K. *Journal of the Chemical Society-Chemical Communications*. 929-931, (1992).
151. Wei, B.; Zhu, G. S.; Yu, J. H.; Qiu, S. L.; Xiao, F. S.; Terasaki, O. *Chemistry of Materials*. 11, 3417-+, (1999).
152. Yu, J.; Sugiyama, K.; Hiraga, K.; Togashi, N.; Terasaki, O.; Tanaka, Y.; Nakata, S.; Qiu, S.; Xu, R. *Chemistry of Materials*. 10, 3636-3642, (1998).
153. Huo, Q. H.; Xu, R. R.; Li, S. G.; Ma, Z. G.; Thomas, J. M.; Jones, R. H.; Chippindale, A. M. *Journal of the Chemical Society-Chemical Communications*. 875-876, (1992).
154. Li, J. Y.; Yu, J. H.; Yan, W. F.; Xu, Y. H.; Xu, W. G.; Qiu, S. L.; Xu, R. R. *Chemistry of Materials*. 11, 2600-2606, (1999).
155. Maple, J. R.; Hwang, M. J.; Stockfisch, T. P.; Dinur, U.; Waldman, M.; Ewig, C. S.; Hagler, A. T. *Journal of Computational Chemistry*. 15, 162-182, (1994).
156. Sun, H. *Macromolecules*. 26, 5924-5936, (1993).
157. Sun, H. *Journal of Computational Chemistry*. 15, 752-768, (1994).
158. Sun, H.; Mumby, S. J.; Maple, J. R.; Hagler, A. T. *Journal of the American Chemical Society*. 116, 2978-2987, (1994).
159. van Beest, B. W. H.; Kramer, G. J.; Vansanten, R. A. *Physical Review Letters*. 64, 1955-1958, (1990).
160. Gale, J. D. *Journal of the Chemical Society-Faraday Transactions*. 93, 629-637, (1997).
161. Wyckoff, R. W. G. *Crystal Structures*; 2nd ed., Vol. 1, 1963.
162. Simmen, A.; McCusker, L. B.; Baerlocher, C.; Meier, W. M. *Zeolites*. 11, 654-661, (1991).
163. Bennett, J. M.; Kirchner, R. M. *Zeolites*. 12, 338-342, (1992).
164. Kirchner, R. M.; Bennett, J. M. *Zeolites*. 14, 523-528, (1994).
165. Yao, Y. W.; Natarajan, S.; Chen, J. S.; Pang, W. Q. *Journal of Solid State Chemistry*. 146, 458-463, (1999).
166. Tuel, A.; Gramlich, V.; Baerlocher, C. *Microporous and Mesoporous Materials*. 56, 119-130, (2002).

167. Yuan, H. M.; Zhu, G. S.; Chen, J. S.; Chen, W.; Yang, G. D.; Xu, R. R. *Journal of Solid State Chemistry*. 151, 145-149, (2000).
168. Vidal, L.; Marichal, C.; Gramlich, V.; Patarin, J.; Gabelica, Z. *Chemistry of Materials*. 11, 2728-2736, (1999).
169. Oliver, S.; Kuperman, A.; Lough, A.; Ozin, G. A. *Inorganic Chemistry*. 35, 6373-6380, (1996).
170. Chippindale, A. M.; Natarajan, S.; Thomas, J. M.; Jones, R. H. *Journal of Solid State Chemistry*. 111, 18-25, (1994).
171. Cygan, R. T.; Liang, J. J.; Kalinichev, A. G. *Journal of Physical Chemistry B*. 108, 1255-1266, (2004).
172. Teppen, B. J.; Rasmussen, K.; Bertsch, P. M.; Miller, D. M.; Schafer, L. *Journal of Physical Chemistry B*. 101, 1579-1587, (1997).
173. de Boer, K.; Jansen, A. P. J.; Vansanten, R. A. *Chemical Physics Letters*. 223, 46-53, (1994).
174. Deman, A. J. M.; Vansanten, R. A.; Vogt, E. T. C. *Journal of Physical Chemistry*. 96, 10460-10466, (1992).
175. Kitao, O.; Demiralp, E.; Cagin, T.; Dasgupta, S.; Mikami, M.; Tanabe, K.; Goddard, W. A. *Computational Materials Science*. 14, 135-137, (1999).
176. Silverstein, R. M.; Webster, F. X.; Kiemle, D. *Spectrometric Identification of Organic Compounds* 72-126. (2005).
177. Heinz, H.; Koerner, H.; Anderson, K. L.; Vaia, R. A.; Farmer, B. L. *Chemistry of Materials*. 17, 5658-5669, (2005).
178. Barrer, R. M. *Transactions of the Faraday Society*. 35, 0644-0655, (1939).
179. Smit, E.; Mulder, M. H. V.; Smolders, C. A.; Karrenbeld, H.; Vaneerden, J.; Feil, D.; Elsevier Science B. p 247-257, (1992).
180. Zhang, R. S.; Mattice, W. L. *Journal of Membrane Science*. 108, 15-23, (1995).
181. Gusev, A. A.; Mullerplathe, F.; Vangunsteren, W. F.; Suter, U. W. *Atomistic Modeling of Physical Properties In Advances in Polymer Science*. Vol. 116, 207-247. (1994).
182. Laguna, M. F.; Guzman, J.; Riande, E.; Saiz, E. *Macromolecules*. 31, 7488-7494, (1998).
183. Beerdsen, E.; Dubbeldam, D.; Smit, B. *Physical Review Letters*. 95, 4, (2005).

184. Tenne, R. *Nature Nanotechnology*. 1, 103-111, (2006).
185. Mukherjee, S.; Kim, K.; Nair, S. *Journal of the American Chemical Society*. In Press, (2007).
186. Farmer, V. C.; Adams, M. J.; Fraser, A. R.; Palmieri, F. *Clay Minerals*. 18, 459-472, (1983).
187. Tamura, K.; Kawamura, K. *Journal of Physical Chemistry B*. 106, 271-278, (2002).
188. Sandomirsky, P. A.; Meshalkin, S. S.; Rozhdestvenskaya, I. V.; Demyanets, L. N.; Uvarova, T. G. *Kristallografiya*. 31, 883-891, (1986).
189. Smith, G. S.; Isaacs, P. B. *Acta Crystallographica*. 17, 842-846, (1964).
190. Berendsen, H. J. C.; Postma, J. P. M.; Vangunsteren, W. F.; Dinola, A.; Haak, J. R. *Journal of Chemical Physics*. 81, 3684-3690, (1984).
191. Bougeard, D.; Smirnov, K. S.; Geidel, E. *Journal of Physical Chemistry B*. 104, 9210-9217, (2000).
192. Deboer, K.; Jansen, A. P. J.; Vansanten, R. A. *Chemical Physics Letters*. 226, 226-226, (1994).
193. Konduri, S.; Mukherjee, S.; Nair, S. *Physical Review B*. 74, art. 033401, (2006).
194. Thorpe, M. F.; Galeener, F. L. *Physical Review B*. 22, 3078-3092, (1980).
195. Galeener, F. L. *Physical Review B*. 19, 4292-4297, (1979).
196. Pauling, L. *Proceedings of the National Academy of Sciences of the United States of America*. 16, 453-459, (1930).
197. Tripathi, A.; Parise, J. B. *Microporous and Mesoporous Materials*. 52, 65-78, (2002).
198. Terrones, H.; Terrones, M. *New Journal of Physics*. 5, 126 (1-37), (2003).
199. Konduri, S.; Tong, H. M.; Chempath, S.; Nair, S. *Journal of Physical Chemistry C*. 112, 15367-15374, (2008).
200. Gupta, A.; Chempath, S.; Sanborn, M. J.; Clark, L. A.; Snurr, R. Q. *Molecular Simulation*. 29, 29-46, (2003).
201. Ramachandran, C. E.; Chempath, S.; Broadbelt, L. J.; Snurr, R. Q. *Microporous and Mesoporous Materials*. 90, 293-298, (2006).

202. Fennell, C. J.; Gezelter, J. D. *Journal of Chemical Physics*. 124, 234104 (1-12), (2006).
203. Skoulidas, A. I.; Sholl, D. S. *Journal of Physical Chemistry B*. 105, 3151-3154, (2001).
204. Mukherjee, S.; Bartlow, V.; Nair, S. *Chemistry of Materials*. 17, 4900-4909, (2006).
205. Gorbach, A.; Stegmaier, M.; Eigenberger, G. *Adsorption-Journal of the International Adsorption Society*. 10, 29-46, (2004).
206. Janchen, J.; Ackermann, D.; Stach, H.; Brosicke, W. *Solar Energy*. 76, 339-344, (2004).
207. Lalik, E.; Mirek, R.; Rakoczy, J.; Groszek, A. *Catalysis Today*. 114, 242-247, (2006).
208. Striolo, A. *Nano Letters*. 6, 633-639, (2006).
209. Arya, G.; Chang, H. C.; Maginn, E. J. *Physical Review Letters*. 91, 026102 (1-4), (2003).
210. Skoulidas, A. I.; Ackerman, D. M.; Johnson, J. K.; Sholl, D. S. *Physical Review Letters*. 89, 185901 (1-4), (2002).
211. Bhatia, S. K.; Nicholson, D. *Journal of Chemical Physics*. 127, 124701 (1-11), (2007).
212. Krishna, R.; Baur, R. *Separation and Purification Technology*. 33, 213-254, (2003).
213. Paoli, H.; Methivier, A.; Jobic, H.; Krause, C.; Pfeifer, H.; Stallmach, F.; Karger, J. *Microporous and Mesoporous Materials*. 55, 147-158, (2002).
214. Malek, K.; Odijk, T.; Coppens, M. O. *Nanotechnology*. 16, S522-S530, (2005).
215. Newsome, D. A.; Sholl, D. S. *Journal of Physical Chemistry B*. 109, 7237-7244, (2005).
216. Newsome, D. A.; Sholl, D. S. *Nano Letters*. 6, 2150-2153, (2006).